DISCOVERY OF ORBITAL SELECTIVE COOPER PAIRING IN FeSe

A Dissertation

Presented to the Faculty of the Graduate School

of Cornell University

in Partial Fulfillment of the Requirements for the Degree of

Doctor of Philosophy

by

Peter Oliver Sprau

August 2017

DISCOVERY OF ORBITAL SELECTIVE COOPER PAIRING IN FeSe

Peter Oliver Sprau, Ph.D.

Cornell University 2017

FeSe is the focus of intense research interest because of its unusual non-magnetic nematic state and because it forms the basis for achieving the highest critical temperatures of any iron-based superconductor. However, its Cooper pairing mechanism has not been determined because an accurate knowledge of the momentum-space structure of superconducting energy gaps $\Delta_i(\vec{k})$ on the different electron-bands $E_i(\vec{k})$ does not exist. Here we use Bogoliubov quasiparticle interference (BQPI) imaging to determine the coherent Fermi surface geometry of the α- and ε-bands surrounding the $\Gamma = (0,0)$ and $X = (\pi/a_{Fe}, 0)$ points of FeSe, and to measure their superconducting energy gaps $\Delta_\alpha(\vec{k})$ and $\Delta_\varepsilon(\vec{k})$. We show directly that both gaps are extremely anisotropic but nodeless, and are aligned along orthogonal crystal axes. Moreover, by implementing a novel technique we demonstrate the sign change between $\Delta_\alpha(\vec{k})$ and $\Delta_\varepsilon(\vec{k})$. This complex configuration of $\Delta_\alpha(\vec{k})$ and $\Delta_\varepsilon(\vec{k})$, which was unanticipated within pairing theories for FeSe, reveals a unique form of superconductivity based on orbital selective Cooper pairing of electrons from the d_{yz} orbitals of iron atoms. This new paradigm of orbital selectivity may be pivotal to understanding the microscopic interplay of quantum paramagnetism, nematicity and high temperature superconductivity.

BIOGRAPHICAL SKETCH

Peter Oliver Sprau was born on June 13th 1986 in the small town of Kirchheimbolanden, Germany, where he completed both his primary and secondary education. Long before he was a physicist, Peter was an active member of the track and field team in his school and a local club, even going on to compete in the dash and relay event on the state and federal youth level. Upon finishing school, he fulfilled his civic duty and carried out his alternative civilian service in the hospital in Kirchheimbolanden.

While Peter's academic interests were diverse, including not just science but also Latin and history, his natural curiosity about the world finally urged him to pursue a higher education in physics. To this end, he left Rhineland-Palatinate and enrolled in the nanotechnology engineering program of the Julius-Maximilians-Universität Würzburg in Bavaria in 2006. Due to outstanding academic achievement, he was among a few in his program selected to participate in an exchange with the University of California Berkeley supported by a fellowship of the DAAD (Deutscher Akademischer Austauschdienst). From August 2009 to May 2010, he worked with Dr. Mary Gilles and Professor Stephen Leone at the Lawrence Berkeley National Laboratory, where he learned how to operate the Scanning Transmission X-ray Microscope at the Advanced Light Source synchrotron.

Undeterred by the long working hours and night shifts involved in synchrotron experiments, he joined Professor Kai Fauth upon his return to Würzburg. He studied the growth and characterization of ultrathin magnetic layers of rare earth silicides using Low Energy Electron Diffraction (LEED) and X-ray Magnetic Circular Dichroism (XMCD) techniques. After successful completion of this one year research project, culminating in the submission of his diploma

thesis, he was awarded his diploma with distinction in the summer of 2012. Wanting to see more of the world as well as continue his studies outside of Germany, Peter applied and was accepted to the physics PhD program at Cornell University beginning in the fall of 2012. At the end of his first year at Cornell, he received an outstanding teaching award as a teaching assistant in Introductory Physics. In early 2013, Peter joined Professor J. C. Séamus Davis to study strongly correlated electron materials with a Spectroscopic Imaging - Scanning Tunneling Microscope (SI-STM). Under Professor Davis' guidance, he completed his Master's degree in physics in May 2015. In recognition of his work, Peter has been invited to present at the Vortex meeting in Madrid in May 2015 and at the Quantum Materials meeting in Vancouver in April 2017.

I dedicate my thesis to my family and friends whose support enabled me to pursue my dreams and ambitions.

ACKNOWLEDGEMENTS

I would like to start my acknowledgements with two quotes that describe the challenges related to the quest that is the pursuit of knowledge in general and a PhD degree in particular. The first one is by Winston Churchill:

"Success consists of going from failure to failure without loss of enthusiasm."

The second one is by author Neil Gaiman:

"I hope that in this year to come, you make mistakes. Because if you are making mistakes, then you are making new things, trying new things, learning, living, pushing yourself, changing yourself, changing your world. You're doing things you've never done before, and more importantly, you're Doing Something.

So that's my wish for you, and all of us, and my wish for myself. Make New Mistakes. Make glorious, amazing mistakes. Make mistakes nobody's ever made before. Don't freeze, don't stop, don't worry that it isn't good enough, or it isn't perfect, whatever it is: art, or love, or work or family or life.

Whatever it is you're scared of doing, Do it. Make your mistakes, next year and forever."

Preventing a loss of enthusiasm and battling frustration was probably the biggest personal challenge throughout my PhD: Experiments break for unexpected and sometimes unknown reasons, results turn out to be inconsequential, or a crucial piece of information remains stubbornly elusive. It was these moments, that the emotional support of my family, my girlfriend Pallavi, and my friends both in Germany and here at Cornell helped me overcome, and ultimately turn my PhD into a success.

On the scientific side, I highly profited and learned a lot from Séamus' out of the box style of thinking, and here is where the Gaiman quote applies: Séamus always encouraged me to tackle the difficult, fundamental, and novel questions,

even if this path is covered with numerous ways to make mistakes. But it is also full of opportunities, and for that I am thankful.

I have to admit that I made mistakes on my path, both while experimenting and when approaching a novel physical problem. Here is where I want to especially thank three people besides Séamus that helped me learn from these mistakes: Freek Massee, Andrey Kostin, and Andreas Kreisel. Freek was the postdoc operating the SI-STM when I joined the Davis group, and he taught me all the intricate details that come with running such a highly complex experiment with admirable patience. Freek inspired me with his rigor towards the science and his commitment; he would never ask me to do anything he would not be ready to do himself. I felt well-prepared when Freek left Ithaca as a friend at the end of 2014.

At this point Andrey joined me in the operation of the SI-STM. I had met Andrey already before I joined the Davis group while teaching 1101 and 1102, and he has become my best friend here at Cornell. Besides his friendship, I also highly appreciated working with him. As with Freek, Andrey is very committed: When we had to stay the night once to complete a cool down of the system, he did not complain, and provided excellent company. He is also very smart, and his sharp mind helped in tackling many of the scientific challenges I encountered throughout my PhD.

The last of the three is Andreas who was a postdoc with Brian Andersen when he visited us last summer. Andreas helped me understand many of the theoretical challenges related to my research, and was and is always available to patiently discuss any question I come up with. Without his help I would not have been able to achieve what I have at this point, and I enjoy our collaboration very much.

There are more I want to thank. I want to thank in no specific order Vikram Gadagkar, Inês Firmo, Ethan Kassner, Mo Hamidian, Stephen Edkins, Chung Koo Kim, Sourin Mukhopadhyay, Rahul Sharma, Anna Eyal, Andrej Mesaros, Inhee Lee, Kazuhiro Fujita, Azar Eyvazov, Ritika Dusad, Ben Pichler, Andrew Parmet, and Yi Xue Chong for making my stay in the Davis group a wonderful experience, and I hope to stay in touch with many of you.

I want to acknowledge my friend Robert who lived with me for the last four years, and always had an open ear when I needed to complain about troubles with my experiment. Nate Ellis, who is a great instructor for the student machine shop course, possibly my favorite course at Cornell due to its project, and offered great advice whenever a part of the STM needed to be fixed by ourselves. Keane Leitch who was extremely helpful in figuring out any safety related issue around the lab, especially after I became safety manager for the group. I want to thank Kacey Acquilano, Debra Hatfield, Douglas Milton, Judy Wilson, and Caroline Brockner. They all made dealing with bureaucratic tasks very easy for me.

I also want to acknowledge in no specific order the following people for useful discussions throughout my PhD: Andrej Mesaros, Anna Bóhmer, Paul Canfield, Brian Andersen, Andreas Rost, Milan Allan, Ulrich Welp, Genda Gu, Cedomir Petrovic, Peter Johnson, Wai-Kwok Kwong, Dirk Morr, Jian-Huang She, Michael Lawler, Eun-Ah Kim, Kyungmin Lee, Daniel Walkup, Paul McEuen, Dung-Hai Lee, Steve Kivelson, Jenny Hoffman, and Peter Hirschfeld. And I want to thank anyone that has supported me throughout my PhD that I have forgotten to mention above.

TABLE OF CONTENTS

LIST OF ABBREVIATIONS

STM := Scanning Tunneling Microscope / Microscopy
SI-STM := Spectroscopic Imaging - Scanning Tunneling Microscope
FT := Fourier Transform
DOS := Density of States
LDOS := Local Density of States
JDOS := Joint Density of States
QPI := Quasiparticle Interference
BQPI := Bogoliubov Quasiparticle Interference
ARPES := Angle-Resolved Photoemission Spectroscopy
INS := Inelastic Neutron Scattering
QO := Quantum Oscillations
CEC := Constant-Energy-Contour
AFM := Antiferromagnet(ic)
BZ := Brillouin Zone
BCS := Bardeen-Cooper-Schrieffer
NMR := Nuclear Magnetic Resonance
MBE := Molecular Beam Epitaxy
FOV := Field of View
LF := Lawler-Fujita

LIST OF FIGURES

CHAPTER 1

INTRODUCTION

The macroscopic quantum mechanical state of superconductivity manages to fascinate even more than 100 years since its initial discovery by H. K. Onnes in mercury [1, 2]. The ability to conduct current without resistance has led to important applications for example in medical technology and fundamental research where very high magnetic fields are required. Currently, the main technological reason that holds back superconductivity are the relatively low critical temperatures of so-called conventional, element and alloy superconductors. The goal remains to find a superconductor which would enable room temperature applications.

The discovery of high-temperature superconductivity in the cuprates in 1986 was thus greeted with much excitement in the scientific community [3]. It also came as a big surprise as the parent state of the cuprates is an antiferromagnet, and magnetism was long thought to be detrimental to superconductivity. Superconductivity in the cuprates is usually referred to as unconventional, and there are other unconventional superconductors: organic salts and heavy-fermion materials [4], but their critical temperatures are very low. Unfortunately, the highest T_C in the cuprates remains at $\sim$ 164 K [4], and there is no consensus among researchers what exactly creates superconductivity in the cuprates.

Interest in unconventional superconductivity got renewed in 2008 when the group of H. Hosono discovered superconductivity in $La[O_{1-x}F_x]FeAs(x = 0.05 - 0.12)$ [5]. This 'iron age' of superconductivity as called by some [6] has brought forth two new families of unconventional superconductors: the pnictides and the chalcogenides. As in the cuprates a transition metal, iron, and parent states

with magnetic order are present. With this in mind the fundamental question emerges if a universal mechanism for unconventional superconductivity exists, and if the iron-based superconductors can help solve the riddle of cuprate superconductivity, and finally create a path to room temperature superconductivity. Incidentally, a record-breaking T_C of 203 K under very high pressure ($\sim$ 90 GPa) in the superconductor H_2S was discovered roughly 2 years ago [7, 8]. Yet, it remains unclear if any real-world applications can materialize out of such extreme conditions.

In the beginning research focused on the pnictides, as T_C was initially higher than in the chalcogenides and high-quality single crystals were easier synthesized in the case of the pnictides. More, recently focus has shifted towards the chalcogenides, and FeSe specifically. This is in part due to the record high T_C achieved for iron-based superconductors by growing a monolayer of FeSe on a $SrTiO_3$ substrate [9–12], but there are additional reasons as we will discuss in more detail later in the introduction.

The introduction is separated into two parts: First we briefly review important general concepts and questions related to iron-based superconductivity. Secondly, we present the most important points about FeSe, and where it differs from other iron-based superconductors.

1.1 Iron-based superconductivity

Iron-based superconductors derive their name from a common motif in their crystal structure similar to the copper oxygen plaquette in cuprate superconductors. This motif is a tetrahedron formed out of iron and chalcogen or pnictogen atoms, see Fig. 1.1. The elements most commonly encountered when

iron-based superconductors are discussed are sulfur, selenium, and tellurium on the chalcogen side, and phosphorus and arsenic for the pnictogens. The two subgroups of iron-based superconductors derive their names accordingly: the pnictides and the chalcogenides.

Research of iron-based superconductivity is a rapidly evolving field due to a great and concerted effort both by theorists and experimentalists over the last ten years. There exist many excellent review articles which address the main questions, theoretical models, and experimental results [6, 12–22]. In the following we provide an overview of the most relevant results for iron-based superconductors, and point the interested reader towards the aforementioned reviews for details.

1.1.1 Crystal and atomic structure

The crystal structure of four common types of iron-based superconductors is presented in Fig. 1.1. Central to the crystal structure is the tetrahedron which consists of a square lattice of Fe-atoms, and a chalcogen / pnictogen atom above or below. The size of the chalcogen / pnictogen atom affects hereby the tetrahedral angle and the distance between Fe-atoms in the square-lattice plane, and has the potential to drastically change the properties as a result [15, 23].

FeSe is the structurally simplest material, as it consists of only the aforementioned trilayers of Fe- and Se-atoms being stacked on top of each other. More complicated families are generated by adding spacer layers between the trilayers. These spacer layers have different levels of complexity as can be seen in Fig. 1.1. There are more families than the ones depicted in Fig. 1.1, but they all have the tetrahedron as elemental building block in common, see for example [15,20].

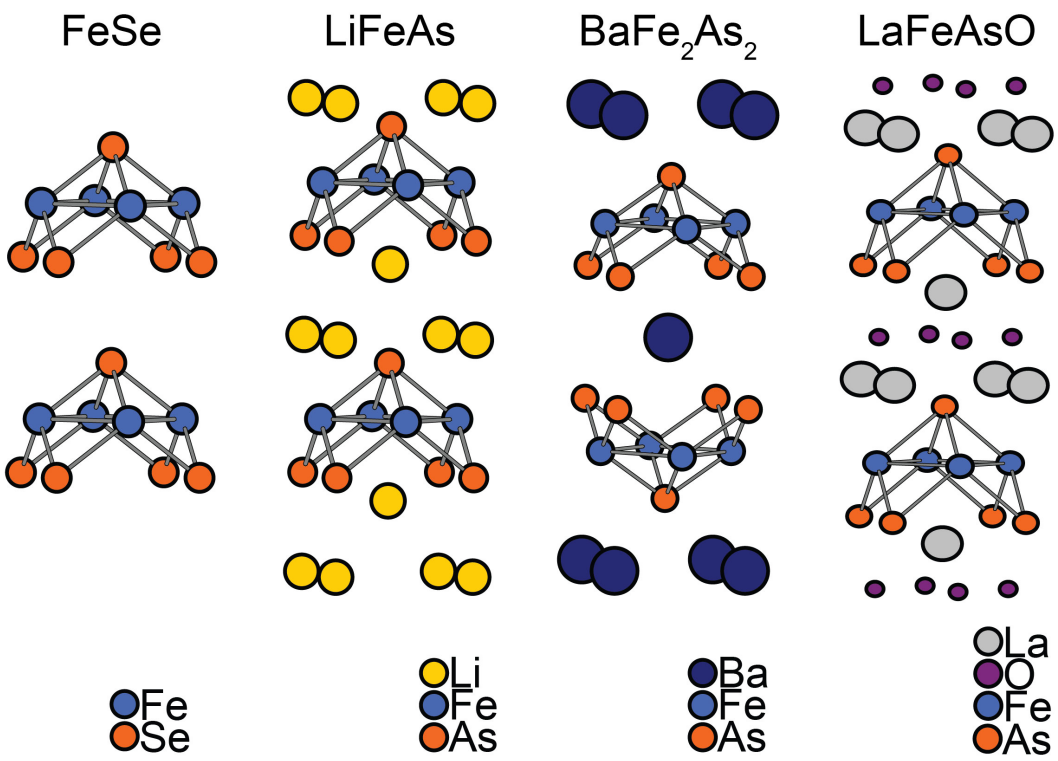

Figure 1.1: Crystal structure of the 11, 111, 122, and 1111 family of iron-based superconductors. The nomenclature 11, 122, etc. is based on the chemical composition of the crystal unit cell; for example 122 corresponds to 1 Ba-atom per 2 Fe- and 2 As-atoms. The common denominator is the tetrahedron formed by iron and chalcogen / pnictogen atoms. In order to emphasize this point the same color has been used for both Se- and As-atoms above. FeSe has the simplest crystal structure of all chalcogenides and pnictides.

On the atomic level the relevant building blocks are the Fe 3d orbitals and the 4p orbitals of the chalcogen / pnictogen atoms. While the overall DOS is dominated by the Fe 3d orbitals, see for example Ref. [26], the chalcogen / pnictogen atoms influence the physics in two important ways. Firstly, the overlap of 4p orbitals and 3d orbitals is important for the hopping of the electrons [14, 26]. Secondly, the chalcogen / pnictogen atom creates a crystal field which leads to a splitting of the energy levels of the individual 3d orbitals.

Figure 1.2 depicts the 3d orbitals. In iron-based superconductors these are the

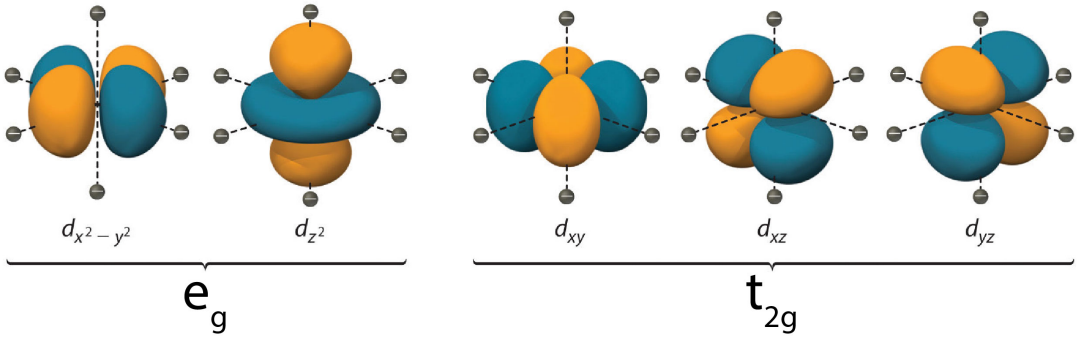

Figure 1.2: 3d orbitals. Shown are the five 3d orbitals. Here negative charges are placed at the corners of an octahedron. Under an octahedral configuration the five 3d orbitals can be divided into two subgroups based on their symmetry: e_g and t_{2g}. The charges create an electrical field which generates different energy splittings for the e_g and t_{2g} orbitals. In a crystal this electrical field is called the crystal field, and an octahedral crystal field exists in the case of the cuprates [24]. For iron-based superconductors the relevant splittings according to the crystal structure are discussed in more detail in Fig. 1.3. Figure reproduced from ref. [25].

3d orbitals of the Fe-atoms, and in the cuprates they belong to the Cu-atoms. In an isolated atom the energy levels of the 3d orbitals are degenerate, but inside a crystal the electrical field generated by the surrounding atoms destroys this degeneracy. In Fig. 1.2 charges are placed at the corners of an octahedron which corresponds to the situation in the cuprates [24]. In iron-based superconductors the alternating placement of chalcogen / pnictogen atoms above and below the Fe-plane creates a crystal field environment that is between a tetragonal and tetrahedral structure [14,22] shown in Fig. 1.3.

Another difference between the cuprates and the iron-based superconductors comes from the different number of electrons in the 3d orbitals. While the Cu-atoms are in a Cu^{2+} state which corresponds to a $3d^9$ configuration the Fe-atoms are in a Fe^{2+} state which results in a $3d^6$ configuration [14,22,24]. In combination with the different crystal structures that results in vastly different distributions of electrons inside the 3d orbitals. Essentially, in the case of iron-based super-

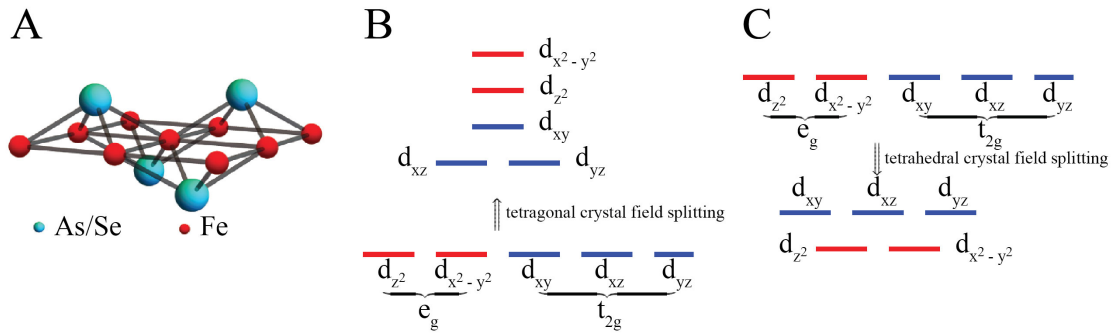

Figure 1.3: Fe 3d orbitals in iron-based superconductors - crystal field splitting. In iron-based superconductors the alternating position of the pnictogen/chalcogen above and below the Fe-lattice (A) creates a situation in between a tetragonal (B) and a tetrahedral (C) crystal field environment. As a consequence all five 3d orbitals need to be considered in models of the electronic structure [14, 22]. Figures reproduced from ref. [22].

conductors in general all five 3d orbitals need to be considered in order to best describe the electronic structure whereas in the case of the cuprates only the $d_{x^2-y^2}$ orbital needs to be taken into consideration.

1.1.2 Electronic structure in $\vec{k}$-space

In general, experiments find highly complex band structures and Fermi surfaces that can be quite different from a detailed point of view for the various families. Nevertheless, there are some common features that we discuss in the following. A generic five orbital / band tight-binding model for the Fe-lattice finds the situation shown in Fig. 1.4A: There are one to three, roughly circular hole-like bands around the Γ-point in the center of the Brillouin zone, and one elliptical, electron-like band around the *X*- and *Y*-point each (here we only show one hole-like band around the Γ-point to simplify the graphic). ARPES measurements show that for some materials only the electron-like pockets exist at the Fermi surface, and one prominent example is the FeSe monolayer grown

on $SrTiO_3$ substrates [12].

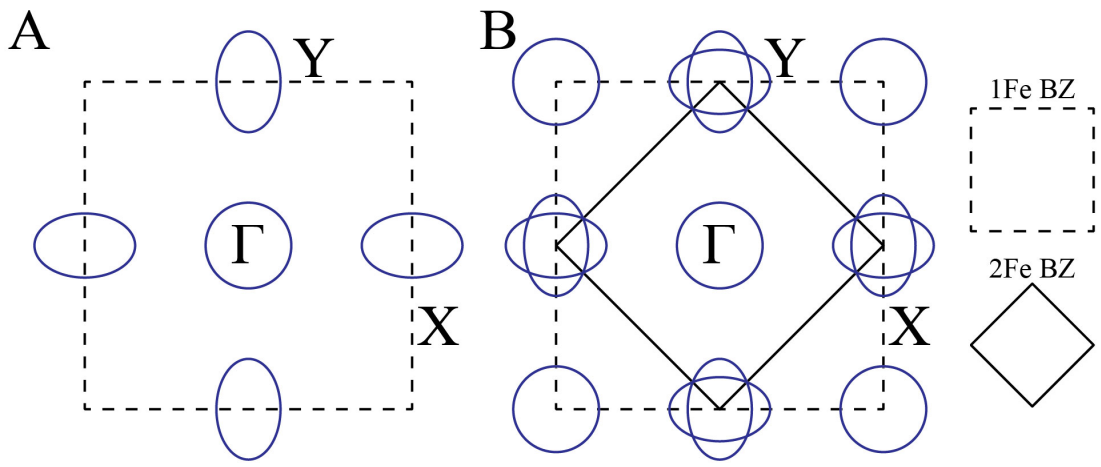

Figure 1.4: 1 Fe unit cell versus 2 Fe unit cell in $\vec{k}$-space. A, Fermi surface for the 1 Fe unit cell. The dashed line marks the 1 Fe unit cell Brillouin zone boundary. **B,** Fermi surface for the 2 Fe unit cell which is created through folding of the 1 Fe unit cell Fermi surface. The solid diamond marks the 2 Fe unit cell Brillouin zone boundary. See for example Fig. 1.6 for depiction of corresponding 1 Fe and 2 Fe unit cell in real space.

So far we have only considered the Fe-square lattice with one Fe-atom per unit cell, but in reality the alternating chalcogen / pnictogen atoms above and below the Fe-atom plane create a bigger unit cell which contains 2 Fe-atoms instead of 1. The two unit cells are called 1 Fe unit cell and 2 Fe unit cell, respectively, and they are shown in Fig. 1.4 in $\vec{k}$-space. A 10-orbital tight-binding model can be created for the 2 Fe unit cell, and a schematic Fermi surface is shown in Fig. 1.4B. Due to symmetry, there is a direct correspondence between the 5 orbital and the 10 orbital model [26, 27].

In band structure sensitive experiments one should observe the picture corresponding to the 2 Fe unit cell as it is the physical unit cell. This is particularly important for the interpretation of quantum oscillation experiments which measure the extremal areas of the Fermi surface, as the two electron pockets at the X- and Y-point can hybridize due to spin-orbit coupling. Such hybridization

can have a sizable effect on the extremal areas.

1.1.3 Phases of matter in pnictides and chalcogenides

Figure 1.5 shows a schematic phase diagram which contains the most important electronic phases observed in pnictides and chalcogenides. Upon cooling the material undergoes a structural transition from tetragonal to orthorhombic symmetry. This structural phase transition is accompanied, or possibly preceded [28], by an enigmatic electronic nematic phase which leads to a huge resistivity anisotropy [29]. Antiferromagnetic order subsequently develops at slightly lower temperatures. At even lower temperatures, superconductivity exists, and becomes most stable where coexisting antiferromagnetic and nematic ordered states are suppressed by doping or pressure [15–18, 22].

As for the cuprate and heavy-fermion compounds superconductivity develops in proximity to a antiferromagnetic phase upon doping with electrons or holes or application of pressure [4], but there are differences between these material systems, as well, and one is the nature of the parent state. The parent state of the cuprates is a Mott insulator, the parent state of the heavy fermions is a heavy fermion metal as the name implies, and the parent state of the iron-based superconductors is a metal. It is necessary to point out that this metallic state is not a simple metal as can be found in for example the alkaline metals. Electronic correlations are of crucial significance in the description of the metallic state found in the iron-based superconductors [13, 20], and we will revisit this question in more detail in the context of FeSe.

The specific phase diagram of FeSe will be presented in part 2 of the introduction, and for the remainder of this subsection we discuss the electronic nematic

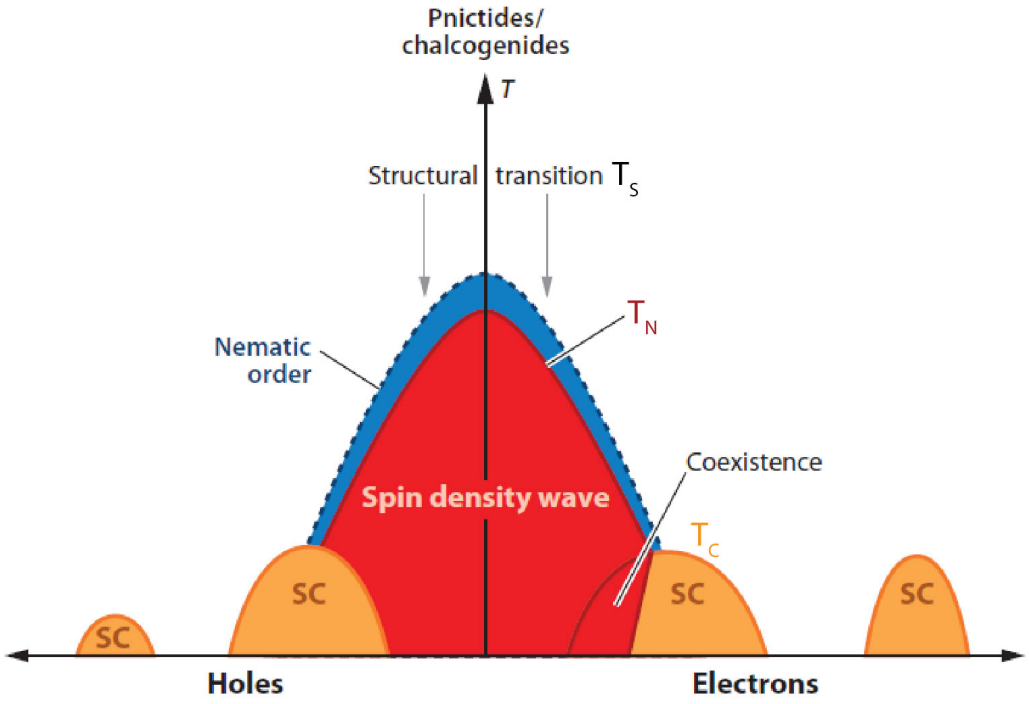

Figure 1.5: Schematic phase diagram for iron-based superconductors. The structural transition T_S from tetragonal to orthorhombic is accompanied by a transition to nematic electronic order, and subsequently followed by antiferromagnetic spin density wave order at T_N. At even lower temperatures T_C, superconducting order develops for a certain amount of electron or hole doping. Note that the antiferromagnetic phase has not been detected for FeSe. Reproduced from reference [18].

phase in some additional detail. The unexpected magnitude of the transport anisotropy in the nematic phase has born the idea that the structural transition is actually driven by electronic degrees of freedom instead of the lattice. Spin-fluctuations have emerged as the most likely candidate for driving the nematic phase [21, 30], but orbital order has been proposed as an alternative [31]. In general, strong coupling between spin, orbital, and lattice degrees of freedom make it hard to readily distinguish the ultimate driving force behind the nematic phase in experiments.

1.1.4 Magnetism

Figure 1.6 shows the most commonly encountered magnetic order in pnictide superconductors, which is called either collinear or stripe order. In the stripe phase the spins order ferromagnetically along the orthorhombic b-axis, and antiferromagnetically along the a-axis. Here, the orthorhombic a-axis is longer than the b-axis. The stripe phase is associated with $(\pi, 0)$ AFM spin-fluctuations which are strongly considered to be the pairing glue for Cooper pairing.

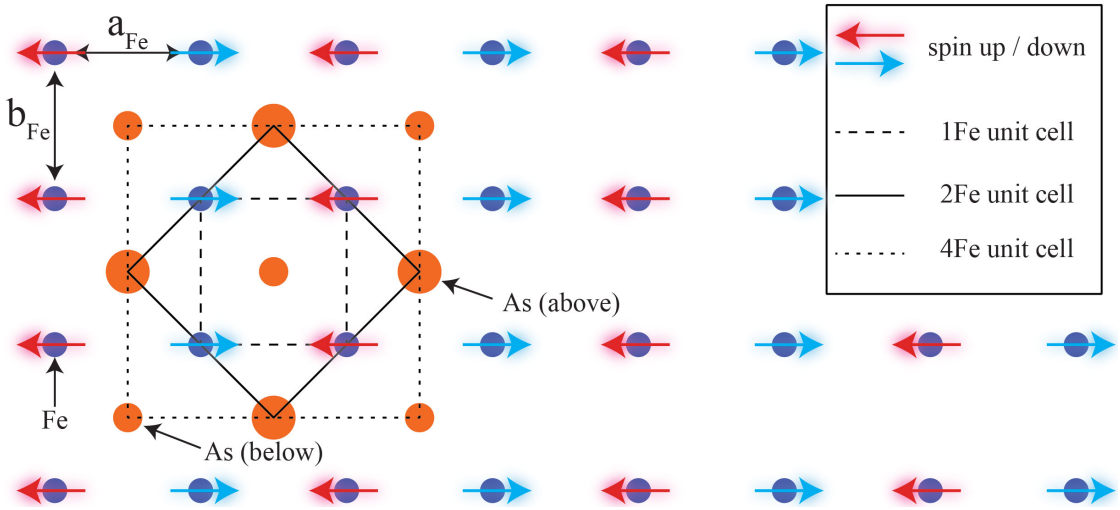

Figure 1.6: Collinear antiferromagnetic order found in pnictide superconductors. Spins couple ferromagnetically along the orthorhombic b-axis and antiferromagnetically along the a-axis. It is often referred to as stripe order and is associated with $(\pi, 0)$ AFM spin-fluctuations.

Figure 1.7 illustrates the Néel type order found in the cuprates. In the Néel phase spins couple antiferromagnetically with all nearest neighbors, and the Néel phase in iron-based superconductors is associated with (π, π) AFM spin-fluctuations. Néel order AFM spin-fluctuations are of importance to the case of FeSe.

Besides the stripe order, other more exotic forms of magnetism exist for example in FeTe and $K_2Fe_4Se_5$ [20,32]. We discuss the bi-collinear or double-stripe order

which is found in FeTe in the context of the FeSe phase diagram in the second part of the introduction.

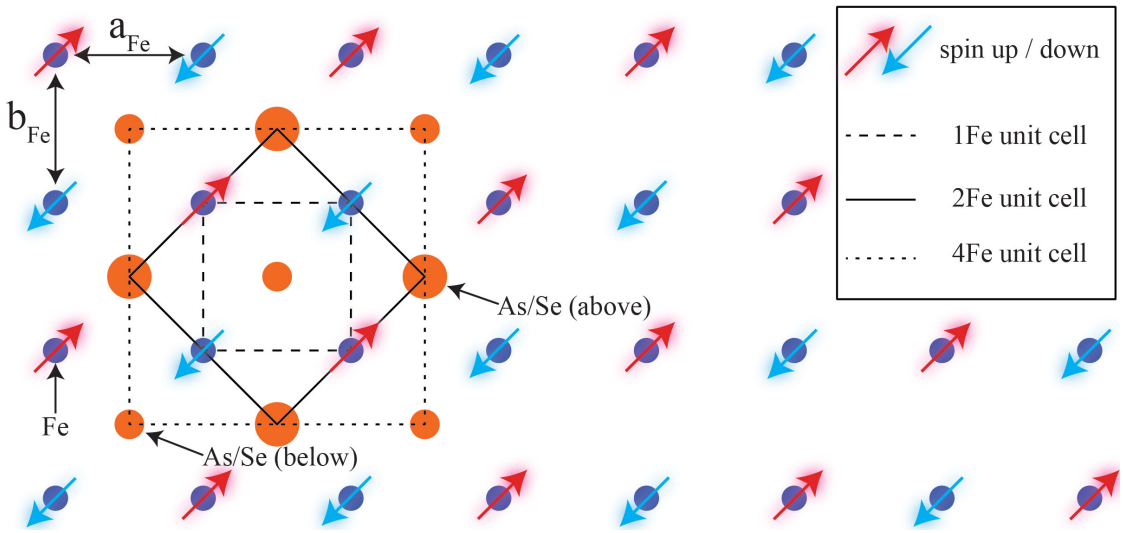

Figure 1.7: Néel antiferromagnetic order. Spins couple antiferromagnetically with all nearest neighbors. This AFM order is found in cuprate superconductors and is associated with (π, π) AFM spin-fluctuations in the case of iron-based superconductors. Competition between $(\pi, 0)$ and (π, π) fluctuations has recently been observed for FeSe by inelastic neutron scattering experiments [33].

The origin of the commensurate magnetic phases observed in various compounds is directly related to the question of metallicity in iron-based superconductors. This is important as it has strong implications for which theoretical framework is appropriate to best describe electrons in iron-based materials. The two diametrically opposite starting points are itinerant electrons and localized electrons. In the itinerant picture the magnetism is due to instabilities towards spin density wave order created by (quasi-)nesting of the Fermi surface [13], as is for example the case in the metal chromium [34]. Correlations only play a minor role in this picture.

The completely localized picture instead describes AFM insulators where magnetism emerges from direct and super exchange, and correlations are extremely important. Transition metal oxides are an example of localized electron physics

[34]. It is important to point out that both models can reproduce some of the major findings of experiments [13]. Thus early on it has been proposed that the truth lies in the middle: Itinerant electrons in combination with important contributions by correlations [13].

1.1.5 Superconductivity

Superconductors are divided into conventional and unconventional superconductors. Conventional means that superconductivity agrees well with the model based on phonon mediated pairing proposed by BCS theory, while for unconventional superconductors the pairing most likely is established by electronic interactions [20]. Every time a new superconductor is discovered one of the first questions is if it is conventional or unconventional? Both in the case of the cuprates and the chalcogenides / pnictides the answer is most certainly unconventional [4].

A telltale sign of unconventional superconductivity are exotic gap structures $\Delta(\vec{k})$ beyond the isotropic gap Δ_0 predicted by BCS theory for phonon mediated pairing, as well as pairing in the triplet instead of the singlet channel of the spin part of the Cooper pair wavefunction. NMR experiments studying the Knight shift in iron-based superconductors have found no sign of triplet Cooper pairing so that the Cooper pairs are thought to be in the spin singlet channel [13].

One hallmark of unconventional superconductivity in the cuprates is the d-wave gap structure with nodal lines along the (π, π) directions of the crystal. This can naturally be explained with the repulsive nature of the pairing interaction caused by AFM spin-fluctuations. Cooper pairing becomes more stable by avoiding the regions of strong Coulomb repulsion [13]. As AFM spin-

fluctuations are expected to be responsible for pairing in the pnictides and chalcogenides, as well, one might ask if similar effects can be seen in iron-based superconductors.

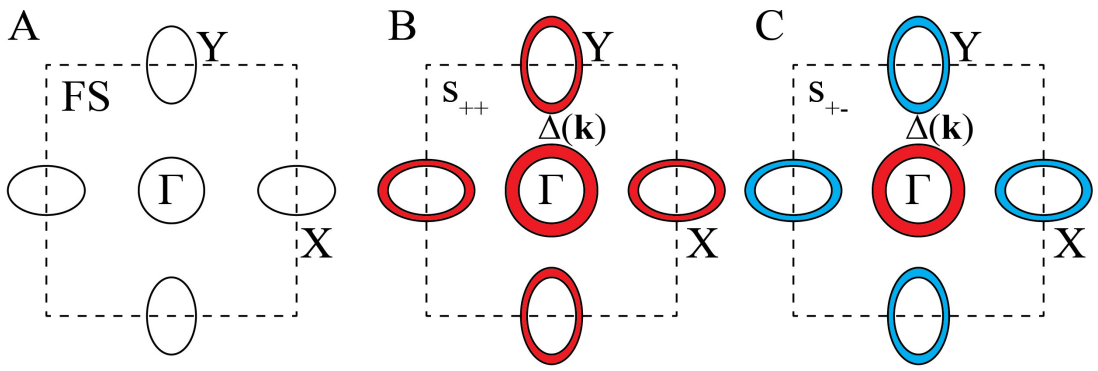

Figure 1.8: Schematic Fermi surface (FS) and gap structure for Fe-based superconductors. A, In a generic three band model the Fermi surface consists of one hole-like pocket in the center of the Brillouin zone and electron-like pockets at the X and Y point, respectively. **B,C,** Superconducting gap structure for the s_{++} (sign-preserving) and s_{+-} (sign-changing) scenario: Red and blue symbolize opposite sign of the gap in the latter case. The dashed lines mark the 1 Fe unit cell Brillouin zone in all three panels.

Figure 1.8 presents the two most widely considered gap structures, s_{++} and s_{+-}, for a schematic Fermi surface. In the case of s_{++} there is no sign change between gaps on the hole-like and electron-like pockets whereas for s_{+-} the gap does change sign. s_{++} is also referred to as (conventional) s-wave, and s_{+-} as extended s-wave. Extended s-wave is found for models using AFM spin-fluctuations for the pairing interaction while conventional s-wave pairing symmetry is caused by phonons or by orbital fluctuations assisted by phonons. d-wave pairing symmetries are found, as well [12, 17]. As there is strong magneto-elastic coupling between the electronic degrees of freedom and the lattice, phonons can modify the gap structure even for the case of AFM spin-fluctuation mediated pairing [13].

On the experimental side, phase-sensitive Josephson junction tunneling ex-

periments played a major role in confirming the d-wave gap structure of the cuprates, but they are less straightforward in distinguishing s-wave from extended s-wave. So far Josephson junction experiments have mostly served to exclude a dominant d-wave pairing in the iron-based superconductors [6, 13]. A second type of experiment sensitive to sign changes of the gap are neutron scattering experiments in the superconducting state. The sensitivity originates from the coherence factor $[1 - \frac{\Delta_{\vec{k}}\Delta_{\vec{k}+\vec{q}}}{E_{\vec{k}}E_{\vec{k}+\vec{q}}}]$ for scattering $\vec{q}$ between the gaps on different pockets. As a consequence a resonance found in the spin-fluctuation spectrum inside the superconducting phase is indicative of an extended s-wave gap, but there are possible alternative explanations for this resonance [6, 12]. New, alternative experiments sensitive to the phase of the superconducting gap are therefore highly searched for in order to confirm the favored extended s-wave gap structure.

1.2 FeSe

We now direct our attention to the peculiar case of FeSe. FeSe appears distinctive compared to other iron-based superconductors for many reasons: (i) FeSe while strongly nematic, does not form an ordered magnetic state and is instead hypothesized to be a quantum paramagnet due to quantum fluctuations of frustrated spin configurations [33, 35, 36]; (ii) strong orbital selectivity [23, 37] of band structure characteristics is reported in FeSe [38–41]; (iii) a monolayer of FeSe grown upon a $SrTiO_3$ substrate produces the highest T_C of all iron-based superconductors [9–12].

1.2.1 Phase diagram of FeSe

Figure 1.9. shows the phase diagram of FeSe both as a function of Te-doping, and as a function of applied pressure. It is believed that pure FeSe only exhibits magnetic order when pressure is applied [42], but there exists the possibility that AFM order develops at extremely low temperatures based on a specific heat experiment published two months ago [43]. In any case, this is very different from pnictide superconductors where the nematic phase and stripe order go hand in hand, and develop at very similar temperatures [20]. This deviation initially cast doubt on the scenario of spin-fluctuation driven nematicity, but recent experiments show that it is still the most likely candidate [44].

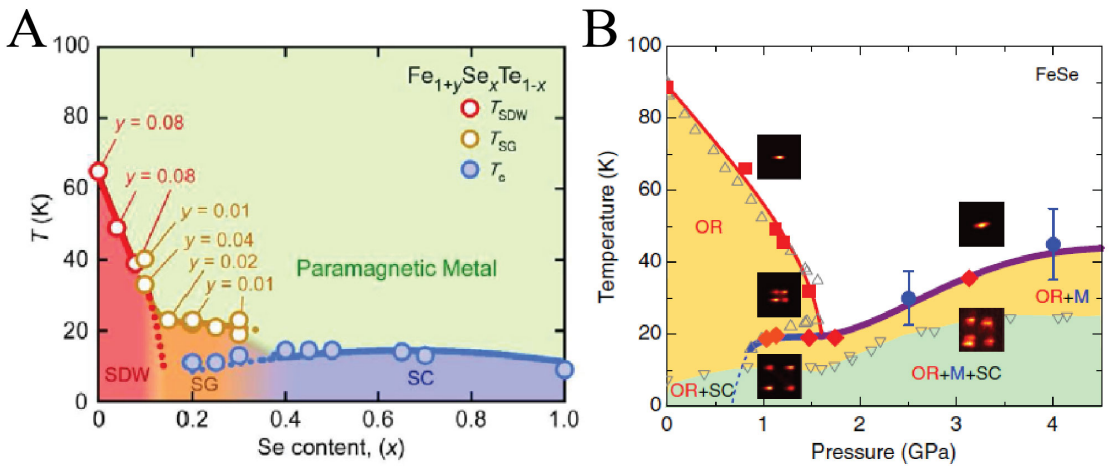

Figure 1.9: Phase diagrams for FeSe. **A,** Phase diagram as a function of tellurium concentration. SG stands for spin glass. The orthorhombic / nematic phase is not shown. Reproduced from reference [45]. **B,** Phase diagram as a function of pressure. OR stands for the orthorhombic phase, and M stands for magnetism. The insets present x-ray diffraction data of the Bragg peak which splits in the orthorhombic phase. Reproduced from reference [42].

Furthermore, inelastic neutron scattering experiments discovered strong competition between stripe and Néel type fluctuations in FeSe [33, 46]. Overall, the unique case that presents itself in FeSe emphasizes the importance of frustration

for the magnetic interactions [33, 35, 36, 47]. Frustrated magnetism potentially plays an important role for the bi-collinear order found in pure FeTe [48], as well. This so-called double stripe order is illustrated in Fig. 1.10.

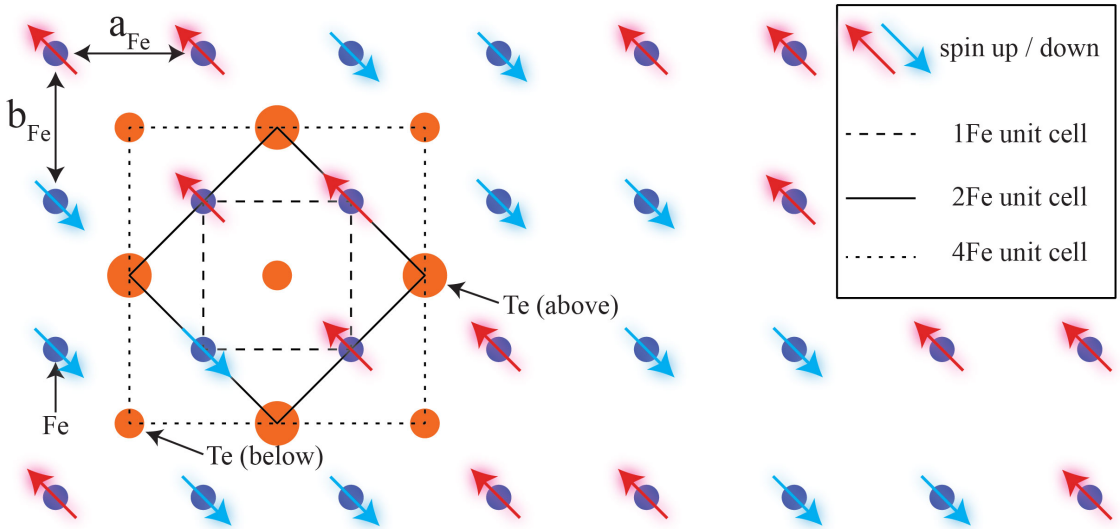

Figure 1.10: Bi-collinear antiferromagnetic order found in FeTe. This unique magnetic order which is associated with $(\pi/2, \pi/2)$ AFM spin-fluctuations has been directly visualized using spin-polarized STM [49].

As FeTe has an overall very similar band structure to the pnictides, and the ordering wavevector for the bicollinear order is $(\pi/2, \pi/2)$ which is unrelated to any possible nesting at the Fermi surface, proponents of the localized electron magnetism see FeTe as proof of the failure of the itinerant magnetism scenario [6, 20].

1.2.2 Crystal structure: Labeling in the orthorhombic phase

As we will make extensive use of the x- and y-axis direction both in real and momentum space we shortly present the labeling notations used in this work inside the orthorhombic phase of FeSe. The high temperature structure of FeSe belongs to the tetragonal $P4/nmm$ space group with the corresponding lattice

parameters $a = 3.77$Å and $c = 5.52$Å [50–52]. Note that here a is the distance between nearest neighbor selenium atoms lying in the same plane. The Fe-Fe nearest neighbor distance is then $a/\sqrt{2}$. On cooling, FeSe undergoes a transition to *Cmma* orthorhombic structure with the lattice parameters $a = 5.31$Å, $b = 5.33$Å and $c = 5.48$Å [50,52]. Here a and b correspond to the two next nearest neighbor distances between selenium atoms lying in the same plane (Fig. 1.11).

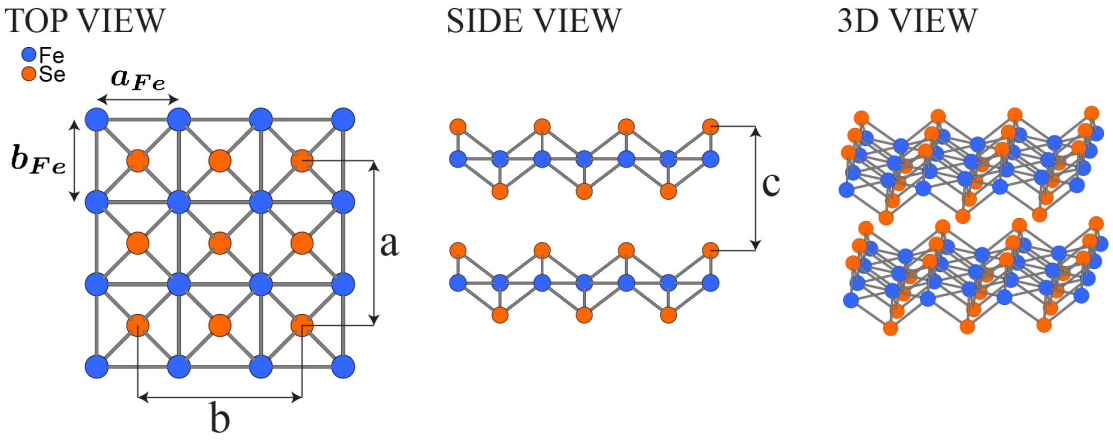

Figure 1.11: FeSe crystal structure in the orthorhombic phase. The lattice parameters $a = 5.31$Å $< b = 5.33$Å $< c = 5.48$Å define the orthorhombic unit cell below the structural transition using conventional labeling. In accordance with earlier work [53, 54] we introduce the non-standard parameters $a_{Fe} > b_{Fe}$ for labeling throughout this thesis: The x-axis, $\vec{k}_x$-axis and $\vec{q}_x$-axis are all parallel to the a_{Fe}-axis, so that labels of orbitals like d_{xy} or d_{yz} or $\vec{k}$-space locations and states, are equally valid in both nematic domains.

In the orthorhombic phase, the two inequivalent Fe-Fe distances are related to the lattice parameters via $a_{Fe} = b/2$ and $b_{Fe} = a/2$. These distances are the most convenient parameters for the discussion of the electronic structure of FeSe, and hence we adopt them throughout this work. We choose $a_{Fe} > b_{Fe}$ to match earlier spectroscopic work [53,54] and for clarity of communication of our key results, even though for the orthorhombic *Cmma* lattice parameters $a < b < c$ are usually enforced by convention [50,52].

1.2.3 Electronic structure of FeSe

The orthorhombic crystal structure of FeSe creates an immediate problem for the study of its electronic structure. Without the application of external strain an orthorhombic crystal will always possess orthorhobic domains of orthogonal orientation. Most bulk probes, as for example neutron scattering or x-ray scattering, or probes that excite a relatively large part of the crystal during measurements, as for example ARPES, average over two orthorhombic domains (Figs. 1.12A, B). The excellent real space resolution of STM provides here a clear advantage.

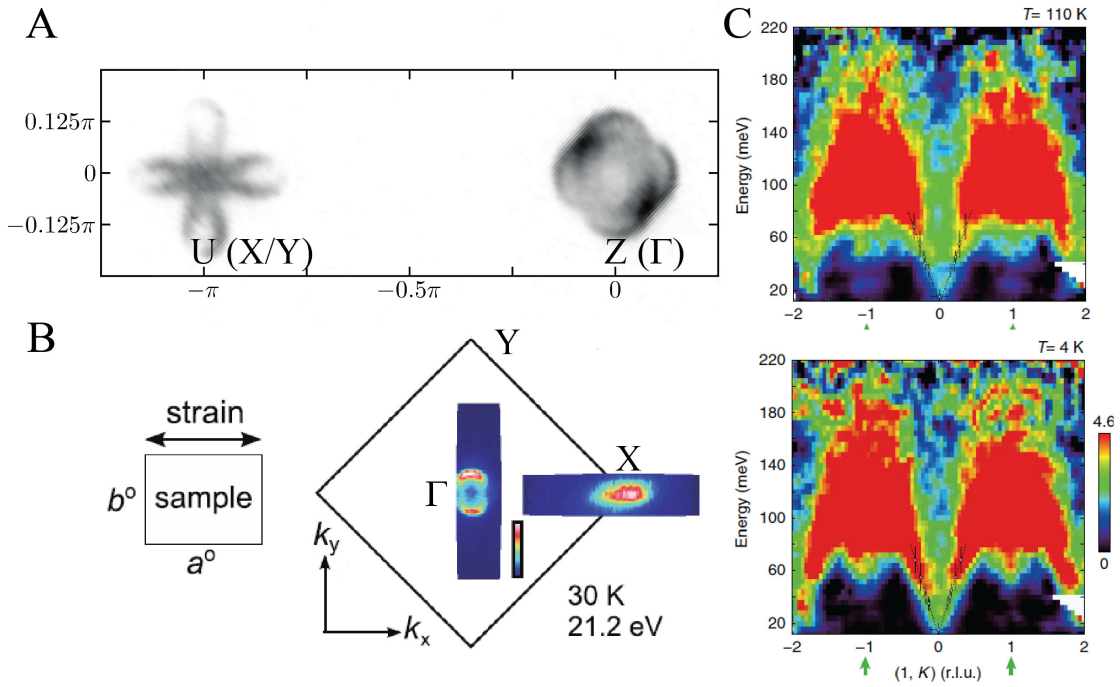

Figure 1.12: ARPES and inelastic neutron scattering on FeSe. **A,** Spectral function at the chemical potential measured on a twinned crystal for $k_z = \pi$. Reproduced from reference [55]. **B,** Spectral function at the chemical potential measured on a detwinned crystal through application of strain for $k_z = 0$. Reproduced from reference [54]. **C,** Dispersion of spin-fluctuations measured for twinned FeSe crystals using INS shows the transfer of spectral weight from (π, π), marked by green arrows, to $(\pi, 0)$ fluctuations below the orthorhombic transition. Reproduced from reference [33].

Multiple ARPES, quantum oscillations, and neutron scattering measurements have been executed over the last several years. Here we shortly summarize the most important findings. In the orthorhombic phase, an ellipsoidal hole-like band exists at the center of the Brillouin zone that shows a clear k_z-dependence in ARPES experiments [55, 56]. At the X-point of the 1 Fe unit cell ARPES experiments find a 'bow tie' shaped, highly elongated electron-like pocket. Based on quantum oscillations measurements another electron-like pocket should exist at the Y-point, but its exact shape remains uncertain as spectroscopic probes struggle to detect it without ambiguity. The relevant 3d orbitals are d_{xz}, d_{yz}, and d_{xy} in the vicinity of the Fermi surface. We discuss the electronic structure in additional detail when we introduce our tight-binding model for FeSe.
As mentioned above, inelastic neutron scattering (INS) experiments detect competition of stripe and Néel type spin-fluctuations in FeSe (Fig. 1.12C) [33,46]. In the context of a possible frustrated quantumparamagnetic ground state in FeSe, detwinned INS experiments would be of particular interest as for example recently pointed out by She et al. [57].

1.2.4 Strong orbital selective correlations in chalcogenides

The topology of the electronic structure in $\vec{k}$-space, while key to understanding the coherent quasiparticle states, deemphasizes correlations. However, as we pointed out in part one of the introduction a fundamental issue in iron-based superconductors is whether conduction electrons are weakly or strongly correlated, and the consequences thereof for enhancing magnetism and or superconductivity. The situation is complex because multiple Fe orbitals (e.g. d_{xz}, d_{yz}, d_{xy}) are involved.

Most germane to FeSe and the other chalcogenides is the Hunds metal viewpoint [23] where strong Hunds coupling within a metallic state, while aligning the Fe spins, also enhances inter-atomic Coulomb repulsion and thus correlation strength. One fascinating possibility is then that orbital selectivity may occur in the effects of the correlations [23,37], so that $\vec{k}$-space states corresponding to specific d-orbitals could become distinct in terms of quasiparticle spectral weight, interactions and ordering. In the most extreme case, an orbital selective Mott phase could develop where electrons in one 3d orbital effectively enter an insulating phase [37,58,59].

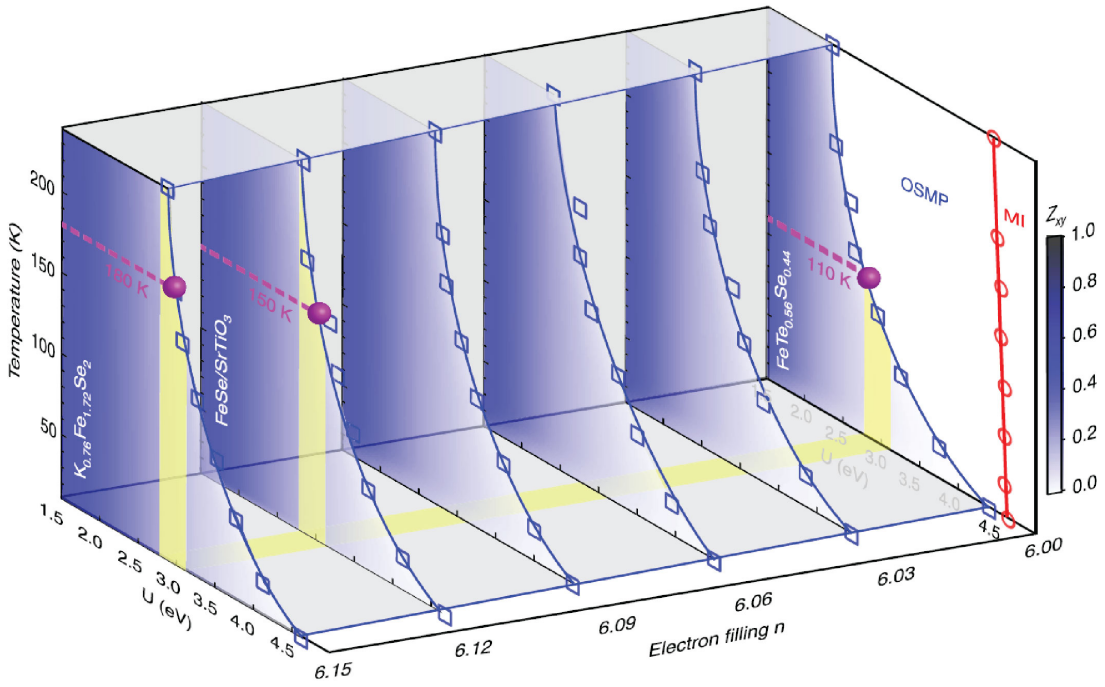

Figure 1.13: Orbital selective correlations in chalcogenides. Slave-spin mean-field phase diagram calculated for the five-orbital Hubbard model. Z_{xy} is the quasiparticle weight of the d_{xy} electrons. OSMP stands for orbital selective Mott phase and MI is the Mott insulating phase. The purple dashed line and purple point has been extracted from experiment for various chalcogenide compounds. It marks the temperature at which the spectral weight of the d_{xy} electrons vanishes. Figure reproduced from reference [40].

A combined ARPES and theory study indeed found evidence for strong orbital

selective correlations across several chalcogenides [40], see Fig. 1.13. The significance of correlations is not restricted to the chalcogenides per se, and theoretical studies predict similar effects for the pnictides, as well [23]. However, the strength of correlations is not the same, and it has been found that the chalcogenides are more strongly correlated than the pnictides [23, 58]. This puts the chalcogenides in the interesting region between the more itinerant pnictides with the weakest correlations, and the even stronger correlated cuprates. Study of chalcogenide superconductors like FeSe is thus highly promising as it could shed light on the importance of correlations for unconventional superconductivity from a different angle.

1.2.5 Prediction of orbital selective superconductivity

In the context of superconductivity, orbital selective correlations pave the way for an even more intriguing possibility: that the pairing itself might become orbital selective [60, 61] so that the electrons of a specific orbital character bind to form the Cooper pairs of the superconductor. If this occurs, the superconducting energy gaps should become highly anisotropic [60, 61], being large only for those FS regions where a specific orbital character dominates. In Fig. 1.14 this situation is shown for a strong coupling $t - J_1 - J_2$-model introduced by Yu et al. [61].

The orbitally resolved Fermi surface for their five orbital tight-binding model is depicted in Fig. 1.14A using the 1Fe unit cell. Here the three hole-like pockets at $(0, 0)$ and $(\pm 1, \pm 1)$ are of pure d_{xz}, d_{yz}, and d_{xy} content while the electron-like pockets at $(\pm 1, 0)$ [and $(0, \pm 1)$] modulate between d_{xz} [d_{yz}] and d_{xy}. The orbital content of the Fermi surface becomes significant when the orbitally resolved

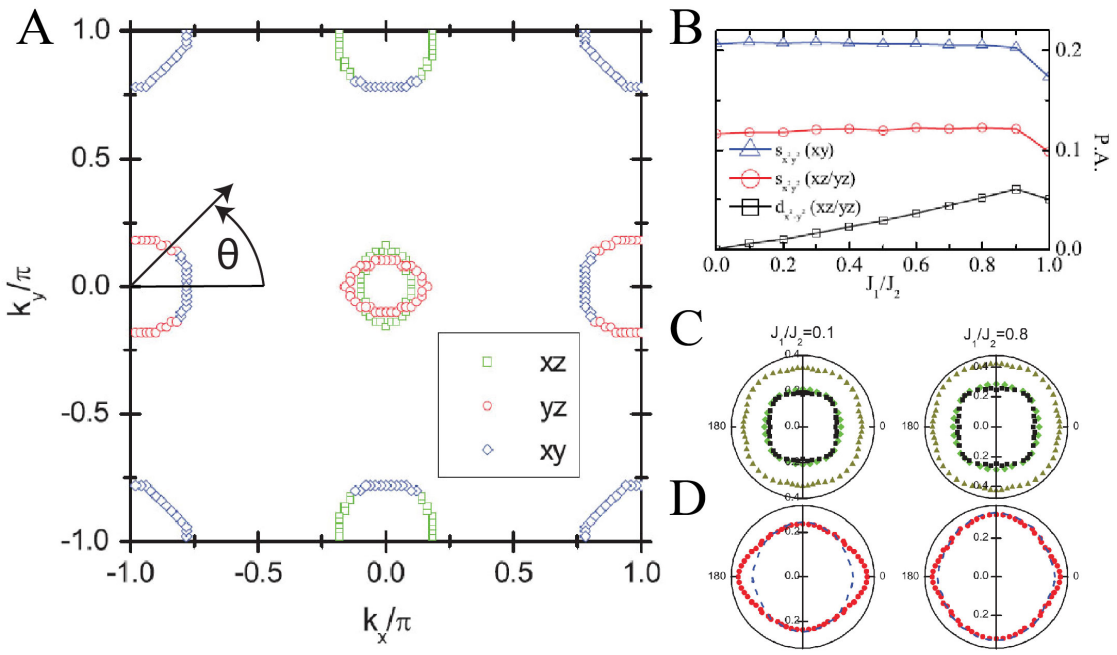

Figure 1.14: Orbital selective superconductivity in strong coupling $t - J_1 - J_2$-model. **A,** Orbitally resolved Fermi surface for the five orbital tight-binding model used in calculations. Note the modulation of orbital content for the electron like pockets at (1,0) and (0,1). **B,** Orbitally resolved pairing amplitudes as function of J_1/J_2. **C,** Excitation gap in $\vec{k}$-space for the hole pockets for two different values of J_1/J_2. **D,** Excitation gap in $\vec{k}$-space for the electron pockets for two different values of J_1/J_2. Anisotropy of the gap is reduced for higher J_1/J_2-values. Figures reproduced from reference [61].

pairing amplitudes are considered which are shown in Fig. 1.14B. For a big anisotropy between J_1 and J_2, pairing in the d_{xy}-orbital is far bigger than pairing in the d_{xz}/d_{yz}-orbitals. This changes when the anisotropy between J_1 and J_2 is reduced. Now pairing in a d-symmetry channel additionally becomes sizable for the d_{xz}/d_{yz}-orbitals, and the sum of s- and d-symmetry becomes comparable to the s-symmetry pairing of the d_{xy}-orbital.

The resulting theoretical superconducting excitation gaps in momentum space are shown in Figs. 1.14C, D for the hole-like and electron-like pockets, respectively. As the hole-like pockets lack any form of orbital content variation, the gaps are quite isotropic. The gap of the electron-like pocket instead is very

anisotropic for a big J_1/J_2 anisotropy, being large where the orbital content belongs to the d_{xy}-orbital. The expected reduction of this anisotropy based on the J_1/J_2-dependence in Fig. 1.14B is observed for $J_1/J_2 = 0.8$.

1.2.6 C_2-symmetric superconductivity

Keeping the discussion of orbital selective correlations and superconductivity in mind we next review experimental findings of superconductivity in FeSe. As the first generation of single crystals struggled with pollution by iron impurities, some of the first studies of the superconducting state in FeSe were executed using high-quality MBE grown thin films [53]. Thin films are hereby not to be confused with the monolayer FeSe. Figure 1.15 presents a STM study of thin films that found extremely elongated, C_2-symmetric vortex cores. The long axis of the vortex core aligns with the long axis ($x \Leftrightarrow a_{Fe}$ in our notation) of the orthorhombic lattice.

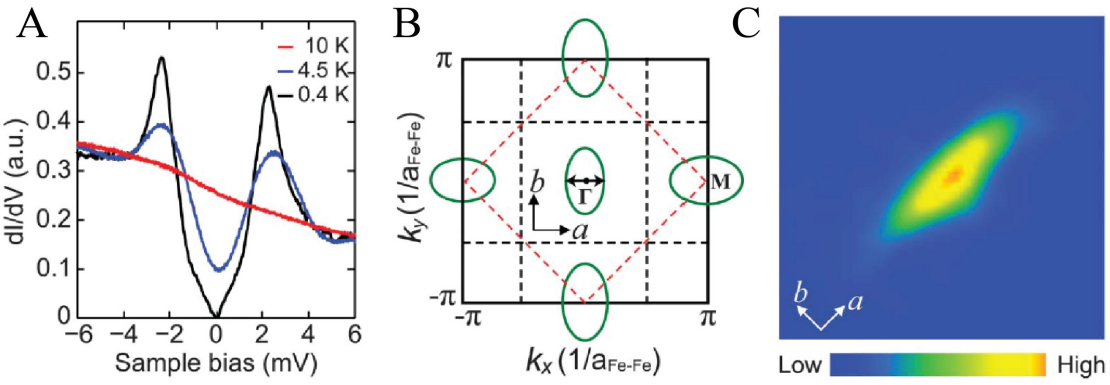

Figure 1.15: Anisotropic vortex core in FeSe. **A,** Temperature evolution of differential tunneling conductance as measured on MBE-grown thin films. **B,** Schematic FS defining the two inequivalent Fe-Fe-directions a and b used in C. **C,** Elongated vortex core visualized by STM on MBE-grown thin films. A-C reproduced from reference [53].

The seemingly V-shaped gap discovered by tunneling spectroscopy (Fig. 1.15A) was interpreted as indicative of a nodal gap structure [53]. The existence of nodes in the gap structure of FeSe has since then come under scrutiny, and contradictory studies for [62, 63] and against nodes [64–68] have since then be published. Figure 1.16 presents microwave and thermal conductivity measurements that both find results consistent with nodeless superconductivity [65, 66].

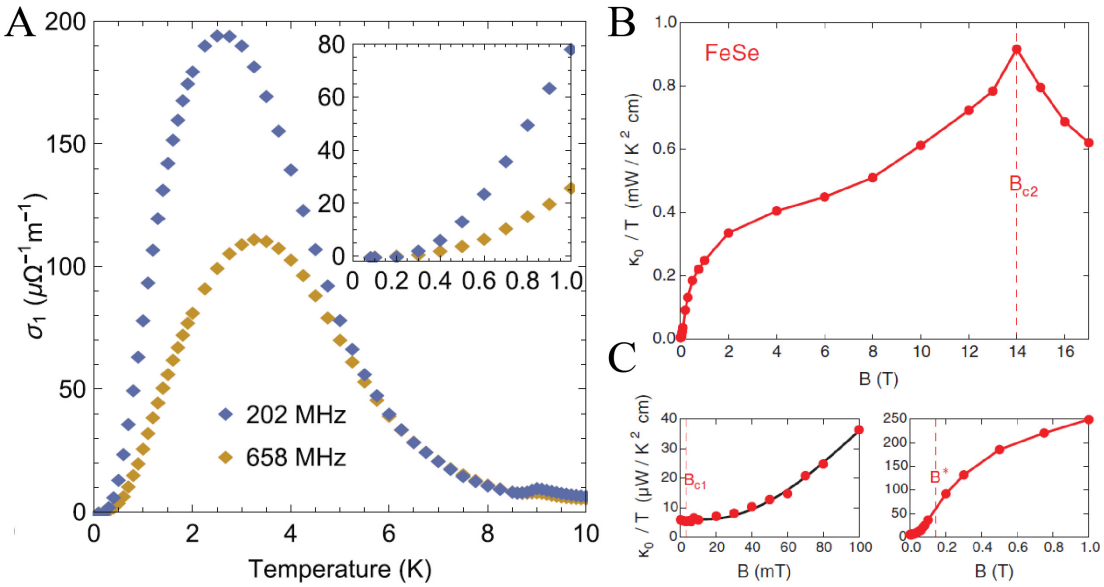

Figure 1.16: Nodeless superconductivity in FeSe deduced from microwave conductivity and thermal conductivity measurements. A, Real part of the microwave conductivity measured between 0.1 and 10 K. Note the region of zero conductivity between roughly 0.1 and 0.3 K in the inset. Reproduced from reference [65]. **B,C,** Magnetic field dependence of the residual linear term of the thermal conductivity is conistent with no nodes in the superconducting gap. B_{c2} is the upper critical field, and B_{c1} is the lower critical field. B^* marks an inflection point in the curvature. G and H reproduced from reference [66].

Based on the microwave conductivity measurements, the quasiparticles in FeSe are extremely long-lived which makes it unlikely that different amount of point defect impurities could alter the superconductivity correspondingly. A possible explanation for the discrepancies between the various studies could be the ex-

istence of different amounts of twin boundaries [63, 65], and measurements of detwinned samples could shed further light on the existence of nodes in the gap structure of FeSe in the absence of orthorhombic domains [65].

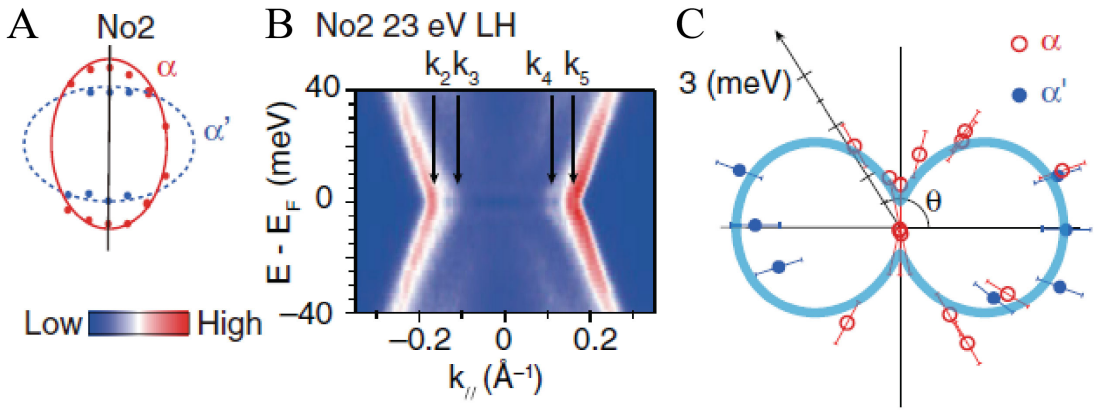

Figure 1.17: Highly anisotropic energy gap on hole-like pocket in S-doped FeSe. A-C, ARPES on twinned $Fe(Se_{1-x}, S_x)$, $x = 0.07$, crystals reveals a highly anisotropic superconducting gap [polar plot in panel C] for the hole-like α-pocket at Γ. A-C reproduced from reference [69].

The issue of nodes aside, all studies agree that their findings imply a very anisotropic gap structure for FeSe [63,65,66]. The first direct evidence of such an anisotropic gap was found in an ARPES experiment on S-doped FeSe [69]. The ARPES study used twinned crystals as can be seen in Fig. 1.17, and revealed a nodeless gap on the hole-like pocket at the Γ-point that has its maximum gap along k_x, and its minimum gap along k_y. No gap was detected for the electron-like pockets, and the authors concluded that no current pairing theory can account for such a highly anisotropic, C_2-symmetric gap structure [69].

The existence of strong orbital selective correlations [39–41] and the detection of such a highly anisotropic gap [69] engineers a unique opportunity to explore the influence of orbital selective correlations on superconductivity and possibly orbital selective superconductivity itself. Such phenomena, although important to understanding and achieving higher temperature superconductivity in cor-

related multi-orbital superconductors [23, 37–41], have remained largely unexplored because orbital selective Cooper pairing has never been detected in any material. For these reasons, it is essential to understand the electronic structure and superconductivity of FeSe at a microscopic level.

CHAPTER 2

FOURIER TRANSFORM SCANNING TUNNELING MICROSCOPY

The invention of the Scanning Tunneling Microscope (STM) by Binnig and Rohrer revolutionized the study of surfaces as it allowed to characterize surfaces with unprecedented precision in real space [70, 71]. One example is the direct imaging of the 7x7 surface reconstruction of the Si(111) surface shortly after [72]. Since then it has become clear that STM can be used for more than simple surface characterization, and Scanning Tunneling Spectroscopy (STS) has been used to probe the electronic structure of many diverse exotic phases such as unconventional superconductors, charge and spin density wave systems, and topological insulators [73–76].

Here, we will focus on the study of superconductivity via STM and STS. Historically, tunneling spectroscopy utilizing planar tunnel junctions played a key role in the successful verification of BCS theory in conventional phonon-driven superconductivity [77–79]. It is thus not surprising that next-generation tunneling spectroscopy experiments are being used extensively in the study of unconventional superconductors as the cuprates, heavy fermions, and iron-based superconductors [80–82]. In the following, we shortly review the basic principles of STM and STS, and after that show how Fourier transform techniques can be used to study the electronic structure of superconductors in quite unexpected ways for an inherently real space probe.

2.1 Spectroscopic Imaging - Scanning Tunneling Microscopy

Spectroscopic Imaging - Scanning Tunneling Microscopy (SI-STM) refers to a class of STM which is optimized for taking spectroscopic maps on a two-dimensional grid in real space that is registered to the crystal lattice. This is a very powerful technique to visualize variations in the electronic structure down to the atomic scale. Additionally, Fourier transforms of such maps contain important information about the electronic structure in momentum space [80–83].

2.1.1 Operation principles of Scanning Tunneling Microscopy

The STM operates based on the quantum mechanical tunneling effect between a sharp metallic tip and a conducting surface (Figs. 2.1A, B). If the tip gets close enough to the surface a measurable tunneling current will exist when the wave-functions of the electrons in the tip and the sample develop a sizable overlap. This tunneling current is exponentially dependent on the distance d between the tip and sample so that the control of d becomes critical for the operation of a STM [73]. Using piezo electronics both d and x- and y-position of the tip can be adjusted with pm precision, and there exist several different designs how to implement piezo electronics to control the tip in a STM, see Ref. [73] (and references therein). Figure 2.1C shows a photograph of the homebuilt STM [84] used for the work within this thesis. Here the tip is facing up, and the fine x, y, and z motion is controlled via a piezo scanning tube that holds the tip. The coarse z motion which is used for the initial approach towards the down-facing sample is based on a 'friction motor' design [84]. A ^3He-refrigerator [84] enables measurements below 300 mK, and a magnetic field of up to 9 T can be applied

perpendicular to the sample surface.

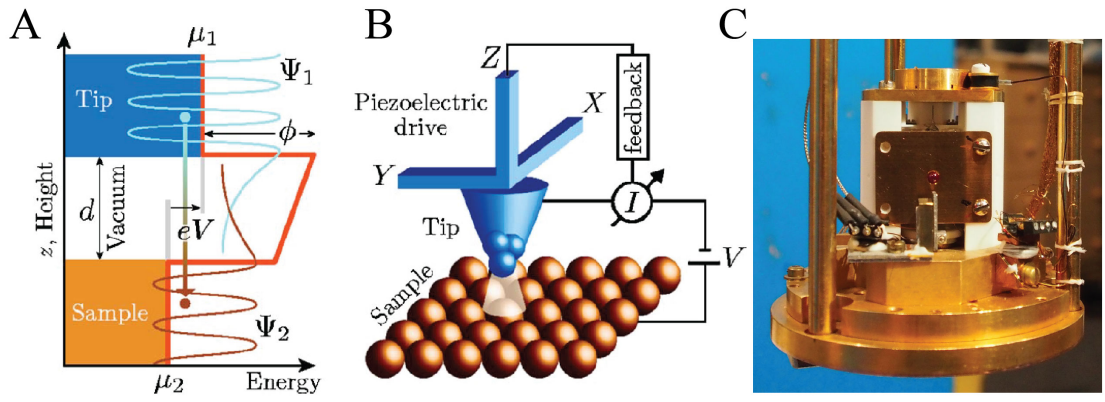

Figure 2.1: Scanning Tunneling Microscopy. **A,** Sketch of the quantum mechanical tunneling process between tip and sample utilized in STM. **B,** Schematic picture of the STM scanning an atomic surface. A, B reproduced from reference [73]. **C,** Photograph of the homebuilt STM [84] used for the work presented in this thesis.

The tunneling current between tip and sample is calculated after Tersoff and Hamann according to [85]:

$$I = \frac{2\pi e}{\hbar} \sum_{\mu,\nu} f(E_\mu)[1 - f(E_\nu + eV)]|M_{\mu\nu}|^2 \delta(E_\mu - E_\nu), \tag{2.1}$$

where f is the Fermi-Dirac distribution function, and μ and ν denote tip and sample, respectively. V is the applied bias between sample and tip, and $M_{\mu\nu}$ the tunneling matrix element which is calculated as follows:

$$M_{\mu\nu} = \frac{\hbar^2}{2m} \int d\vec{S}(\Psi_\mu^* \nabla \Psi_\nu - \Psi_\nu \nabla \Psi_\mu^*). \tag{2.2}$$

Here S is any surface between the sample and tip, and Ψ is the electron wave-function of the sample and tip, respectively (Fig. 2.1A). In general, it is a good approximation that the matrix element is a constant, but that does not have to be the case [73].

In order to characterize the profile of a surface two scan modes exist (Fig. 2.2).

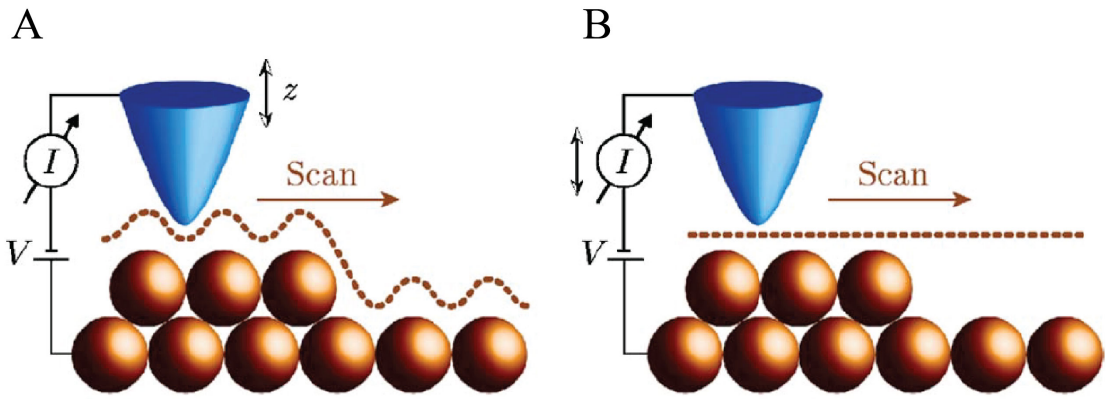

Figure 2.2: STM scan modes for surface characterization. A, In the constant current mode the surface profile is generated through the variation of the height z of the tunneling tip. **B,** In the constant height mode the surface profile is generated through the variation of the tunneling current as a function of position. A, B reproduced from reference [73].

The first is the constant current mode where a feedback loop maintains a constant current while the tip scans across the surface continuously adjusting the tip sample separation. The second is the constant height mode. Here the tip is held at a constant height and the tunneling current varies with changes in the tip sample distance. The preferred mode of operation is constant current mode in most scenarios, as constant height mode carries greater risk of collisions between the tip and sample [73]. In both cases, if the sample is completely homogeneous the variation in the current will be due to the differences in the tip sample separation as a function of position. Thus, these modes of operation are often referred to as topography.

Besides topography, Scanning Tunneling Spectroscopy (STS) is a commonly used mode of operation of the STM. One can show that the tunneling conductance $g(V) \equiv dI/dV(V)$ is to a good approximation proportional to the local density of states (LDOS) under a certain set of conditions [73]:

$$g(V) \equiv dI/dV(V) \propto LDOS\,(V) \tag{2.3}$$

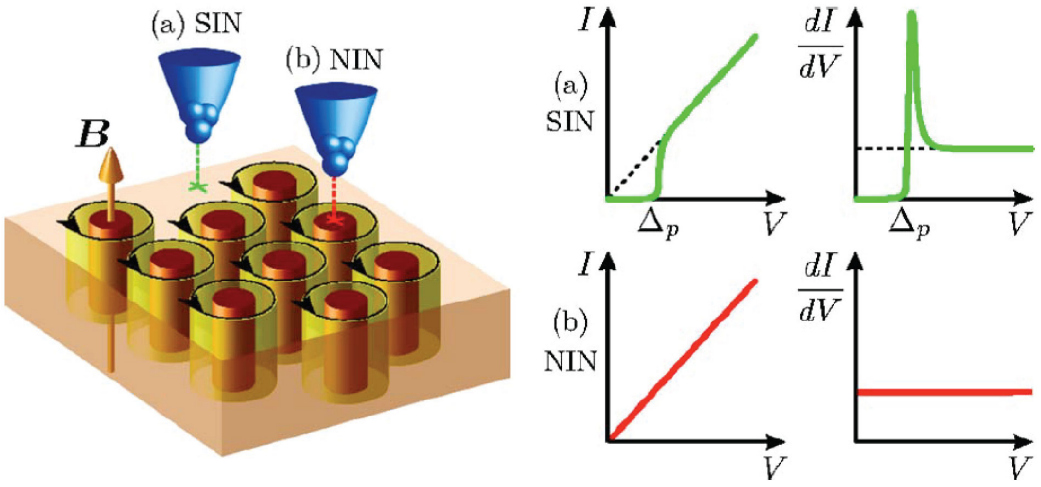

Figure 2.3: Scanning Tunneling Spectroscopy. Differential tunneling conductance is measured via a lock-in amplifier technique. Tunneling spectroscopy is a powerful tool as the conductance is proportional to the local density of states. In the example above superconducting vortices are visualized by taking advantage of the fact that superconductivity is suppressed inside the core of a vortex. Here SIN stands for a Superconductor Insulator (vacuum) Normal (metal) tunneling junction, and NIN for Normal Insulator Normal, accordingly. Reproduced from reference [73].

In order to acquire the differential tunneling conductance one can either numerically differentiate the tunneling current $I(V)$ or preferably use a lock-in technique [73]. Figure 2.3 shows an example of how STS and SI-STM can be used to visualize vortices in a superconductor.

2.1.2 Quasiparticle interference

It is a well-known fact of condensed matter physics that a defect placed inside a conductor causes oscillations of the charge around the defect. These oscillations are called Friedel oscillations. STM allows us to directly visualize Friedel oscillations in real space, see Figs. 2.4A, D, E.

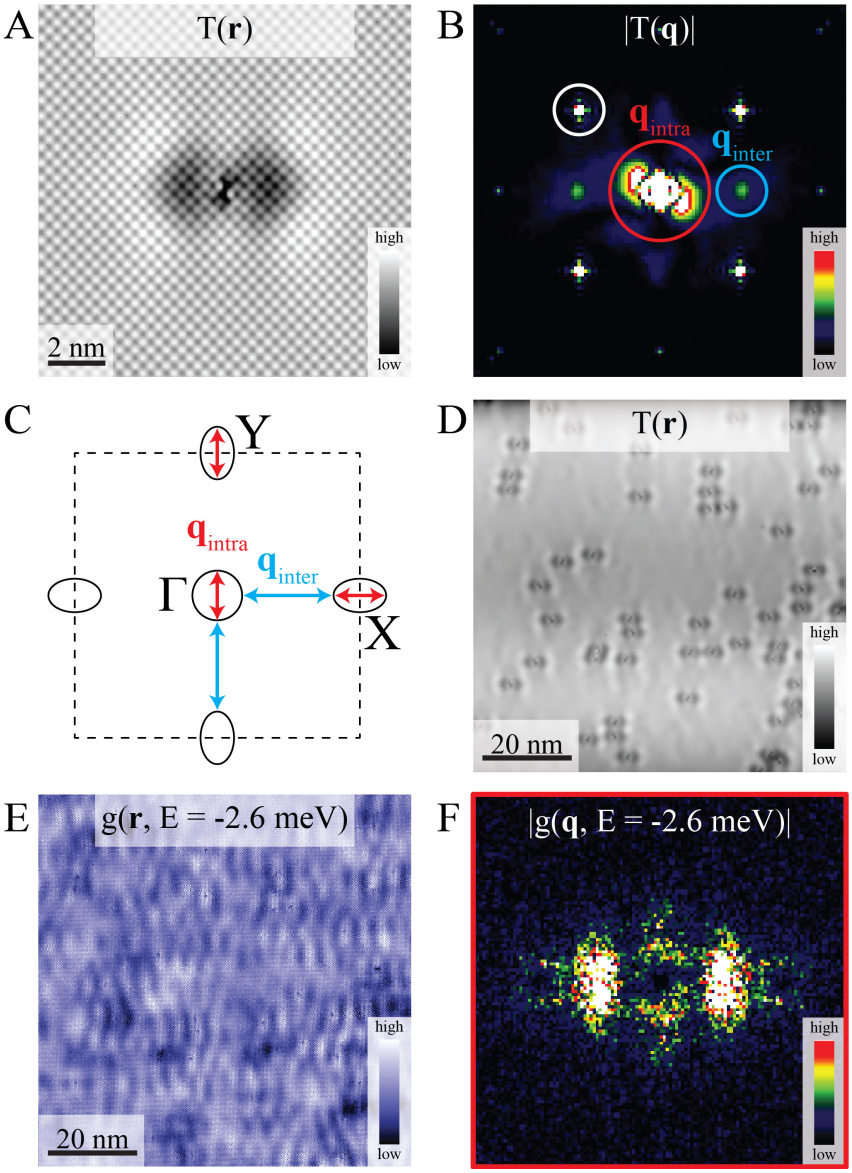

Figure 2.4: Spectroscopic Imaging - Scanning Tunneling Microscopy. **A,** Topography of a single defect in FeSe. Note the strong Friedel oscillations. **B,** Amplitude of the FT of topography shown in A. Red circle marks regions in **q**-space corresponding to scattering within hole-like and electron-like pockets. The blue circle shows a region in **q**-space that is connected via scattering between pockets, see also C. The white circle marks one of the Se-Bragg peaks whose **q**-vector is determined by the atomic corrugation visible in A. **C,** Schematic constant-energy-contour in $\vec{k}$-space presenting possible intra- and inter-pocket scattering vectors. **D,** Topography of many defects in FeSe. A 3-by-3 pixel averaging filter has been applied to the topograph to suppress short wavelength modulations. **E,** dI/dV in the same field of view as D. **F,** Amplitude of the FT of the dI/dV shown in E visualizing details of intra-pocket scattering in FeSe. The **q**-space region has been cropped to be similar in size to the area surrounded by the red circle in B.

One famous example are the quantum corrals created by manipulating Fe-atoms on top of a copper surface [86], another the standing waves caused by step edges in copper [87]. There is an intimate relationship between the oscillations in real space and the electronic structure in $\vec{k}$-space, see for example Ref. [83].

In the following we discuss this relationship in the context of iron-based superconductivity and FeSe. Figure 2.4A presents a constant current topograph of a single defect in FeSe, Figure 2.4B shows the amplitude of the Fourier transform of the constant current topograph. In real space strong Friedel oscillations emanate from the defect, and the atomic lattice is clearly distinguishable. Additionally, a peculiar pattern modifies the atomic contrast in the immediate vicinity of the defect which due to its shape and likely origin has been given the name 'geometric dumbbell' [53, 88, 89]. The amplitude of the Fourier transform consists of all these effects: static structure of the defect ('geometric dumbbell'), Friedel oscillations, atomic corrugation of the lattice. We point out that FeSe cleaves between Se-layers, and the atomic lattice visible is in all likelihood the Se-lattice.

Next, we focus on the contribution of the Friedel oscillations to the Fourier transform, and the two regions called $\mathbf{q}_{intra}$ and $\mathbf{q}_{inter}$ in scattering space to explain quasiparticle interference (QPI). In order to interpret scattering space we recall the schematic electronic structure of the iron-based superconductors in $\vec{k}$-space (Fig. 2.4C). For a scattering event both energy and momentum of the quasiparticles need to be conserved. The only accessible states to the quasiparticles in $\vec{k}$-space are restricted by the constant-energy-contours (CECs). In the pedagogical model in Fig. 2.4C the CECs are the circle and ellipses. For elastic scattering two scenarios exist: Either the quasiparticles scatter within a pocket (intra) or they scatter between pockets (inter). The difference for small pock-

ets is that inter-pocket scattering usually takes place for high $\vec{q}$-vectors whereas intra-pocket scattering is restricted to low $\vec{q}$-vectors.

For multiband systems with complex CECs the situation can become quite complicated and careful comparison and analysis of $\vec{k}$- and $\vec{q}$-space is necessary. An example of this situation for FeSe is shown in Figs. 2.4D-F. Panel D shows a constant current topograph of many defects, and E shows the differential conductance in the same field of view at -2.6 meV. Using $g(\vec{r}, V)$, we obtain energy resolved information of scattering space, and hence the electronic structure in $\vec{k}$-space. The amplitude of the Fourier transform of the conductance presented in F displays the non-trivial pattern of intensity in $\vec{q}$-space created by intra-pocket scattering and static defect structures.

ARPES measurements of the electronic structure in $\vec{k}$-space provide a useful starting point for the interpretation of QPI. Furthermore, polarized light sources can be utilized to deduce the symmetry of electronic states in $\vec{k}$-space. On the other hand STM has the advantage of excellent real space resolution, being able to measure with an applied magnetic field, and its energy resolution $\delta E < 100\mu eV$ is far superior for now. The combination of ARPES and SI-STM studies is thus the ideal approach in correlated electron systems in our opinion.

2.1.3 Bogoliubov quasiparticle interference

Inside a superconductor Bogoliubov quasiparticles scatter and interfere in a similar fashion, and Bogoliubov quasiparticle scattering interference (BQPI) imaging has become a very powerful technique to study Cooper pairing and measure $\Delta_i(\vec{k})$ [80–82, 90–92]. As BQPI imaging can be implemented at temperatures $T \leq 300mK$, the $\Delta_i(\vec{k})$ on multiple bands can be measured with energy

resolution $\delta E \approx 75\mu eV$ [81,82], a precision unachievable by any other approach. Before we give a more detailed example relevant to FeSe, we provide a straightforward and intuitive approach for BQPI studies in general: When a $\vec{k}$-space energy gap $\Delta_i(\vec{k})$ is anisotropic, the Bogoliubov quasiparticle dispersion $\epsilon_i(\vec{k})$ will exhibit closed constant-energy-contours which are roughly banana-shaped and surround Fermi surface points where $\Delta_i(\vec{k})$ is minimum [80–82]. Then, at a given energy E, the location of these banana tips can be determined because the maximum intensity BQPI modulations occur at wavevectors $\vec{q}_j(E)$ connecting them, due to their high joint density of states (JDOS) for scattering interference (Fig. 2.5B). Both the superconductors Cooper-pairing energy gap $\Delta_i(\vec{k})$ and Fermi surface on each band are then determined directly [80–82] by geometrically inverting the measured BQPI wavevector set $\vec{q}_j(E)$ in the energy range $\Delta_i^{min} < E < \Delta_i^{max}$.

Consider a standard Bogoliubov spectrum of a superconductor with an anisotropic gap $\Delta_{\mathbf{k}}$ similar to the one observed for S-doped FeSe for an ellipsoidal hole pocket with band structure $E_{\mathbf{k}}$ [69].

$$\epsilon_{\mathbf{k}} = \pm\sqrt{E_{\mathbf{k}}^2 + \Delta_{\mathbf{k}}^2} \tag{2.4}$$

Without loss of generality, we can then define a constant-energy-contour (CEC) in $\vec{k}$-space at a specified energy $\epsilon' > 0$ (because of the particle-hole symmetry, all observations also apply to $-\epsilon' < 0$) by the following equation:

$$\epsilon' = \pm\sqrt{E_{\mathbf{k}}^2 + \Delta_{\mathbf{k}}^2} \tag{2.5}$$

Lets further impose that the contour is within the superconducting gap meaning $\epsilon' < \Delta_{max}$. As long we are in the region of $\vec{k}$-space where $\epsilon' > \Delta_{\mathbf{k}}$, we expect two types of $\vec{k}$-space solutions, one with $E_{\mathbf{k}} < 0$ and one with $E_{\mathbf{k}} > 0$. These two types of solutions will connect at specific $\vec{k}$-points where $\epsilon' = \Delta_{\mathbf{k}}$, and hence $E_{\mathbf{k}} = 0$,

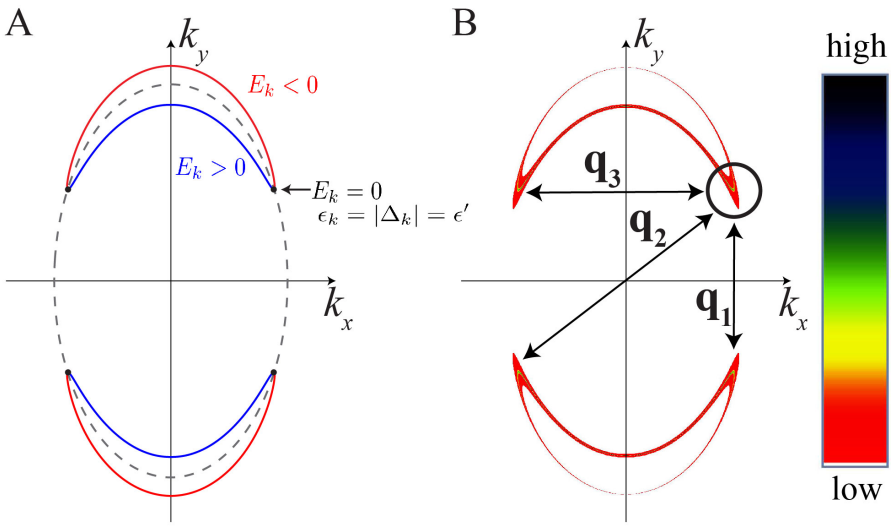

Figure 2.5: Scattering hot spots. **A,** Schematic showing a superconducting constant-energy-contour at a particular energy $\epsilon' > 0$ (above the chemical potential) for an ellipsoidal hole pocket (grey dashed line) with two-fold symmetric anisotropic gap that is maximum along k_x directions and minimum along the k_y directions. **B,** Spectral function $A(\mathbf{k}, \omega = \epsilon')$ corresponding to A. The spectral weight is greatest at the locations of 'banana tips'. The upper right 'banana tip' is marked with a black circle. Scattering is dominant between the tips as a consequence of the enhanced spectral weight. The wavevector triplet $\vec{q_1}$, $\vec{q_2}$, $\vec{q_3}$ connects these scattering hot spots.

to create closed contours reminiscent of bananas (Fig. 2.5A). Since $E_{\mathbf{k}} = 0$, these points (banana tips) lie on the normal state FS of the corresponding band by definition.

Within the JDOS picture, the modulations in the density of states (and hence dI/dV) due to impurity scattering will be dominated by the $\vec{q}$-vectors connecting $\vec{k}$-space regions with high spectral weight. For a superconductor with an anisotropic gap, such regions are exactly the tips of the CECs discussed above (Fig. 2.5B). For that reason, tracking the evolution of the $\vec{q}$-vectors associated with the tips of the CEC allows one to extract both the Fermi surface and the $\vec{k}$-space structure of the gap.

2.2 Phase Resolved Fourier Transform Scanning Tunneling Microscopy

So far our discussion of Fourier transform STM techniques was restricted to the amplitude of the Fourier transform. A collection of additional techniques becomes available when we consider the real and imaginary part of the Fourier transform individually. Research in the field of phase resolved FT-STM was pioneered by Slezak, Lawler, Fujita, Mesaros, Davis, and Kim in 2008-2011 [93–95].

2.2.1 Shift theorem of Fourier transforms

We start with the discussion of a basic theorem in the context of Fourier transforms, the shift theorem:

$$FT\{f(\vec{r}-\vec{r_0})\} = e^{-i\vec{q}\vec{r_0}} FT\{f(\vec{r})\} \tag{2.6}$$

A shift of a function away from the origin leads to multiplication with an oscillatory exponential term in Fourier space. Remembering that the Fourier transform of a Gaussian is just another Gaussian we can visualize the shift theorem with a simple example (Fig. 2.6).

Figure 2.6 is easy to understand when we rewrite the exponential in terms of a cosine and sine: $e^{-i\vec{q}\vec{r_0}} = cos(\vec{q}\vec{r_0}) - isin(\vec{q}\vec{r_0})$. Without a shift away from the origin, the Fourier transform is a purely real Gaussian. Once the Gaussian gets shifted the situation changes, and both a real and an imaginary part exist. If one looks closely the multiplication of the Gaussian with a cosine for the real part and sine for the imaginary part will become obvious. The bigger the shift away

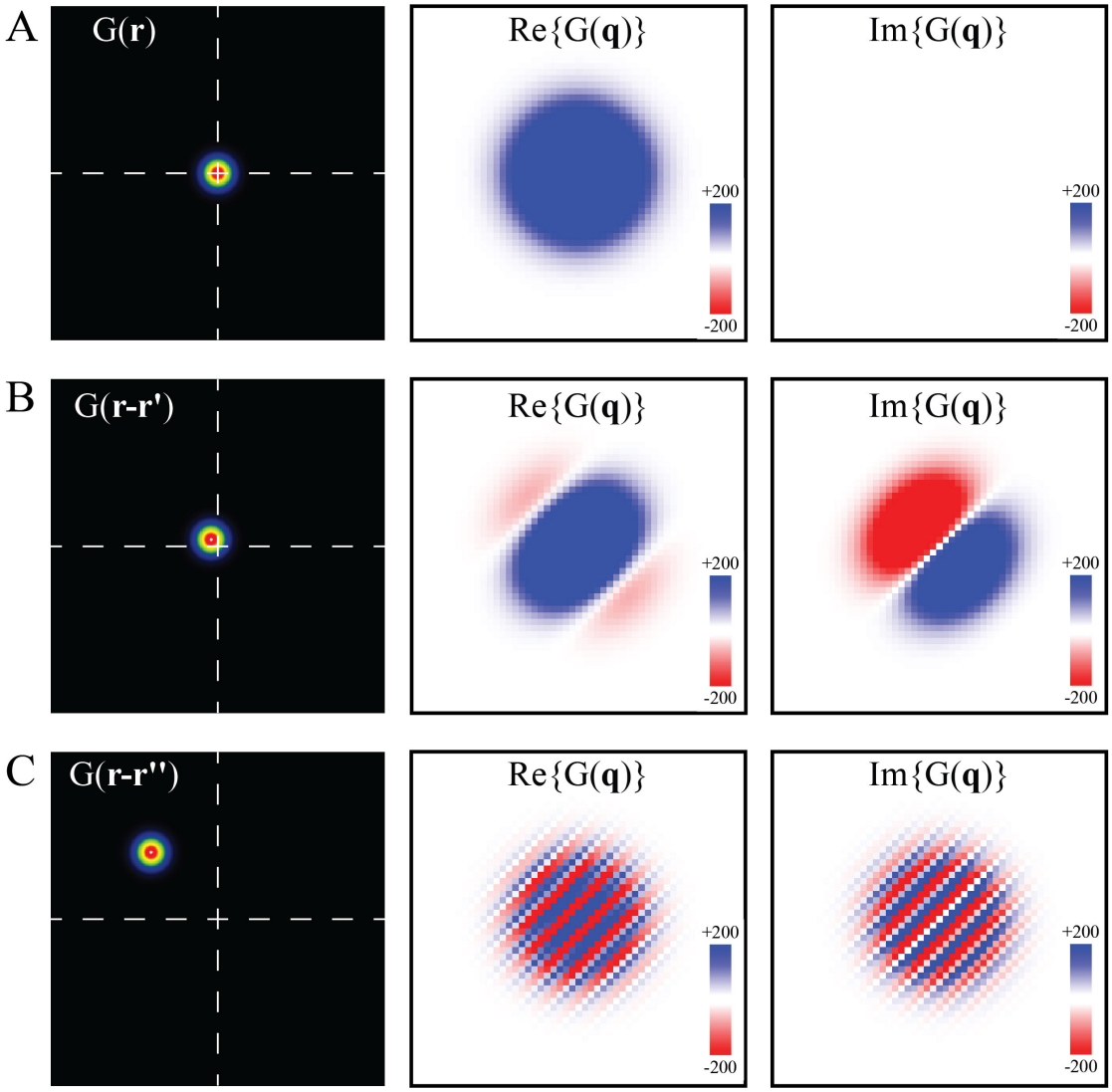

Figure 2.6: Shift theorem of Fourier transforms: Gaussian example. A, B, C, show how the real and imaginary part of the FT is affected by a shift **r′** or **r″** of the center of a Gaussian $G(\mathbf{r})$ away from the origin of the FT. The dashed white lines serve as a guide to the eye, and meet at the origin in real space.

from the origin the higher the frequency of the sine and cosine wave in Fourier space. Note that for practical, computational purposes the origin is arbitrarily determined by the computer software used to calculate the Fourier transform.

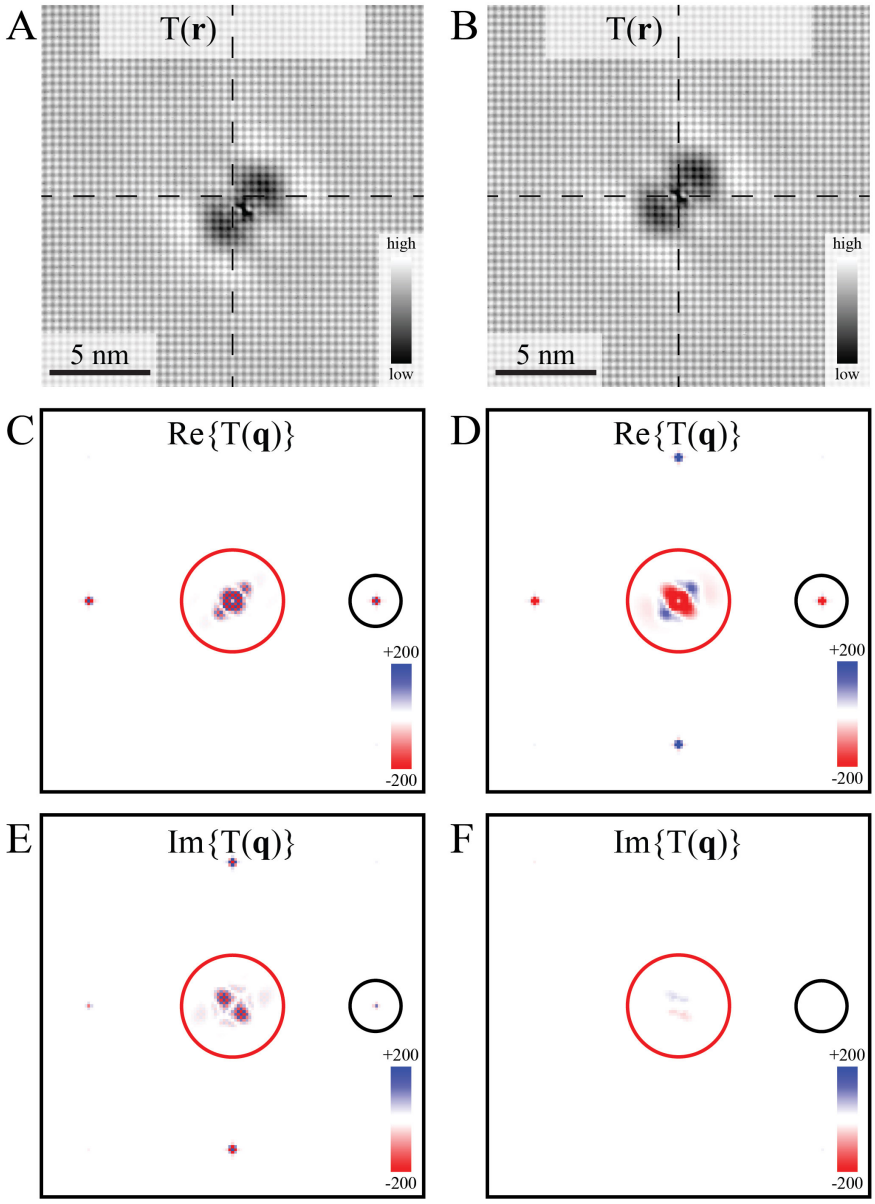

Figure 2.7: Shift theorem of Fourier transforms: FeSe example. A, B, Constant current topography of a single defect in FeSe. The size of the field of view is the same for A and B, but in B the topograph has additionally been processed so that the defect is at the origin. The dashed lines serve as a guide to the eye, and meet at the origin in real space. **C, D,** Real part of the FT of the topographic images in A and B. **E, F,** Imaginary part of the FT of the topographic images in A and B. Note the strong suppression of the imaginary part in the case of the shift corrected topograph. The red circle marks the region of intra-pocket scattering, and the black circle is positioned around one of the Se-Bragg peaks.

Next we revisit the single defect in FeSe. Here rotated by 45 degrees and in a slightly bigger field of view (Fig. 2.7). In the case of the Gaussian example, we determined the shift away from the origin by hand. In an experiment, a defect usually will not align with the origin because of drift of the piezo scanner tube for example. However, this is the beauty of the shift theorem. As we know what the origin should be, we can invert the shift, and through this process place the defect at the origin. This is the difference between panel A and B in Fig. 2.7. Panels C to F present the real and imaginary part of the Fourier transform before and after correcting the shift of the defect. The correction has two effects: (i) the phase of the real and imaginary part becomes well defined instead of oscillating rapidly between positive and negative values (checkerboard pattern visible in C and E); (ii) most of the signal of the Fourier transform is real. This is expected as the Fourier transform of a real function which is even under inversion symmetry is even and real. The Fourier transform of a real function which is odd under inversion is odd and imaginary. Before we discuss the significance of even and odd functions in more detail, we direct our attention to high $\vec{q}$.

2.2.2 Spatial phase, real and imaginary part

The reader with a keen eye for detail will have noticed that in Fig. 2.7D the $\vec{q}$-vectors corresponding to the Se-Bragg peaks have opposite sign for the x and y direction of the Se-lattice. This difference is rooted in the origin of the defect within the crystal structure of FeSe. The defect is most likely a vacancy in the Fe-lattice [88, 96] which means that we choose an Fe-site as the origin when we take the Fourier transform. Figure 2.8 illustrates the difference between a Se and an Fe origin.

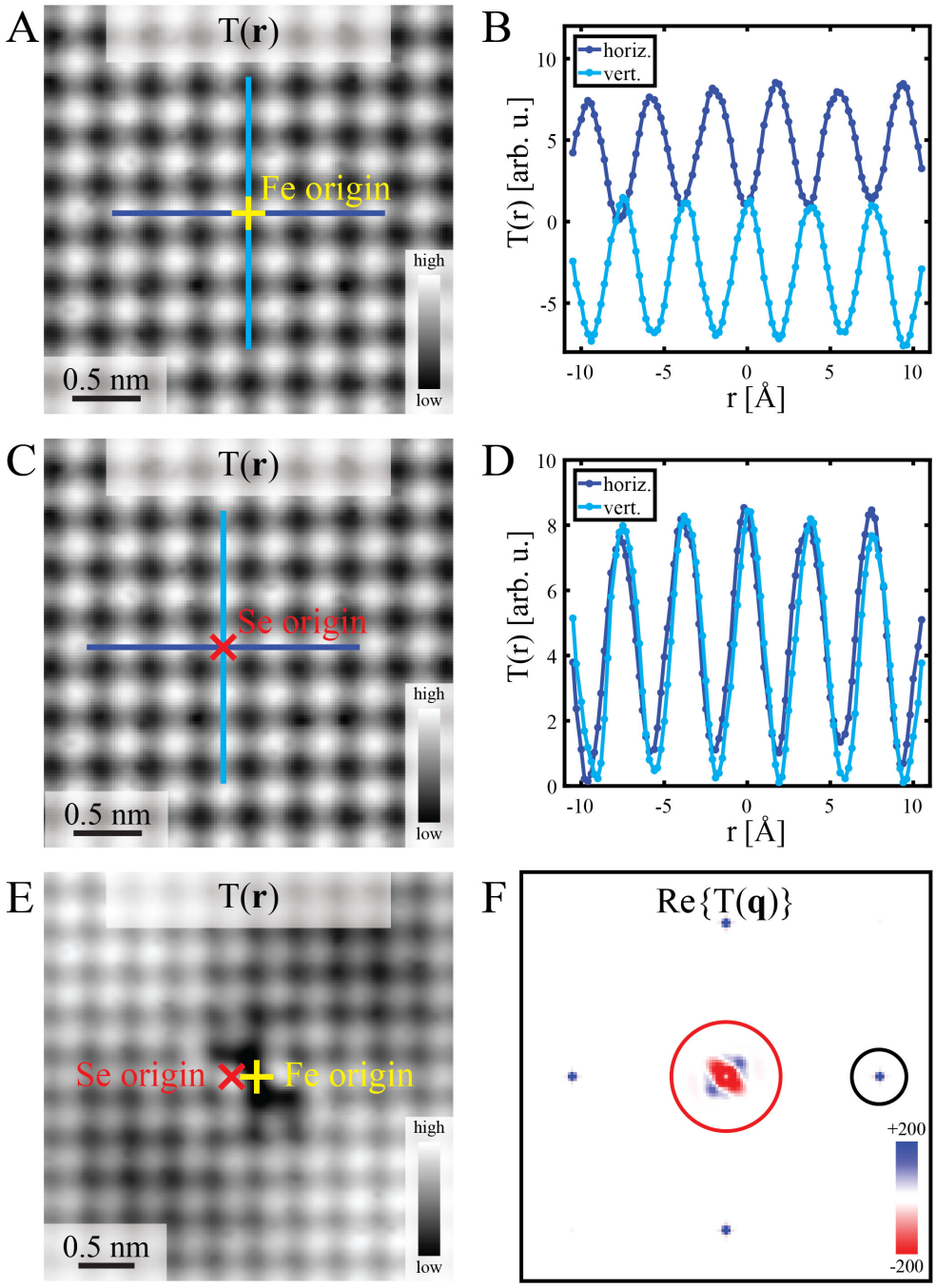

Figure 2.8: Phase resolved Fourier transform analysis. **A, B, C, D,** present line-cuts along the two perpendicular Se-Se-directions. In A and B the line-cut is centered on an Fe-atom, while in C and D the line-cut is centered on a Se-atom. In the first case the line-cut resembles two cosine waves that are half a wavelength out of phase. For the Se-origin the cuts are effectively in phase. **E,** Magnified view of the defect center of the topograph in Fig. 2.7B. **F,** Real part of the FT using the Se origin instead of the Fe origin as depicted in E. All Se-Bragg peaks are positive unlike in Fig. 2.7D.

Panels A to D depict line-cuts through the Se-lattice along its x and y direction both for the case of an Fe origin and a Se origin. The line-cuts resemble cosine waves in both cases with the difference that for an Fe origin the two waves are approximately π out of phase while a Se origin produces waves that are effectively in phase. A phase shift by π multiplies a cosine wave by -1, and this factor -1 explains the opposite sign for the two Se-Bragg peaks in Fig. 2.7D. Panel F shows the real part of the Fourier transform for the case where the Se-atom to the left of the Fe vacancy has been used as origin (Panel E). As expected all Se-Bragg peaks are positive.

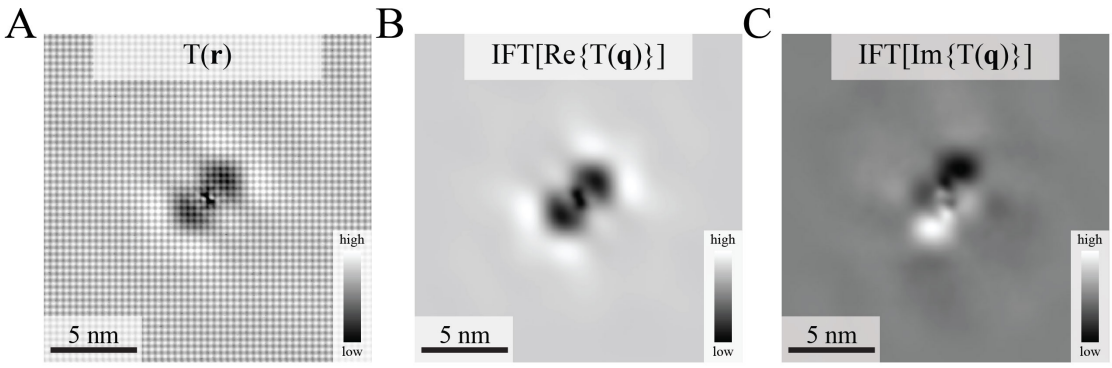

Figure 2.9: Decomposition of the even and odd part of the Friedel oscillations. **A,** Shift corrected constant current topography of single defect in FeSe. **B,** Inverse FT (IFT) of the real part multiplied with a Gaussian function to suppress short wavelength components. **C,** IFT of the imaginary part multiplied with a Gaussian function to suppress short wavelength components.

The case of a phase shift by π which is equivalent to a shift by half a wavelength is related to the question of even and odd function under inversion symmetry. If for example the phase shift was $\pi/2$ instead the cosine would become a sine. A sine is odd under inversion, and its Fourier transform is completely imaginary. Breaking of inversion symmetry is non-trivial, and can produce interesting physics as is the case for topological crystalline insulators [76]. The ability to distinguish real and imaginary part is therefore highly interesting. Us-

ing a Gaussian mask to suppress high $\vec{q}$ ($\rightarrow$ suppresses short wavelengths in real space) and calculating the inverse Fourier transform of the real and imaginary part (Fig. 2.7D, F) we can visualize the even and odd part of the Friedel oscillations around the defect (Fig. 2.9). Such inverse Fourier transform techniques applied to high $\vec{q}$ scattering could be a powerful tool in the search for domains inside a topological crystalline insulator [76] which is of interest for the novel physics that might exist at domain boundaries.

For the last part of this section we mention possible reasons for observing the breaking of inversion symmetry in experimental data where it is not expected. Firstly, there is the technical limitation of a finite amount of pixels when we correct the shift of a defect or atom with respect to the origin. In general, the higher the pixel count during data acquisition the better. Secondly, the tip itself is an unknown factor. It is highly unlikely that the tip is a perfectly spherically symmetric object so that the tunneling data is expected to possess some amount of inversion symmetry breaking. Thirdly, energy dependent studies additionally face the challenge that in a multi-orbital system tunneling could be dominated by different Wannier orbitals at different energies. This is especially problematic for studies across larges ranges of energy. For all these reasons, the study of inversion symmetry breaking requires extreme care in order to detect physically significant results.

2.2.3 Measuring sign changes of a superconducting gap

As we have mentioned in our introduction new techniques that could determine if a sign change between the different Fermi surface pockets exists are highly sought after. STM scattering experiments on Fe(Se, Te) [97] that rely

on differences between measurements with and without magnetic field applied have been criticized for a variety of reasons [98, 99]. Phase resolved FT-STM offers the opportunity for implementing a new BQPI technique for determining sign changes in the pairing symmetry without using magnetic fields [100]. It is based on conventional (non-magnetic) impurity scattering along with the realization that the particle-hole symmetry of interband scattering interference patterns depends on the relative sign of the energy-gaps on those bands [100]. As a result, the energy-symmetrized $\rho_+(\vec{q}, E)$ and energy-antisymmetrized $\rho_-(\vec{q}, E)$ phase-resolved Bogoliubov scattering interference amplitudes

$$\rho_\pm(\vec{q}, E) = Re\{g(\vec{q}, +E)\} \pm Re\{g(\vec{q}, -E)\} \tag{2.7}$$

have, at the $\vec{q}$ for interband scattering, distinct properties depending on the relative sign of the two gaps. Importantly, this new HAEM (Hirschfeld, Altenfeld, Eremin and Mazin) approach to measuring sign changes of superconducting gap structures, while not requiring variable temperature studies, does require phase-resolved imaging of BQPI in order to reliably discriminate $Re\{g(\vec{q}, E)\}$ from $Im\{g(\vec{q}, E)\}$. A point scatterer at an Fe-lattice site does not break inversion symmetry, and thus the whole BQPI signal is contained within the real part of the Fourier transform. For the reasons mentioned at the end of the last section, an experiment contains signal in the imaginary channel, as well, which needs to be reduced as much as possible, both during data acquisition and data processing.

We conclude this section with the predictions of the HAEM scheme for a two band toy model with flat DOS around the chemical potential. The goal is to distinguish between a sign-preserving and a sign-changing gap structure, as for example the ones shown in Figs. 2.10A, B.

In Fig. 2.10C we present the predicted $\rho_-(E)$ for sign-changing and sign-

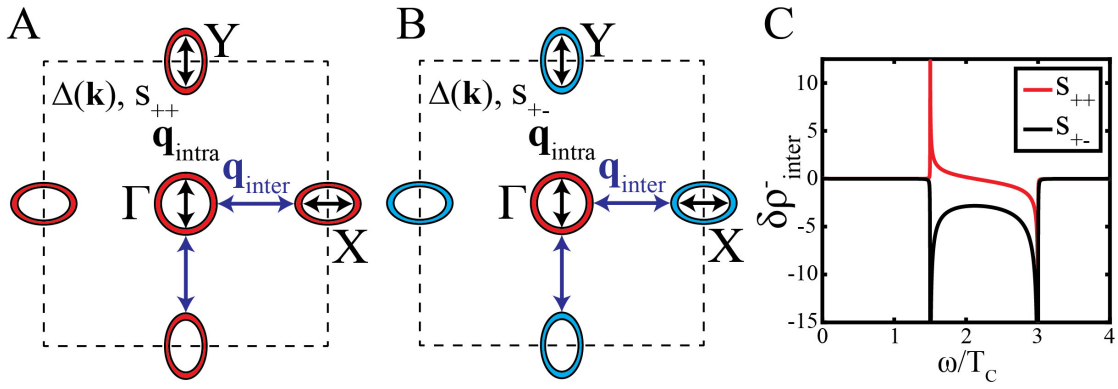

Figure 2.10: Determination of the sign of the superconducting gap using BQPI. A,B, Gap structure for the s_{++} (sign-preserving) and s_{+-} (sign-changing) scenario: Red and blue symbolize opposite sign of the gap in the latter. The dashed lines mark the 1 Fe unit cell Brillouin zone in both panels. Inter-pocket scattering connects gaps of same / different sign in the s_{++} / s_{+-} scenario. **C,** Anti-symmetrized LDOS for inter-pocket scattering calculated using a weak potential scatterer for a two-band model with flat DOS around the chemical potential. The important difference is the zero crossing for the case of s_{++} which is absent in the s_{+-} case. Gaps on the two bands were set to $3/T_C$ and $1.5/T_C$ in this example.

preserving superconductivity. The first difference between s_{++} and s_{+-} is that the scattering intensity is a lot stronger for the case of s_{+-} [100]. As comparison of relative intensities is always difficult for an experiment, the second difference is the crucial one: s_{++} crosses zero between the two gaps while s_{+-} does not [100]. This zero crossing is caused by the coherence factor for scattering between the two pockets.

In the case of the toy model presented in Fig. 2.10C the solution for inter-pocket scattering in the superconducting state is given as [100]:

$$\delta\rho^{-}_{inter}(\omega) = -2\pi^2 t_3 \rho_h \rho_e Im \frac{\omega^2 - \Delta_h\Delta_e}{\sqrt{\omega^2 - \Delta_h^2}\sqrt{\omega^2 - \Delta_e^2}} \tag{2.8}$$

Here Δ_h is the gap on the hole-like pocket in the center of the Brillouin zone, and Δ_e refers to the gap on the electron-like pocket at the X- or Y-point. ρ_h and ρ_e represent the DOS of the hole-like and electron-like pocket, respectively, and t_3

marks the strength of the potential scatterer. *Im* stands for taking the imaginary part of the fraction as ω possesses a small imaginary component. The product of the gaps Δ_h and Δ_e on the two pockets is evidently distinct for the case of sign-changing and sign-preserving gaps which creates the energy dependence of $\delta\rho^{-}_{inter}(\omega)$ presented in Fig. 2.10C.

While this particular toy model can be solved analytically for the whole Brillouin zone [100], in general the (anti)symmetrized functions $\rho_{\pm}(\vec{q}, E)$ must be integrated over a particular $\vec{q}$-space region. Specifically, we focus on

$$\rho_{-}(E) = \sum_{\delta\vec{q}} \rho_{-}(\vec{p_1} + \delta\vec{q}, E) \tag{2.9}$$

with radius δq confining $\vec{q}$-space to interband scattering processes between two distinct energy gaps. We will discuss the specifics of this numerical procedure in chapter 6.

CHAPTER 3

TIGHT-BINDING MODEL FOR FeSe

Both for the discussion of our FT-STM measurements and any theoretical simulations we require an accurate model of the electronic structure of FeSe in the vicinity of the chemical potential. For this purpose we introduce a tight-binding model (Fig. 3.1) that as we show in chapter 5 exhibits maximal simultaneous consistency with angle resolved photoemission [54, 55], quantum oscillations [56, 101], and the BQPI studies herein.

We remind the reader at this point that we parameterize the lattice by the two inequivalent Fe-Fe distances $a_{Fe} = 2.665$Å and $b_{Fe} = 2.655$Å in the orthorhombic/nematic phase (Fig. 3.1A). Furthermore, we define the x-axis (y-axis) to always be parallel to the orthorhombic a_{Fe}-axis (b_{Fe}-axis), so that our x/y coordinate system rotates when a twin boundary is crossed.

The Fermi surface (FS) is postulated to consist of three bands α, ε and δ (as shown schematically for $k_z = 0$ in Fig. 3.1B), and may be parameterized accurately using a tight-binding model [27, 102] that is fit simultaneously to several types of experimental observations. Surrounding the $\Gamma = (0, 0)$ point is an ellipsoidal hole-like α-band, whose FS $\vec{k}_\alpha(E = 0)$ has its major axis aligned to the orthorhombic b_{Fe}-axis; surrounding the $X = (\pi/a_{Fe}, 0)$ point is the electron-like ε-band whose bowtie FS $\vec{k}_\varepsilon(E = 0)$ has its major axis aligned to the orthorhombic a_{Fe}-axis. At the $Y = (0, \pi/b_{Fe})$ point, a δ-band FS should also exist but has remained stubbornly imperceptible to spectroscopic techniques.

Equally important to the topology of the band structure in a multiorbital system is the distribution of the orbital content in $\vec{k}$-space. Polarized LASER-ARPES on detwinned crystals provides valuable information about the orbital composition in $\vec{k}$-space [54, 103], and was used for the construction of the tight-binding

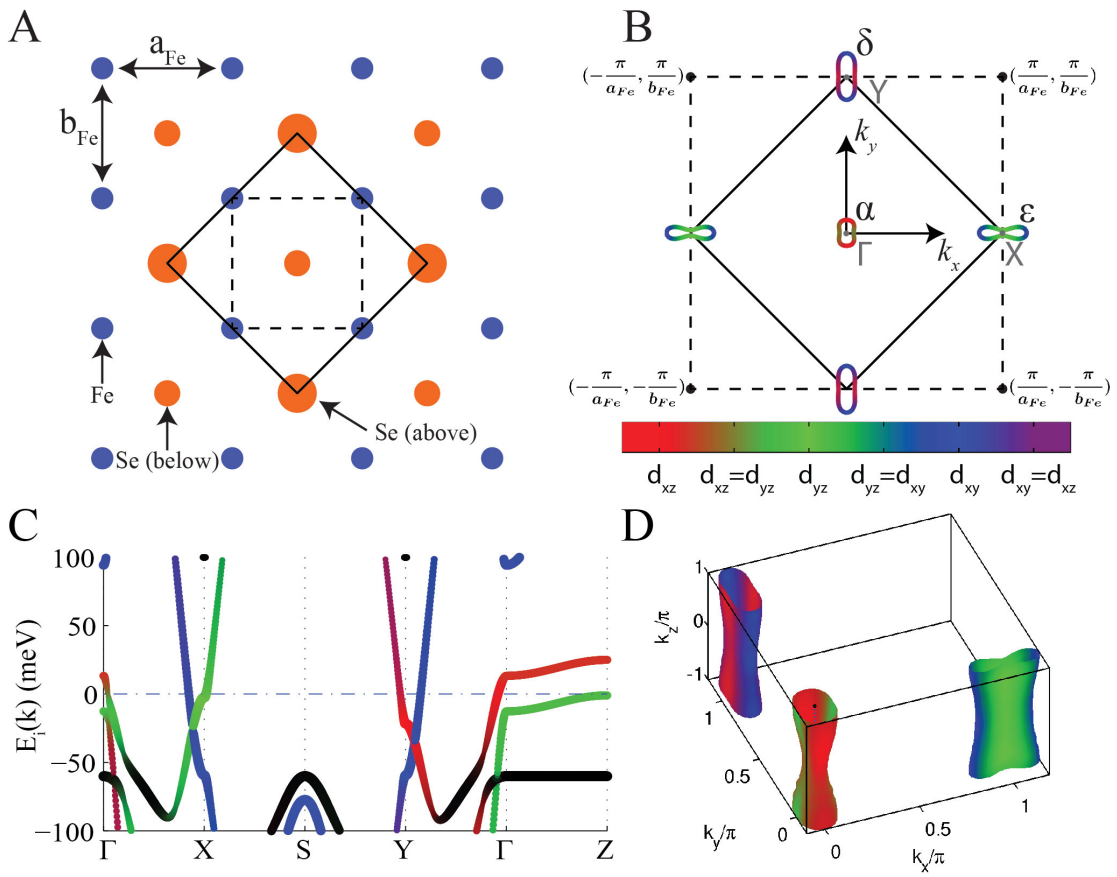

Figure 3.1: Tight-binding model for FeSe. **A,** Top view of FeSe crystal structure. Dashed lines represent the 1 Fe unit cell, and the 2 Fe unit cell is shown using solid lines. **B** Fermi surface at $k_z = 0$ consists of the hole-like α-band around $\Gamma = (0, 0)$ and an electron-like ε-band around $X = (\pi/a_{Fe}, 0)$. An anticipated third band, the δ-band around $X = (0, \pi/b_{Fe})$ has not yet been observed by spectroscopic techniques in the nematic phase.**C,** Band structure used as a basis for theoretical calculations. Line thickness represents the magnitude of the dominant orbital content. Thus, if the line gets thinner orbital content will be more mixed. Red = d_{xz}, green = d_{yz}, blue = d_{xy}, and black = $d_{x^2-y^2}$ or d_{z^2}. **D,** 3D Fermi surface including orbital character of our band structure model at low temperatures.

parameter set. In our resulting tight-binding model, the d_{yz} orbital content of the α-band Fermi surface has its maximum value along the x-axis (green Fig. 3.1B) while its d_{xz} orbital content peaks along the y-axis (red Fig. 3.1B) . Conversely, the d_{yz} orbital content of the ε-band FS is maximum along the y-axis (green Fig. 3.1B), and its d_{xy} orbital content reaches its highest point along the x-axis (blue

Fig. 3.1B); (Refs. [27, 54, 102, 103]). In this picture, the δ-pocket consists predominantly of d_{xy} mixed with d_{xz} orbital content.

3.1 Band structure parameters

Next we provide a detailed description of the individual parts of our band structure model. We use a band structure model, introduced in [26, 27], that includes a parameterization of site-centered (Δ_s) and bond-centered (Δ_b) orbital order as well as spin-orbit coupling [104]. Effects of interactions and correlations of the quasiparticles (in the normal state, but including the nematic order) are modeled by allowing the hoppings to be modified to match the spectral positions of the quasiparticle peaks observed in ARPES [54–56] and BQPI (this work). Note that this approach takes into account the real part of the self-energy corrections by fitting to the experimentally observed spectral positions $E_i(\mathbf{k})$. Specifically, the band structure is determined by the normal state Hamiltonian $H_N = H_0 + H_{OO} + H_{SOC}$, where H_0 (in real space notation) is given by

$$H_0 = \sum_{\mathbf{r},\mathbf{r'},a,b} t^{ab}_{\mathbf{r}-\mathbf{r'}} c^{\dagger}_{a,\mathbf{r}} c_{b,\mathbf{r'}} \tag{3.1}$$

where a, b are orbital labels, $\mathbf{r}$, $\mathbf{r'}$ are lattice sites, and t the hopping integral. For the orbital order term, we use the momentum space representation,

$$H_{OO} = \Delta_b(T) \sum_{\mathbf{k}} (cos(k_x) - cos(k_y))(n_{xz}(\mathbf{k}) + n_{yz}(\mathbf{k})) + \Delta_s(T) \sum_{\mathbf{k}} (n_{xz}(\mathbf{k}) - n_{yz}(\mathbf{k})) \tag{3.2}$$

Finally, the spin-orbit coupling is given by

$$H_{SOC} = \lambda \mathbf{L} \cdot \mathbf{S} \tag{3.3}$$

Keeping in mind the correspondence between a 5-band and a 10-band model [27] which is exact for $k_z = 0$ and $k_z = \pi$ in the absence of spin-orbit coupling

(SOC), we use a 5-band model to represent the band structure away from the band crossings that have splittings induced by SOC. However, the splitting at Γ needs to be taken into account [105,106]. The resulting band structure is shown in Fig. 3.1.

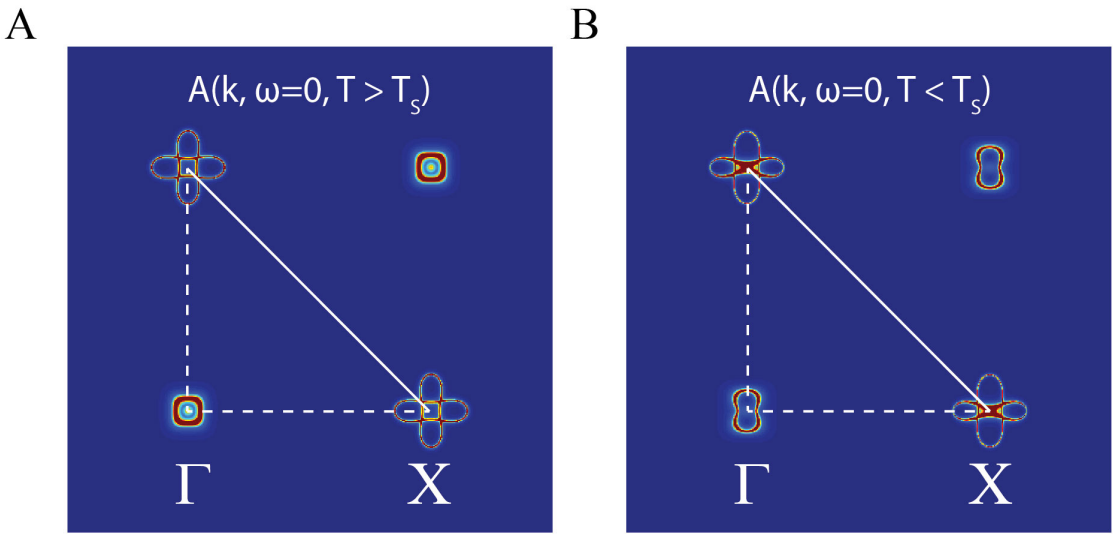

Figure 3.2: 10-band spectral function of the tight-binding model above and below the structural transition. **A,** Above the structural transition the orbital order terms are zero. As a consequence of this, both the hole-like pockets around Γ and the electron-like pockets around the X-point are C_4-symmetric. **B,** Below the structural transition, the orbital order terms break the C_4-symmetry of both the hole-like pocket around Γ and the electron-like pockets around X.
The solid white line marks the boundary of the 2 Fe unit cell Brillouin zone, and the dashed white lines represent symmetry axes about which the Fermi surface is mirror symmetric.

The values of the orbital order terms, as determined from experimental measurements of normal state QPI to be discussed elsewhere (A. Kostin et al., in preparation [107]), are $\Delta_s = 9.6meV$, $\Delta_b = -8.9meV$, and the SOC constant is fixed to $\lambda = 20meV$. These values also agree with the observed splitting above the nematic ordering temperature [106] assuming that the SOC is unaffected by temperature. In order to visualize the influence of the orbital order terms on the Fermi surface topology, we display the 10-band spectral functions at $\omega = 0$ both

above and below the structural transition T_S which correspond to $\Delta_s = 0meV$, $\Delta_b = 0meV$ and $\Delta_s = 9.6meV$, $\Delta_b = -8.9meV$, respectively (Fig. 3.2).

Above the structural transition, without orbital order, the Fermi surface is C_4-symmetric as reported by ARPES [55]. Overall, our band structure parametrization not only agrees in its spectral positions $E_i(\mathbf{k})$ with those of experimental observations, but is also consistent with deductions of the orbital content of the Fermi surface [54]. Moreover, at low energies it does not show any unexpected behavior as compared to investigations that include correlations [108]. Its general correspondence with experiment is discussed in chapter 5.

3.2 Nematic phase, twinned and detwinned measurements

The origin of the nematic phase in iron-based superconductors, and FeSe in particular, has been hotly debated ever since it was discovered [21, 30, 31, 109, 110]. Experiments find contradictory evidence for a nematic phase driven by orbital degrees of freedom [111] or by spin-fluctuations [44]. The strong coupling between the various degrees of freedom further complicates a clear distinction between different scenarios on the theoretical side, but the spin-fluctuation driven scenario is favored [20, 21, 30]. Related to the origin of the nematic phase is the question of orbital order in FeSe. A variety of types of orbital order has been suggested based on ARPES measurements [54–56, 103, 112].

For a realistic parametrization of the band structure, in addition to orbital order we need to consider a sizable spin-orbit coupling [106] and the evidence for strong orbital selective correlations which can modify the quasiparticle weights of the electrons [40]. The d_{xy} electrons are the most strongly correlated, and could become decoherent due to reduced quasiparticle weight [40]. In combi-

nation with our own (B)QPI and twinned as well as detwinned ARPES measurements shown in Figs. 3.3A, B the combination of mean-field orbital order terms was chosen eq. 3.2.

Figures 3.3C-F illustrate how our model of the electronic structure of FeSe is consistent with both twinned and detwinned ARPES measurements. Given our 10-orbital model for FeSe within one twin domain, the folding to the 2 Fe unit cell would give the ε-pocket aligned horizontally and the δ-pocket oriented vertically, as shown in panel C. If one now averages this $\vec{k}$-space structure (panel D) over the two orthorhombic domains, one ends up with a signal from a horizontally and vertically aligned ε-pocket, and in addition with a signal from a vertically and horizontally aligned δ-pocket which is demonstrated in panel D. This argument is true both without or with decoherence effects, as illustrated in panel D and F. This averaging over all twins yields the appearance of C_4 symmetry in excellent agreement with the observed spectral function by the most precise multi-domain ARPES studies on twinned crystals [55].

In a single domain, our model predicts a Fermi surface structure which breaks C_4 symmetry everywhere. And this situation is what is detected by single-domain (detwinned) ARPES studies of FeSe as shown in panel A above [54]. Our independent BQPI studies comprehensively detect phenomena that are completely consistent with this situation (panel E) as we will show in the remainder of this thesis.

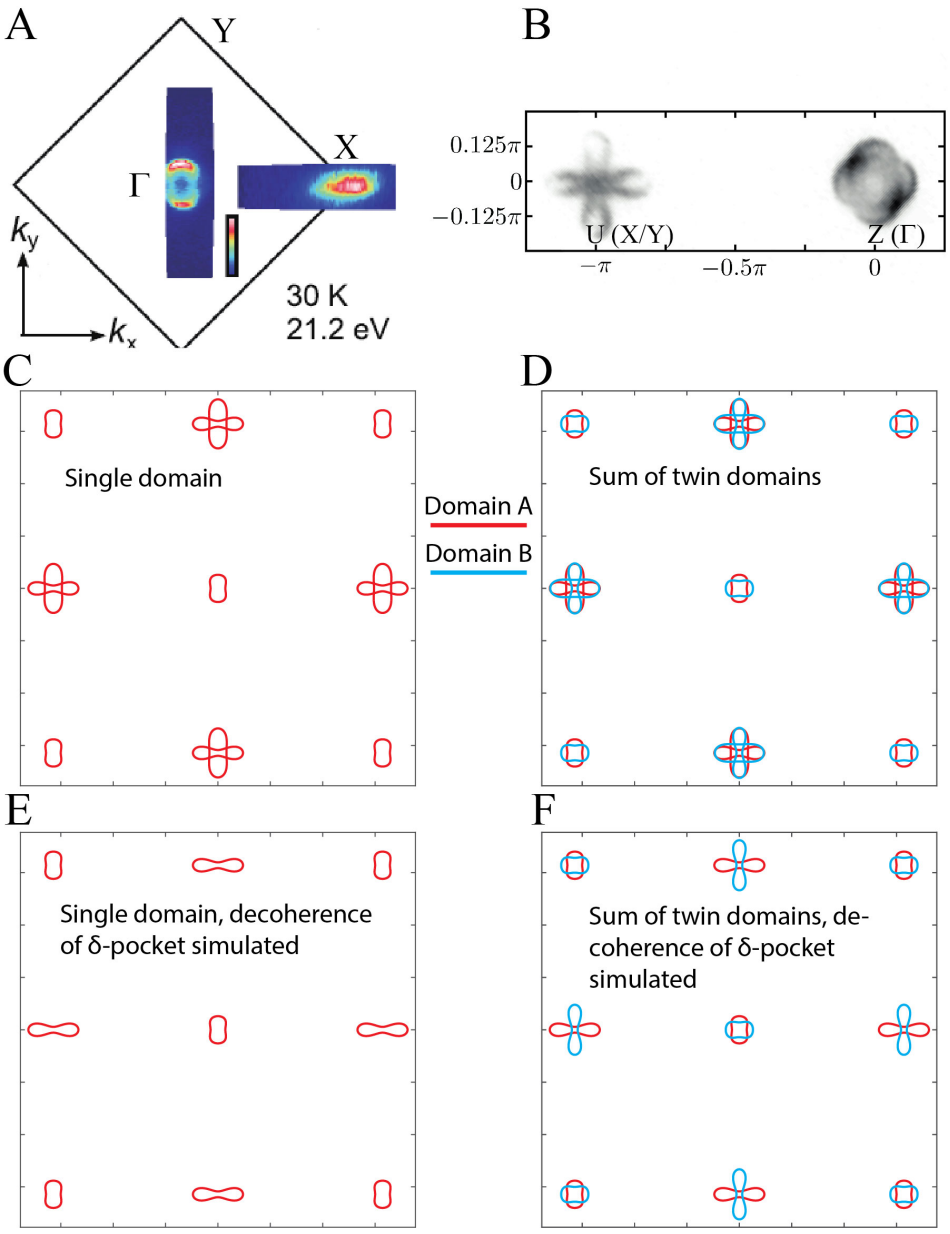

Figure 3.3: Twinned and detwinned measurements. **A,** Spectral function for $\omega = 0$ and $k_z = 0$ as measured using ARPES on detwinned FeSe crystals. Reproduced from reference [54]. **B,** Spectral function for $\omega = 0$ and $k_z = \pi$ as measured using ARPES on twinned FeSe crystals. Reproduced from reference [55]. **C,** Fermi surface for the ten-orbital version of our band structure model in a single orthorhombic domain. **D,** Fermi surface for the ten-orbital version of our band structure model when summed over two orthogonal orthorhombic domains. **E,** Fermi surface for the ten-orbital version of our band structure in a single domain without the delta pocket; this is to simulate decoherence of the d_{xy} states. **F,** Fermi surface for our ten-orbital band structure for the sum of two orthorhombic domains without the delta pocket.

CHAPTER 4

BOGOLIUBOV QUASIPARTICLE INTERFERENCE MEASUREMENTS IN FeSe

The FeSe single crystals measured via FT-STM were synthesized using KCl/AlCl3 chemical-vapour transport [113] and were thoroughly characterized using resistivity, magnetization and x-ray diffraction measurements [42, 44, 113, 114]. They show a structural transition at $T_S = 87 - 89K$ and a superconducting transition at $T_C = 8.7 - 8.8K$.

For study of the samples in the STM, each single crystal is glued flat onto the end of a cylindrical brass sample holder using silver epoxy H20E from Epotek. This provides excellent heat and electrical conductivity at low temperatures and yields a clean flat unstressed cleave of the crystal with high reliability. All samples are inserted slowly from a room temperature load-lock into the cryogenic environment and then cleaved in situ in cryogenic ultra-high vacuum at $T < 20K$.

Differential tunneling conductance $dI/dV(\vec{r}, eV) \equiv g(\vec{r}, eV)$ is measured at T = 280 mK, and as a function of both location $\vec{r}$ and electron energy $E = eV$ where V is the tip-sample bias voltage. We use fields of view in the range of 60 nm x 60 nm to 90 nm x 90 nm square and raster between 128x128 to 400x400 pixel square to get high signal-to-noise ratio and sufficient $\vec{q}$-space resolution, and a typical bias modulation of $\delta V = 100\mu eV$. The same measurements were carried out on both nematic domains of multiple crystals and all the results presented herein are supported by this data set.

4.1 Pedagogical Bogoliubov quasiparticle interference model

For guidance on what to expect in FeSe, we first consider a pedagogical QPI model, while emphasizing that Fermi surfaces and energy-gap structures derived using BQPI imaging do not depend on any such model [80–82]. ARPES measurements on the related material Fe(Se, S) provide an excellent starting point for the α-pocket, see also chapter 2. Given the α-band Fermi surface (fine dashed grey contour Fig. 4.1A) supporting an anisotropic $\Delta_\alpha(\vec{k})$ that has C_2 symmetry [53, 69], the constant-energy-contours would be as shown by the fine colored curves, with quasiparticle energy increasing as indicated by the color code. The tips of each Bogoliubov CEC banana are then indicated by colored dots similarly representing increasing energy. The predominant quasiparticle scattering should then occur between the four regions of maximum spectral weight as indicated here by each set of similarly colored dots (Fig. 4.1A), and discussed in chapter 2. Thus, for the α-band of FeSe we expect that a triplet of inequivalent BQPI wavevectors $\vec{q}_i^{\,\alpha}(E)$ $i = 1-3$ should exist (black arrows Fig. 4.1A). Scattering interference patterns with these wavevectors can be imaged using atomically-resolved differential tunneling conductance mapping $dI/dV(\vec{r}, E) \equiv g(\vec{r}, E)$. Maxima in the Fourier transform $g(\vec{q}, E)$ reveal the characteristic wavevectors $\vec{q}_i^{\,\alpha}(E)$ of dispersive BQPI modulations. The anticipated energy dependence of the $\vec{q}_i^{\,\alpha}(E)$ is then shown schematically in Fig. 4.1C using the same color code as for 'banana tips' in Fig. 4.1A.

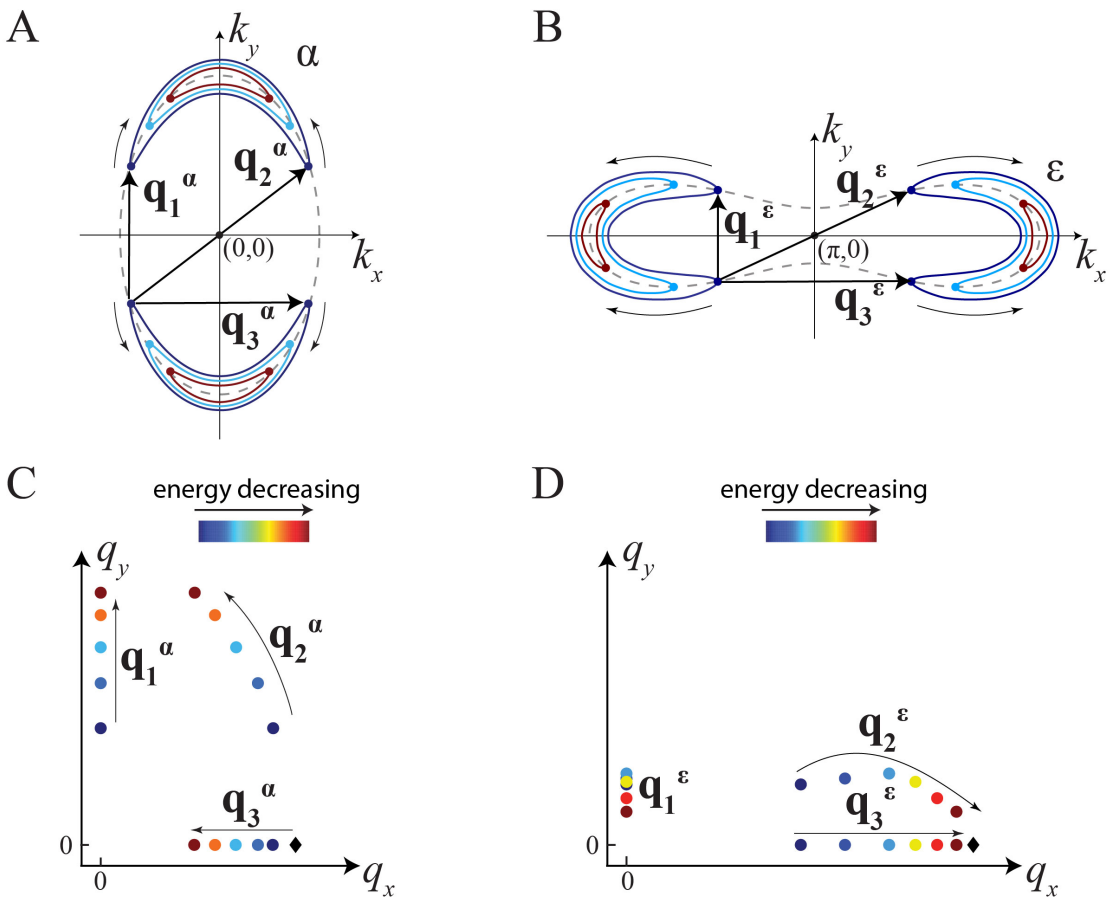

Figure 4.1: Pedagogical BQPI model for FeSe. **A,** Constant-energy-contours (CEC) of Bogoliubov quasiparticles for the gapped α-band around $\Gamma = (0,0)$. The CEC are color-coded to indicate increasing energy. A schematic, ellipsoidal normal state Fermi surface is shown using a grey dashed contour. Predominant scattering interference occurring between the 'tips' of the CEC should produce a triplet of characteristic BQPI wavevectors $\vec{q}_1^{\alpha}$, $\vec{q}_2^{\alpha}$, $\vec{q}_3^{\alpha}$ as indicated by black arrows. **B,** Constant-energy-contours (CEC) of Bogoliubov quasiparticles for the gapped ε-band around $X = (\pi/a_{Fe}, 0)$. These are color-coded to indicate increasing energy. Normal state Fermi surface is shown using a grey dashed contour. Predominant scattering interference occurring between the 'tips' of the CEC should produce a triplet of characteristic BQPI wavevectors $\vec{q}_1^{\varepsilon}$, $\vec{q}_2^{\varepsilon}$, $\vec{q}_3^{\varepsilon}$ as indicated by black arrows. **C,** The expected energy dependence of the α-band wavevector triplet $\vec{q}_1^{\alpha}$, $\vec{q}_2^{\alpha}$, $\vec{q}_3^{\alpha}$ in 1C; these are color-coded to indicate increasing energy. The black diamond symbolizes the starting point of $\vec{q}_3^{\alpha}$ where $\Delta_\alpha = max$. **D,** The expected energy dependence for the ε-band wavevector triplet $\vec{q}_1^{\varepsilon}$, $\vec{q}_2^{\varepsilon}$, $\vec{q}_3^{\varepsilon}$ color-coded by energy. The black diamond symbolizes the end point of $\vec{q}_2^{\varepsilon}$ where $\Delta_\varepsilon = min$.

For each energy $\Delta_i^{min} < E < \Delta_i^{max}$ the positions of the four CEC 'banana tips' $(\pm k_x(E), \pm k_y(E))_\alpha$ can be determined by inverting

$$\vec{q_1}^{\alpha} = (0, 2k_y) \tag{4.1}$$

$$\vec{q_3}^{\alpha} = (2k_x, 0) \tag{4.2}$$

$$\vec{q_2}^{\alpha} = (2k_x, 2k_y) \tag{4.3}$$

If a C_2-symmetric energy gap $\Delta_\delta(\vec{k})$ existed on the δ-band surrounding $Y = (0, \pi/b_{Fe})$ it might be expected to behave very comparably. Similarly, if a C_2-symmetric energy gap $\Delta_\varepsilon(\vec{k})$ existed on the bowtie ε-band Fermi surface surrounding $X = (\pi/a_{Fe})$ (grey contour Fig. 4.1B) it would exhibit Bogoliubov CEC as in Fig. 4.1B; another BQPI triplet $\vec{q}_i^{\varepsilon}(E)$ $i = 1 - 3$ (black arrows Fig. 4.1B) should then exist whose energy dependence is shown schematically in Fig. 4.1D using the equivalent color code. Here again the locus of four CEC 'banana tips' $(\pm k_x(E), \pm k_y(E))_\varepsilon$ is determined from the equivalent of eqs. 4.1 - 4.3. Thus, detection of BQPI phenomena of the type shown schematically in Figs. 4.1A-D, and their use to measure the FeSe Fermi surfaces $\vec{k}_\alpha(E = 0); \vec{k}_\varepsilon(E = 0)$, along with the structure and sign of their superconducting energy gaps $\Delta_\alpha(\vec{k})$ and $\Delta_\varepsilon(\vec{k})$, are the objectives for our study.

4.2 Crystal symmetry

Figure 4.2 presents SI-STM measurements across an orthorhombic twin boundary. We discuss the superconducting tunneling spectrum in A in detail later, and concentrate for now on the constant current topography and dI/dV images in B-D. Both in the topography and in the dI/dV images the highly anisotropic C_2-symmetric Friedel oscillations rotate when the twin boundary is crossed. This

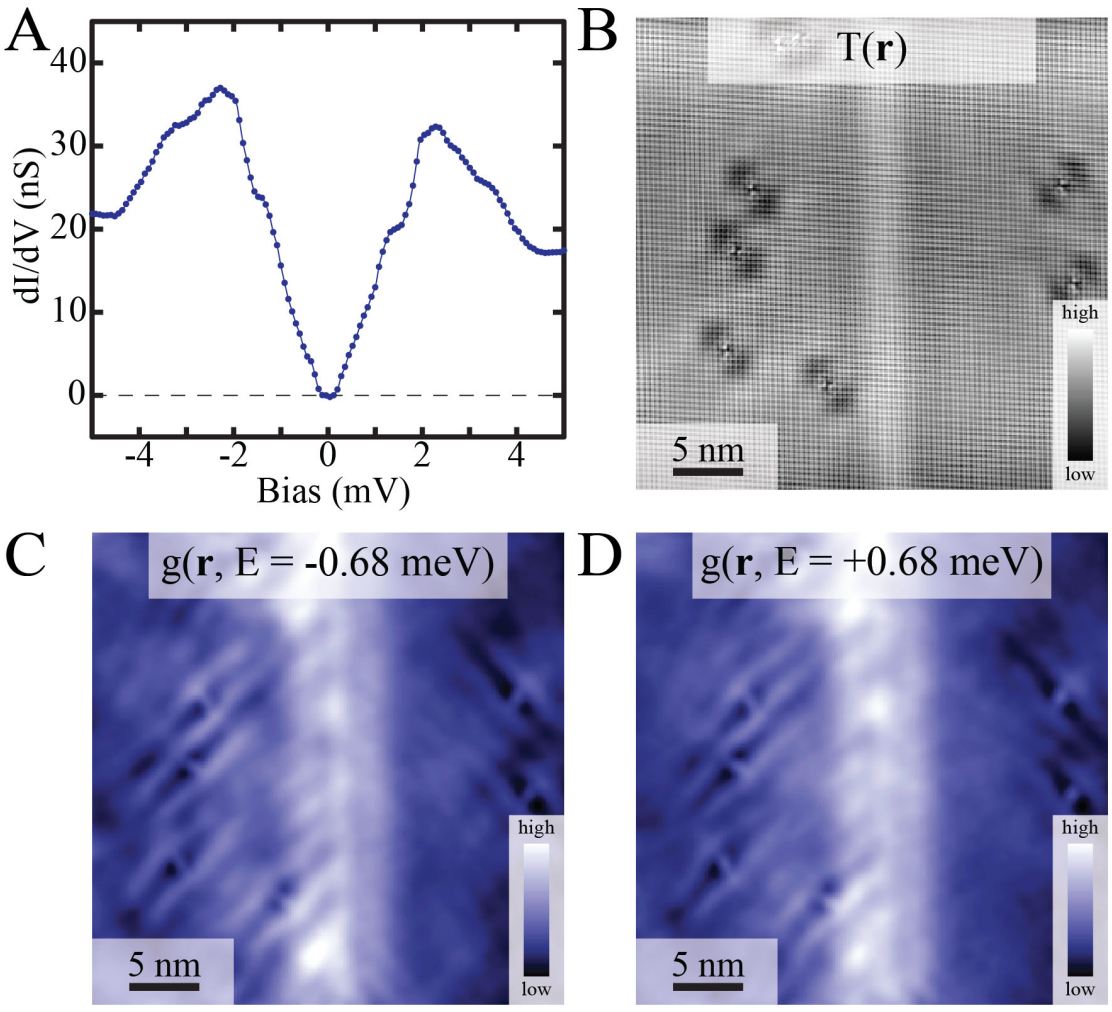

Figure 4.2: Rotation of BQPI across orthorhombic twin boundary. **A,** High-resolution spectrum of the superconducting gap in FeSe. **B,** Topography across a twin boundary. Note the rotation of the Friedel oscillations between the two orthorhombic domains. **C,** dI/dV map inside the superconducting gap below the chemical potential in the same field of view as B. **D,** dI/dV map inside the superconducting gap above the chemical potential in the same field of view as B.
Both in C and D short wavelength components were filtered in order to enhance the visibility of the BQPI Friedel response around the defects.

is important, as it confirms that the anisotropy of experimental quantities is not a property of the tip, but instead inherent to the electronic structure of FeSe in the orthorhombic / nematic phase. Furthermore, the BQPI oscillations in the dI/dV (panels C and D) are particle-hole symmetric with respect to the chemi-

cal potential as expected for Bogoliubov quasiparticles.

The symmetry of the crystal structure can be used to increase the signal-to-noise ratio of (B)QPI measurements. In Fig. 4.3 we present the sequence of steps used to optimize the signal-to-noise ratio of the BQPI data. The three steps are symmetrization, averaging, and Gaussian core subtraction in Fourier space. We would like to emphasize that no unfolding of BQPI data with respect to the 1 Fe and 2 Fe unit cell picture takes place within these steps, and that the symmetrization does not enforce C_2 symmetry on the data.

For the symmetrization we take advantage of the mirror symmetry axes present in the underlying $\vec{k}$-space structure, see also Fig. 3.2. As BQPI consists of scattering between parts of constant-energy-contours in $\vec{k}$-space these mirror symmetry axes carry over into $\vec{q}$-space. The raw amplitude Fourier transform $|g(\vec{q}, E)|$ is symmetrized via reflection about the mirror symmetry axes displayed in Fig. 4.3A.

In order to further increase the signal-to-noise ratio we use a three-by-three pixel averaging filter on the symmetrized amplitude Fourier transform $|g(\vec{q}, E)|$ in Fig. 4.3B. The result is shown in panel C. The last step is a Gaussian core subtraction in Fourier space which corresponds to a long wavelength filter in real space. As can be seen in D this subtracts intensity for very small $\vec{q}$-vectors. The labeling and assignment of $\vec{q}$-vectors in A-D can be understood based on the pedagogical QPI model presented in Fig. 4.1.

4.3 Different tunneling tips

Three types of tips were repeatably observed during our studies. Figure 4.4 presents conductance maps $g(\vec{r}, E)$ at -1.1 meV measured with the three different

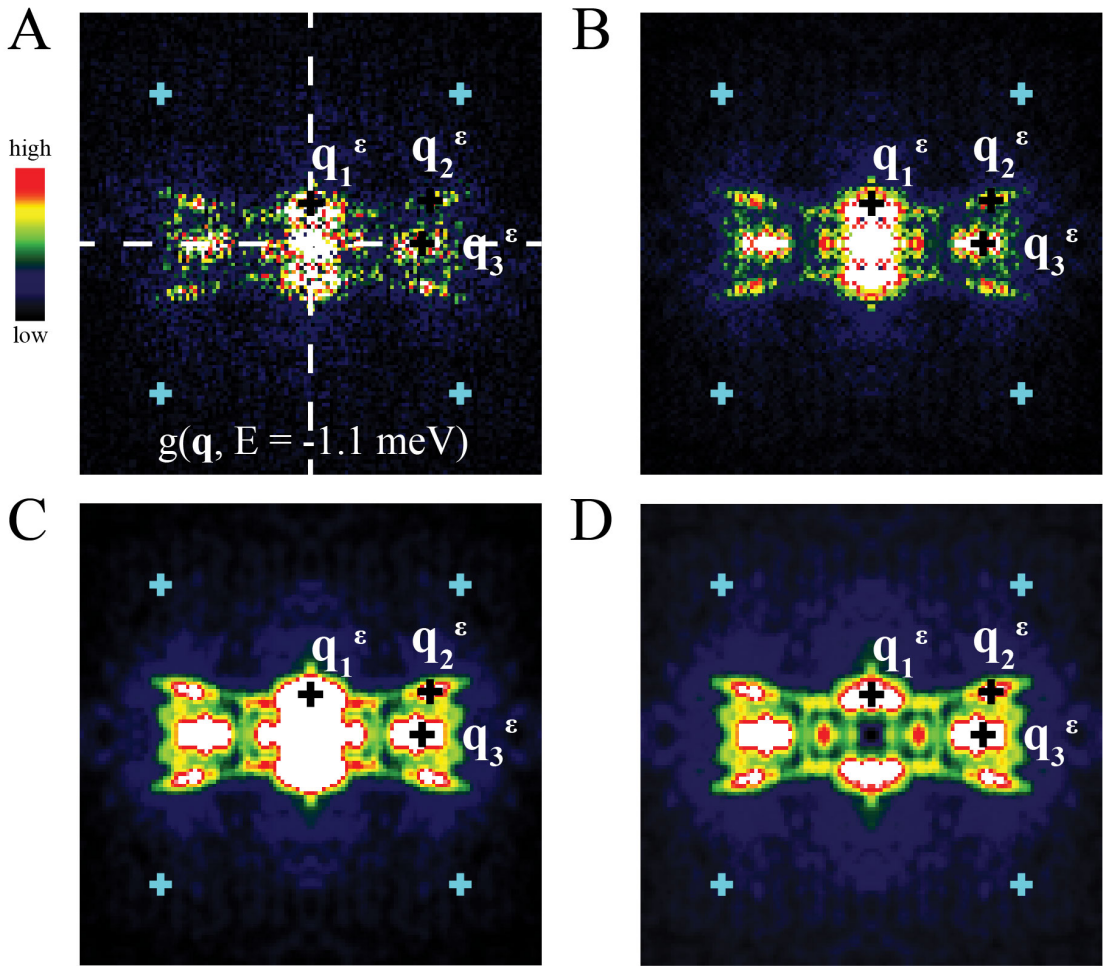

Figure 4.3: BQPI data processing steps. **A,** Raw amplitude Fourier transform $|g(\vec{q}, E)|$ as obtained from measured differential conductance. The dashed white lines represent mirror symmetry axes of the Brillouin zone, see also Fig. 3.2. **B,** Symmetrized amplitude Fourier transform $|g(\vec{q}, E)|$ created by reflection about the mirror symmetry axes displayed in A. **C,** Symmetrized and averaged amplitude Fourier transform $|g(\vec{q}, E)|$; after symmetrization a three-by-three pixel averaging filter is utilized in order to further increase signal-to-noise. **D,** Symmetrized, averaged, and core subtracted amplitude Fourier transform $|g(\vec{q}, E)|$; in the last step a Gaussian core is subtracted in Fourier space which corresponds to a long wavelength filter in real space.
In all panels cyan crosses mark $(\pm\frac{2\pi}{8a_{Fe}}, \pm\frac{2\pi}{8b_{Fe}})$ positions.

tip types (for clarity shown in smaller fields of view in $\vec{q}$-space than the original data) along with the amplitude of their corresponding Fourier transforms $|g(\vec{q}, E)|$. The tips differ in their atomic sharpness, with the sharper tips being

created when the atomic configuration at the end of the tip changed while scanning across the surface at low tunneling junction resistance. Panels A and B represent the expected case where the STM tip is sensitive to the BQPI signal from both the α- and ε-pocket simultaneously. It is possible in principle to extract the FS and energy gaps $\Delta_\alpha(\vec{k})$ and $\Delta_\varepsilon(\vec{k})$ from these data alone. However, we found that it is also possible to simplify the situation and to measure the properties of the two bands individually. Panels C and D contain the results for a tip that is sensitive primarily to the α-pocket. This is achieved by using a lower spatial resolution tip which is far more sensitive to the long wavelength BQPI modulations that occur in intra-band scattering in the center of the Brillouin zone. Alternatively, panels E and F show the results form a tip that is predominantly sensitive to the scattering interference from the ε-pocket. Momentum dependence of tunneling tips is discussed in more detail in Ref. [73]. In the following we will call these tips tip $\alpha\varepsilon$, tip α, and tip ε. All panels in Fig. 4.4 and Fig. 4.5 have been labeled depending on which tip was used during the measurement. As can be seen from the atomic contrast in Fig. 4.4A, E the tips sensitive to the ε-pocket BQPI possess excellent real-space resolution.

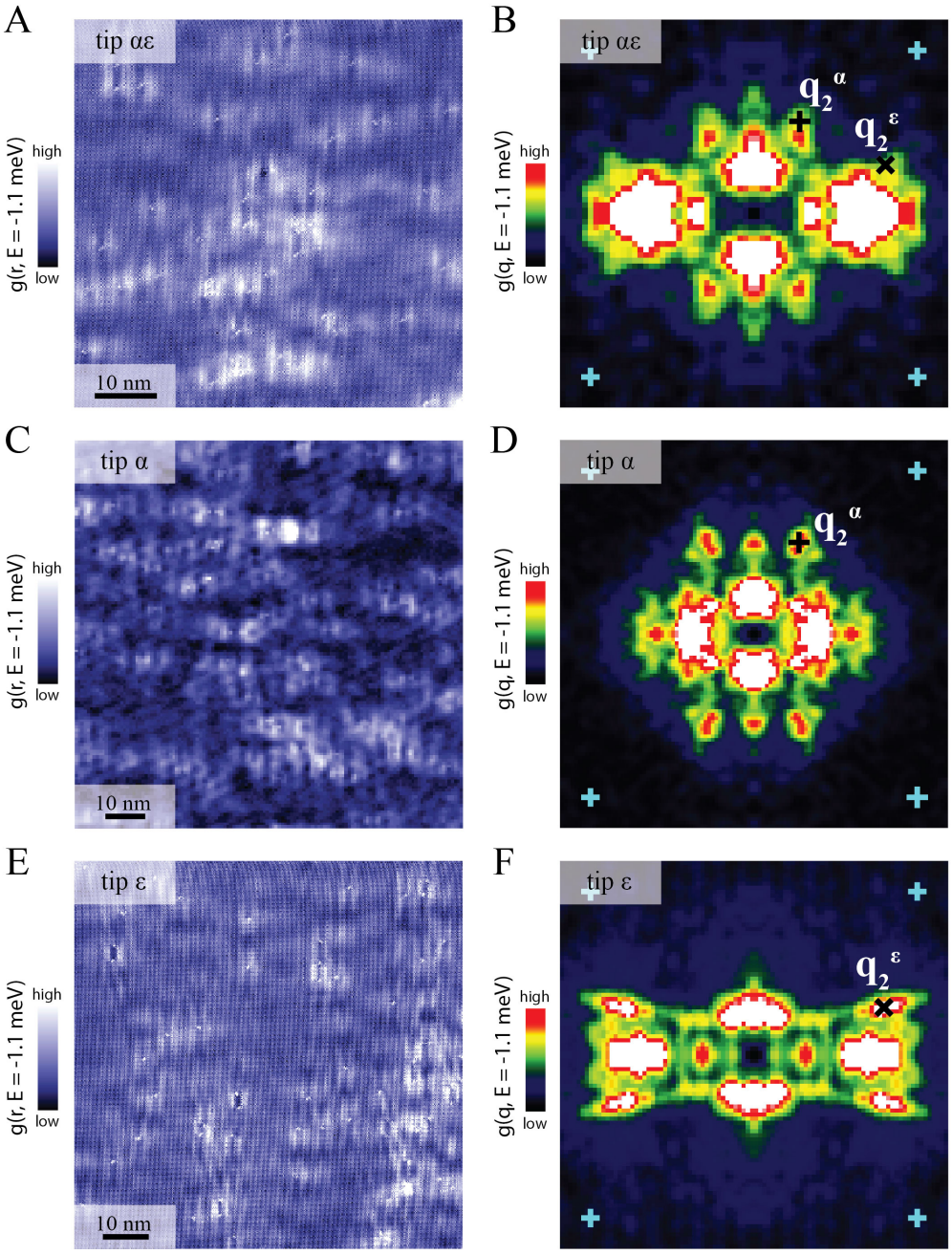

Figure 4.4: Different tunneling tips. A,C,E, Differential tunneling conductance images $g(\vec{r}, E)$ for three different tips at -1.1 meV. **B,D,F,** Symmetrized, averaged, and core subtracted amplitude Fourier transform $|g(\vec{q}, E)|$ of the conductance maps in A, C, E. The tip in A and B is simultaneously sensitive to both α- and ε-band BQPI. The tip in C and D is sensitive predominantly to the α-pocket because its spatial resolution is low and so can only detect long wavelength BQPI. The tip in E and F instead mostly displays sensitivity to the ε-pocket. Cyan crosses mark $(\pm\frac{2\pi}{8a_{Fe}}, \pm\frac{2\pi}{8b_{Fe}})$ positions.

In order to compare real-space resolution and $\vec{q}$-space sensitivity to the tip that is primarily sensitive to the α-pocket BQPI we show in Figs. 4.5A, B constant current topographs recorded for the same setup current and setup bias but with two different tips: tip α and tip $\alpha\varepsilon$. The topographs and the corresponding am-

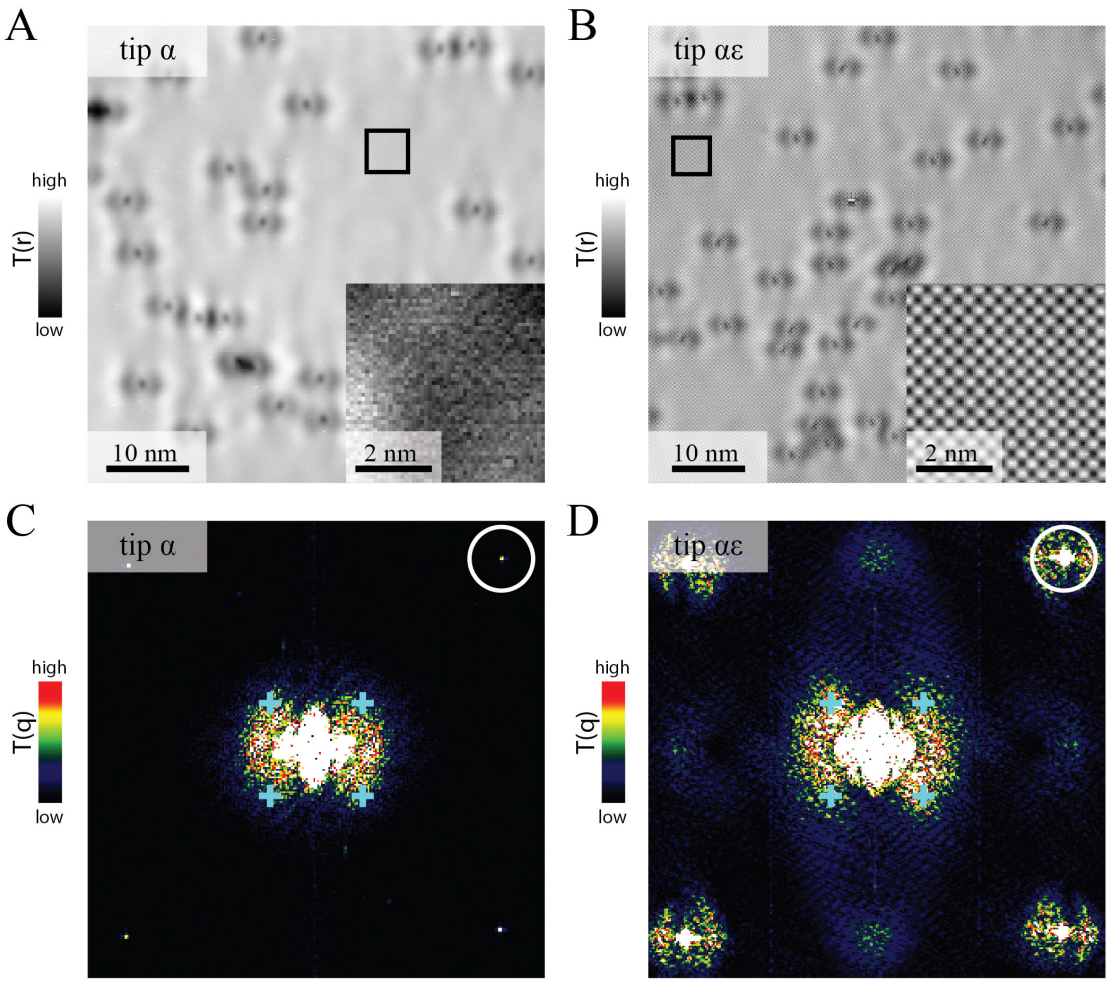

Figure 4.5: Relationship between r- and q-space sensitivity of different tunneling tips. A,B, Constant current topography in the same orthorhombic domain in FeSe with two of the tips discussed in additional detail in the text and Fig. 4.4. The inset shows the topographic region marked by the black box. The ability to resolve atoms differs strongly between the two tips. **C,D,** Amplitude of the Fourier transform of the topographs in A and B. The tip with superior spatial resolution detects scattering at high **q**-values, not observed in the Fourier transform of the lower spatial resolution tip.
The white circle marks $(+\frac{\pi}{a_{Fe}}, +\frac{\pi}{b_{Fe}})$. Cyan crosses mark $(\pm\frac{2\pi}{8a_{Fe}}, \pm\frac{2\pi}{8b_{Fe}})$ positions.

plitudes of their Fourier transforms in Figs. 4.4C, D exhibit the same behavior as seen in Fig. 4.4. Superior real space resolution goes hand in hand with sensitivity to high-$\vec{q}$ phenomena as expected. The sharper tip is sensitive to even the signal from Umklapp-scattering processes around the Se-Bragg peak which has been marked with a white circle. Additionally, the sharper tip is sensitive to interband scattering between the hole pocket at $\Gamma = (0,0)$ and the electron pocket at $X = (\pi/a_{Fe}, 0)$ which is absent for the lower resolution α-tip, see Fig. 4.5C. We find identical high-$\vec{q}$ properties for the atomically sharp tip which predominantly detects the ε-pocket for low $\vec{q}$-values, tip ε. We assign the BQPI triplet of wavevectors $q_i^{\vec{\alpha},\varepsilon}(E)$ to the α- and ε-pocket based on the energy evolution of their intensity-maxima, which can be compared to JDOS (Joint Density of States) simulations (chapter 5) of the expected BQPI using our tight-binding model introduced in chapter 3.

4.4 Measured Bogoliubov quasiparticle interference

In the following we present BQPI measurement for all three types of tips. We reiterate the measurement conditions: Differential tunneling conductance $dI/dV(\vec{r},E) \equiv g(\vec{r},E)$ is imaged at $T = 280mK$ both as a function of location $\vec{r}$ and electron energy E. As the Fermi surface pockets are so miniscule in area, the expected range of dispersive intraband BQPI wavevectors is very limited $0 < |\vec{q}_i^{\alpha,\varepsilon}(E)| < 0.25(\frac{2\pi}{a_{Fe}})$, while the interband BQPI necessitates resolving wavevectors $\geq \frac{\pi}{a_{Fe}}$. To achieve the $\vec{q}$-space resolution $|\delta q_i^{\alpha,\varepsilon}| \leq 0.01(\frac{2\pi}{a_{Fe}})$ required to discriminate the energy evolution of BQPI on both α-band and ε-band necessitates high-precision $g(\vec{r},E)$ imaging in very large fields of view, typically between 60X60 nm^2 and 90X90 nm^2. BQPI measurements for the α- and ε-tip are

depicted in Fig. 4.6.

Local maxima of $|g(\vec{q}, E)|$, the amplitude Fourier transform of $g(\vec{r}, E)$, are then used to determine the characteristic wavevectors $\vec{q}_i^{\,\alpha}(E)$ and $\vec{q}_i^{\,\varepsilon}(E)$ of dispersive modulations of BQPI. Two triplets $\vec{q}_i^{\,\alpha}(E)$ and $\vec{q}_i^{\,\varepsilon}(E)$ can be identified based on the energy evolution of the BQPI pattern. The triplets become a set of eight through symmetry operations, and are marked by black crosses in Fig. 4.6.

Similarly, we measure the energy evolution of BQPI for an $\alpha\varepsilon$-tip Fig. 4.7. The triplets of BQPI wavevectors are marked using the same symbols as in Fig. 4.6. We find very good agreement between the energy evolution of BQPI measured for the 'isolated' α- and ε- tips and the 'combined' $\alpha\varepsilon$-tip. However, it is clear that the 'isolated' tips reduce the complexity of the BQPI patterns significantly. Additional structure in $\vec{q}$-space comes for example from the geometric, static structures of the defects. Finally, we point out that the BQPI is particle-hole symmetric as expected for Bogoliubov quasiparticles in a superconductor.

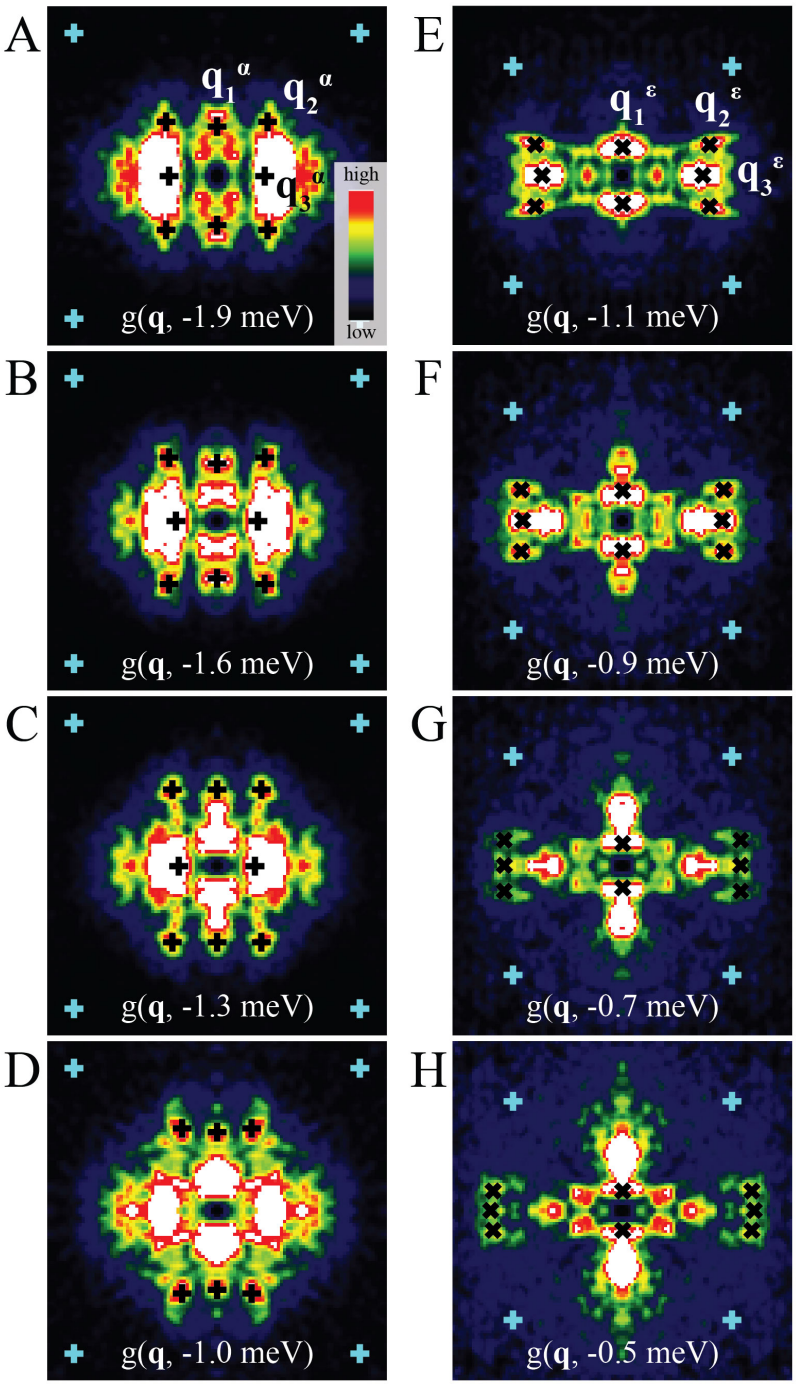

Figure 4.6: BQPI for an α- and ε-tip configuration. A-D, Symmetrized, averaged, and core subtracted amplitude Fourier transform $|g(\vec{q}, E)|$ at four energies inside the superconducting gap Δ_α. Black crosses mark the extracted **q**-vectors expected from the 'banana tips' model. **E-H,** Symmetrized, averaged, and core subtracted amplitude Fourier transform $|g(\vec{q}, E)|$ at four energies inside the superconducting gap Δ_ε. Black crosses mark the extracted **q**-vectors expected from the 'banana tips' model.
Cyan crosses mark $(\pm\frac{2\pi}{8a_{Fe}}, \pm\frac{2\pi}{8b_{Fe}})$ positions.

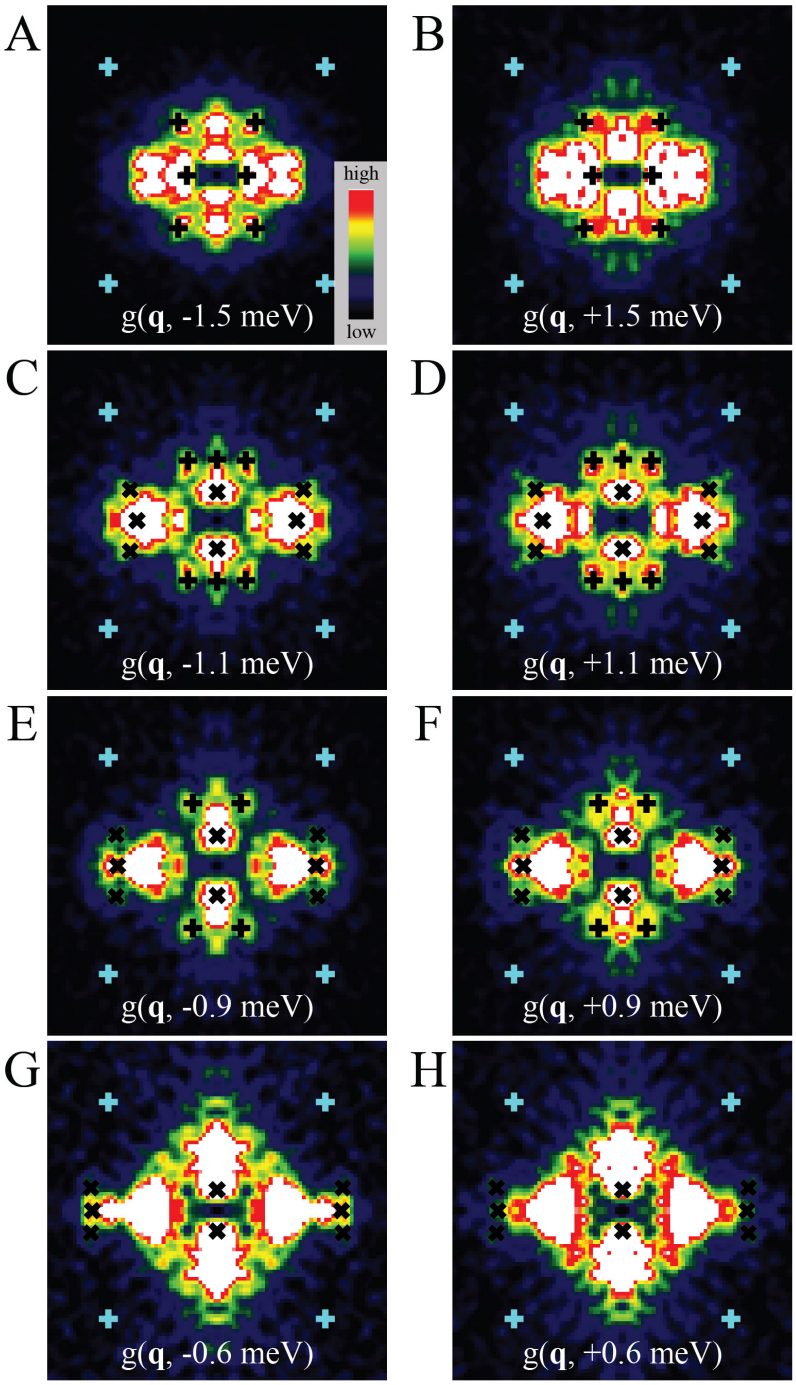

Figure 4.7: Particle-hole symmetry of BQPI. A-H, Symmetrized, averaged, and core subtracted amplitude Fourier transform $|g(\vec{q}, E)|$ in same field of view at $\pm E$ pairs. The tip here is simultaneously sensitive to Δ_α and Δ_ε. By tracking the black + and x indicators of the maximum $|g(\vec{q}, E)|$ for $q_2 = 2k_F$ one sees directly that the BQPI wavevectors q_2 for both Δ_α and Δ_ε diverge away from $q = 0$ as $E \to 0$.
Cyan crosses mark $(\pm\frac{2\pi}{8a_{Fe}}, \pm\frac{2\pi}{8b_{Fe}})$ positions.

CHAPTER 5

INTERPRETATION OF BOGOLIUBOV QUASIPARTICLE INTERFERENCE IN FeSe

In this chapter we present a comparison of Joint density of states (JDOS) simulations and measured BQPI data, before we summarize the energy evolution of extracted $\vec{q}$-vectors, and finally determine the Fermi surface and gap structure for the α- and ε-pocket from it. The last part of this chapter comprises of a comparison between BQPI measurements and various other techniques.

5.1 Joint density of states

In order to compare the observed BQPI to the proposed tight-binding (chapter 3) and pairing model (chapter 7), we simulate the BQPI using the joint density of states approach:

$$JDOS(\vec{q},\omega) = \int A(\vec{k}+\vec{q},\omega)A(\vec{k},\omega)d\vec{k}, \tag{5.1}$$

with the spectral function $A(\vec{k},\omega)$ given by $A(\vec{k},\omega) = -\frac{1}{\pi}Im\{\sum_a G_{aa}(\vec{k},\omega)\}$, where the sum runs over the orbitals a. Here $G_{aa}(\vec{k},\omega) = Z_a G^0_{aa}(\vec{k},\omega)$ is the dressed Greens function, and the Z-factors for the orbitals are the same as used for the calculation of the pairing interaction (see chapter 7 for more details), and given as $Z_a \in \{0.27152, 0.97172, 0.40482, 0.92362, 0.59162\}$. Varying quasiparticle weights for the individual d-orbitals are motivated by evidence for strong orbital selective correlations in chalcogenides both in experiment [39–41] and experiment [23, 37, 38, 58].

Furthermore, we separate the JDOS into partial JDOS simulations by restricting

the integration area to 1/4 of the Brillouin zone containing the corresponding pocket. Here to mimic the sensitivity of our tunneling tips to BQPI from different bands, we compute the partial JDOS for the α-pocket, for the ε-pocket, and the sum of both. This is a valid approach as the two pockets are well-separated in $\vec{k}$-space. The results in Fig. 5.1 are in excellent agreement with the banana tips model, as it clearly visualizes the three (independent) dominant scattering vectors $\{\vec{q_1}, \vec{q_2}, \vec{q_3}\}$ for each pocket, which are transformed into a set of eight through symmetry operations.

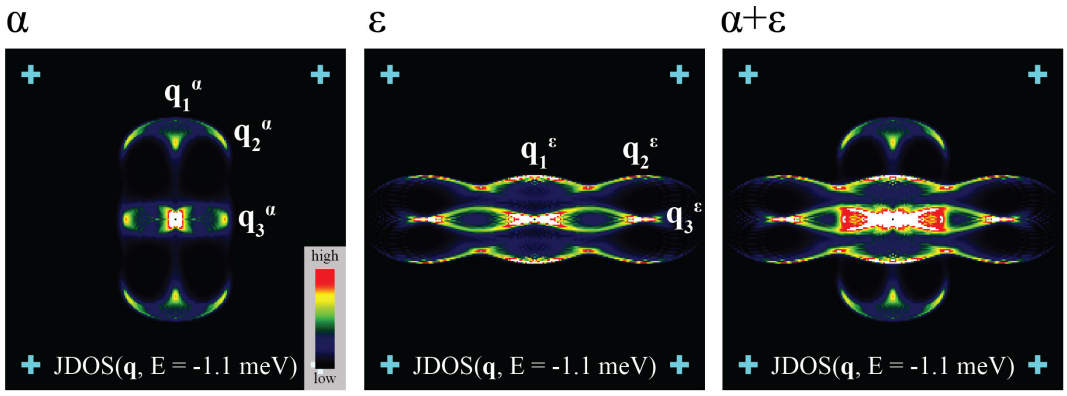

Figure 5.1: Partial Joint Density of States (JDOS) using the tight-binding model and orbital selective pairing for the α-pocket, the ε-pocket and the sum of both the α- and ε-pocket. Cyan crosses mark $(\pm\frac{2\pi}{8a_{Fe}}, \pm\frac{2\pi}{8b_{Fe}})$ positions.

Overall we find very good agreement between experiment and JDOS simulation, and deviations between the two can for example be ascribed to the static structure of the scatterers themselves which the JDOS simulation cannot take into account. We present typical measured BQPI data at four energies, and comparison to partial JDOS, for both the α- and ε-pocket in Fig. 5.2 and Fig. 5.3.

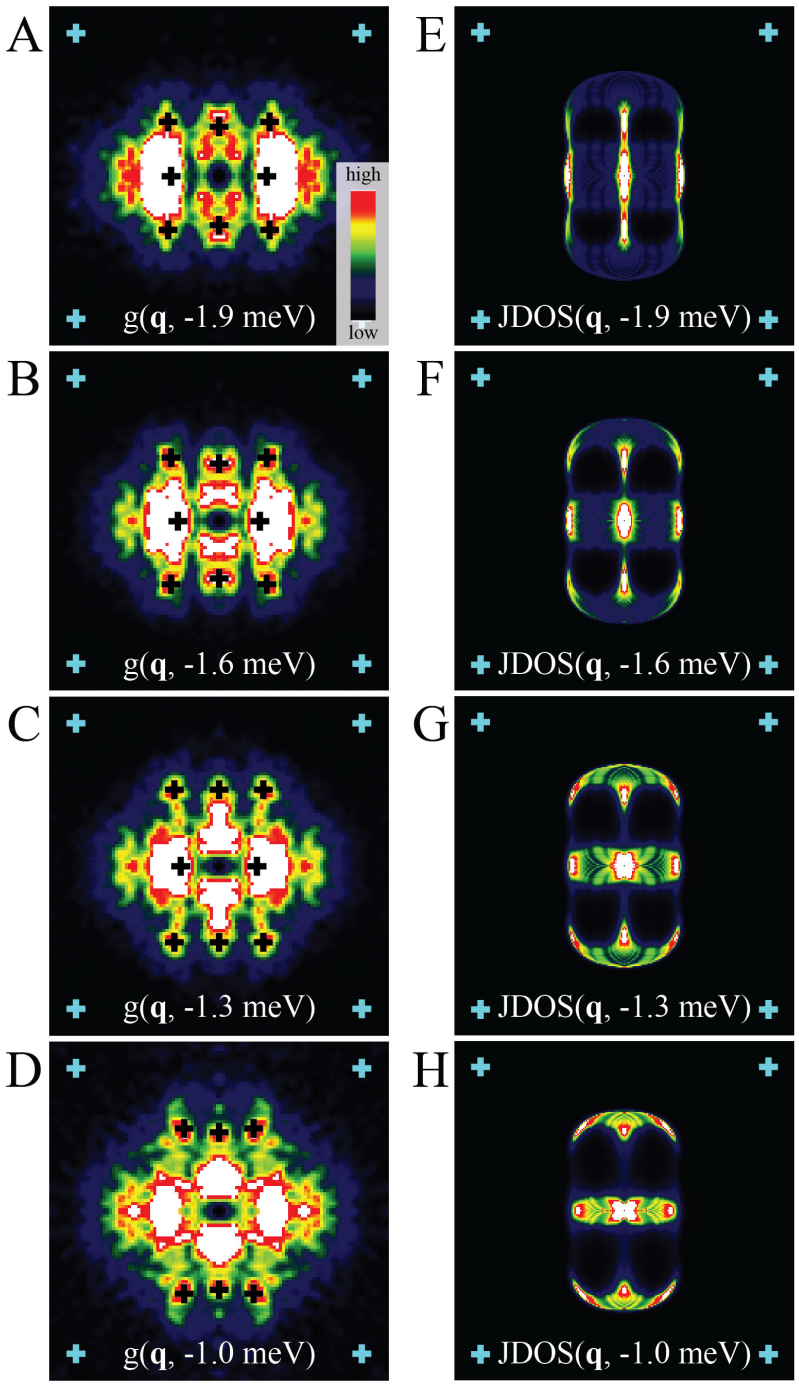

Figure 5.2: Comparison of $|g(\vec{q}, E)|$ and partial JDOS for an α-tip configuration. **A-D,** Symmetrized, averaged, and core subtracted amplitude Fourier transform $|g(\vec{q}, E)|$ at four energies inside the superconducting gap Δ_α. Black crosses mark the extracted q-vectors expected from the 'banana tips' model. **E-H,** Partial JDOS for α-pocket at corresponding energies.
Cyan crosses mark $(\pm\frac{2\pi}{8a_{Fe}}, \pm\frac{2\pi}{8b_{Fe}})$ positions.

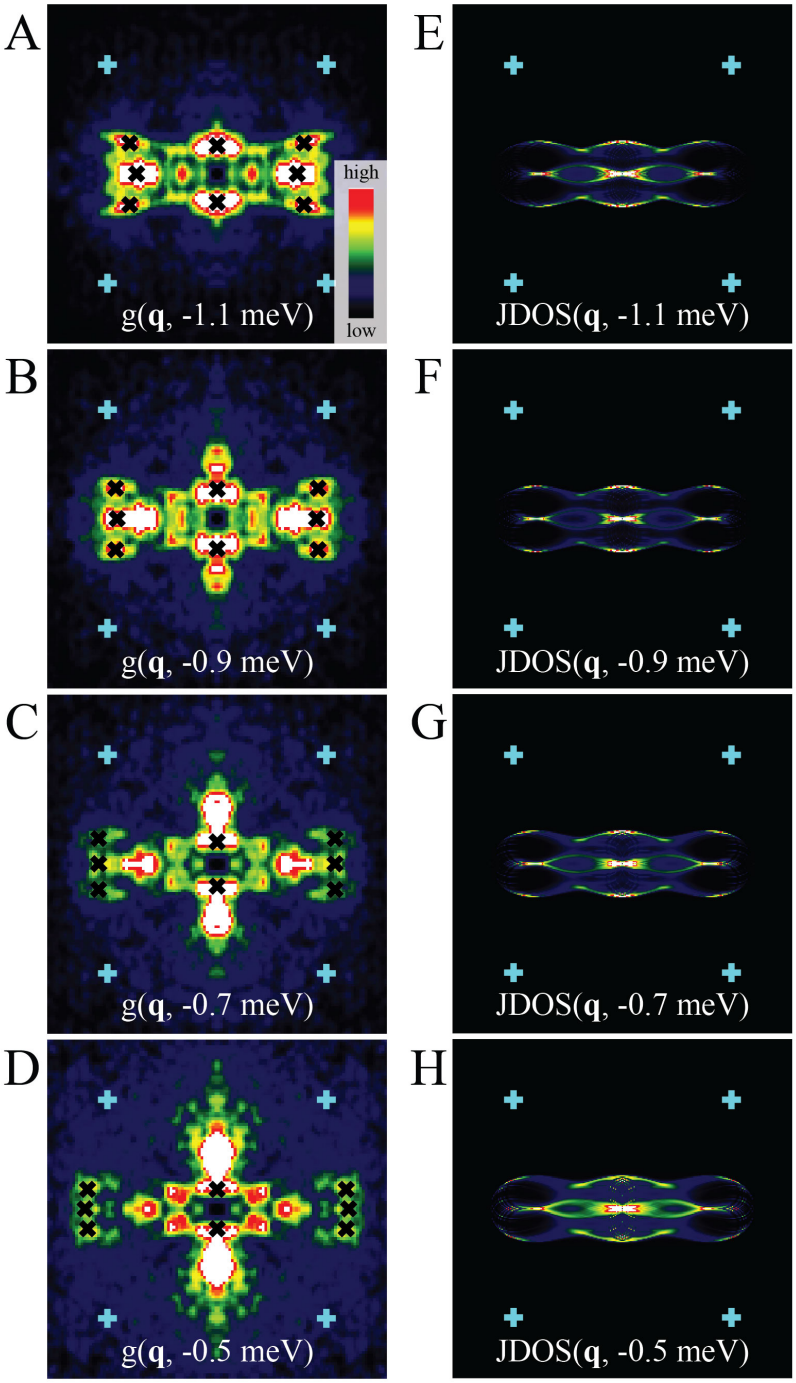

Figure 5.3: Comparison of $|g(\vec{q}, E)|$ and partial JDOS for an ε-tip configuration. **A-D,** Symmetrized, averaged, and core subtracted amplitude Fourier transform $|g(\vec{q}, E)|$ at four energies inside the superconducting gap Δ_ε. Black crosses mark the extracted q-vectors expected from the 'banana tips' model. **E-H,** Partial JDOS for ε-pocket at corresponding energies.
Cyan crosses mark $(\pm\frac{2\pi}{8a_{Fe}}, \pm\frac{2\pi}{8b_{Fe}})$ positions.

5.2 Fermi surface and gap structure from BQPI

The measured evolution of the BQPI wavevector triplet $\vec{q}_i^{\,\alpha}(E)$ for $2.3meV > |E| > 0.8meV$ (T=280mK) is plotted in Fig. 5.4A, while the measured wavevector triplet $\vec{q}_i^{\,\varepsilon}(E)$ for $1.3meV > |E| > 0.3meV$ (T=280mK) is shown in Fig. 5.4B. The resemblance to the expected energy evolution from the pedagogical model in Fig. 4.1 is immediately apparent. Figures 5.4C, D display the measured evolution of $|\vec{q}_i^{\alpha}(E)|$ and $|\vec{q}_i^{\varepsilon}(E)|$. Dashed lines symbolize the expected energy dependence of $|\vec{q}_i^{\alpha}(E)|$ and $|\vec{q}_i^{\varepsilon}(E)|$ in a 'banana tips' model for the empirically determined Fermi surfaces and $\Delta_\alpha(\vec{k})$ as well as $\Delta_\varepsilon(\vec{k})$. This serves as a consistency check for the extracted $\vec{q}$-values based on the geometric restrictions imposed on the wavevector triplets by eqs. 4.1 - 4.3 [115].

The associated density of states $N(E) \equiv dI/dV(E)$ spectrum measured at 280 mK is shown in Fig. 5.4E, and for comparison a model $N(E)$ in Fig. 5.4F. Black and red arrows mark coherence peaks that we associate with the maximum gap on the α- and ε-pocket, respectively. There is a small flat bottom part around the chemical potential which is consistent with nodeless superconductivity. A last prominent feature in the spectrum are the shoulders between ± 3 - 4 mV. They could be explained by coupling of a bosonic mode to the electronic spectrum [116, 117].

Finally, we note that, since both $\vec{q}_2^{\,\alpha}(E)$ and $\vec{q}_2^{\,\varepsilon}(E)$ evolve to finite wavevectors $2\vec{k}_F^{\,\alpha}$ and $2\vec{k}_F^{\,\varepsilon}$ respectively as $E \to 0$ (Figs. 5.4A-D), FeSe superconductivity is in the BCS limit and not approaching Bose- Einstein condensation where BQPI wavevectors must evolve to 0 as $E \to 0$.

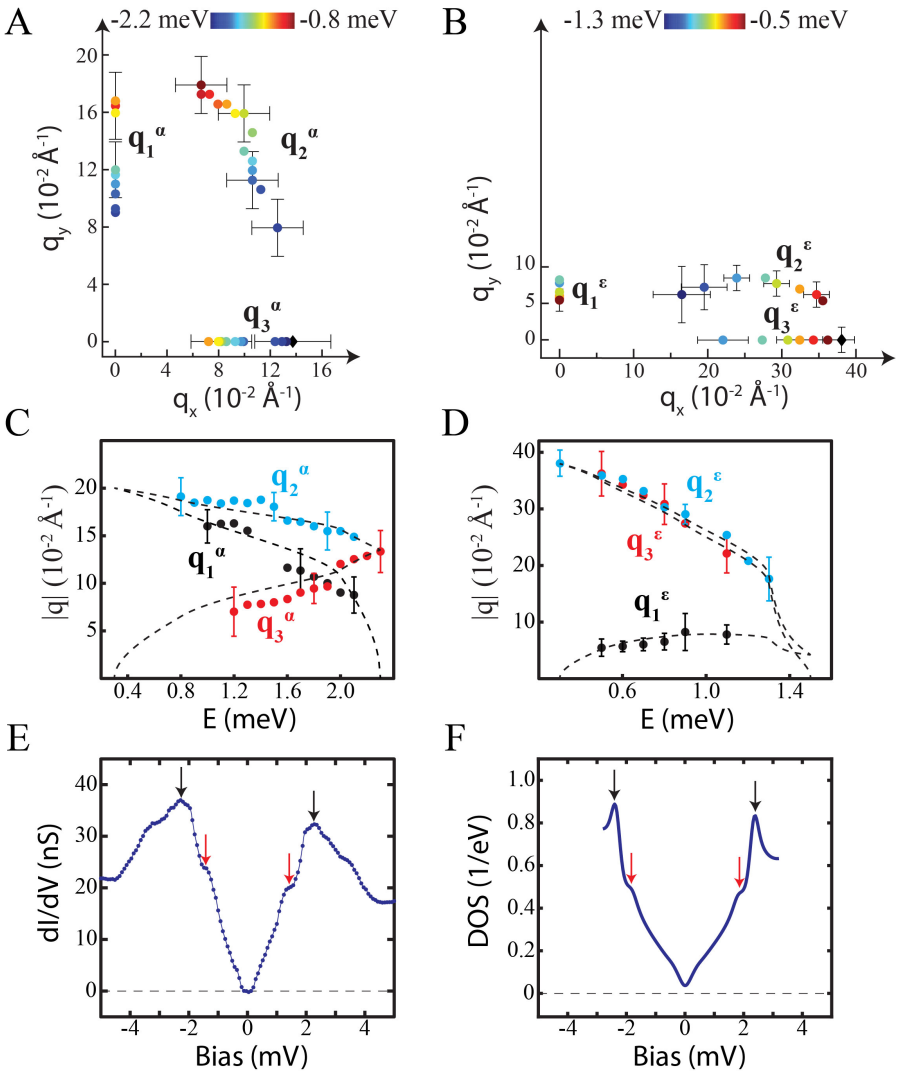

Figure 5.4: Summary of Bogoliubov quasiparticle interference results. A, Measured evolution of $\vec{q}_1^{\alpha}$, $\vec{q}_2^{\alpha}$, $\vec{q}_3^{\alpha}$. The black diamond is the first $\vec{q}_3^{\alpha} = -2.3meV$ data point. **B,** Measured evolution of $\vec{q}_1^{\varepsilon}$, $\vec{q}_2^{\varepsilon}$, $\vec{q}_3^{\varepsilon}$. The black diamond corresponds to the last $\vec{q}_2^{\varepsilon} = -0.3meV$ data point. **C,** Measured evolution of $|\vec{q}_i^{\alpha}(E)|$ for $2.3meV > |E| > 0.8meV$ at 280 mK. Dashed lines symbolize the expected energy dependence of $|\vec{q}_i^{\alpha}(E)|$ in a 'banana tips' model for empirically determined Fermi surface and $\Delta_{\alpha}(\vec{k})$. **D,** Measured evolution of $|\vec{q}_i^{\varepsilon}(E)|$ for $1.3meV > |E| > 0.3meV$ at 280 mK. Dashed lines symbolize the expected energy dependence of $|\vec{q}_i^{\varepsilon}(E)|$ in a 'banana tips' model for empirically determined Fermi surface and $\Delta_{\varepsilon}(\vec{k})$. **E,** Measured dI/dV(E); black arrows indicate the maximum energy gap on any band, which we determine from BQPI to be on the α-band. Red arrows indicate a smaller energy gap on a second band which from BQPI is assigned to the ε-band. **F,** Calculated N(E) using the band-structure and a gap structure model which will be discussed in chapter 7.

Next we use the measured BQPI wavevector sets $\vec{q}_i^{\alpha,\varepsilon}(E)$ shown in Figs. 5.4A, B, to determine the two Fermi surfaces by using eqs. 4.1 - 4.3 to find the $(k_x, k_y)_{\alpha,\varepsilon}$locations of all the banana tips for both the α- and ε-bands. These Fermi surfaces are shown in Figs. 5.5A, B. We use the same wavevector sets $\vec{q}_i^{\alpha,\varepsilon}(E)$ in conjunction with the two Fermi surfaces, to plot the energy $E = \Delta$ associated with the observation of BQPI for each Fermi surface wavevector $(k_x, k_y)_{\alpha,\varepsilon}$. The resulting functions are $\Delta_\alpha(\vec{k})$ and $\Delta_\varepsilon(\vec{k})$ (see chapter 2).

The area of the Fermi surfaces extracted by BQPI is consistent with that at $k_z = 0$ (see last section of this chapter). Next, the $N(E) \equiv dI/dV(E)$ density of states spectrum (T=280mK) shown in Fig. 5.4E is used to identify some additional key phenomena. First, the maximum gap on any band is $\Delta_\alpha^{max} = 2.3meV$ (black arrows) while another coherence peak occurs at the gap maximum of a second band at $\Delta_\varepsilon^{max} = 1.5meV$ (red arrows). Maximum gaps were assigned to bands based on the energy evolution of BQPI (Figs. 5.4A-D). And no conductance whatsoever is detected in the energy region $E \lesssim 150\mu eV$ meaning that $\Delta_{min} \gtrsim 150\mu eV$ for all bands. Finally, we plot schematically the measured magnitude of the energy gap $|\Delta_\alpha(\vec{k})|$ on the α-band in Fig. 5.5C, and the measured magnitude $|\Delta_\varepsilon(\vec{k})|$ on the ε-band in Fig. 5.5D, where in both cases we use the width of the shaded region to indicate $|\Delta(\vec{k})|$ and include values of extrema of any energy gap from $N(E)$ in Fig. 5.4E. From these measurements, we conclude that, although exhibiting extraordinarily anisotropic ($\Delta_\alpha^{max}/\Delta_\alpha^{min} \gtrsim 15$) C_2-symmetric energy-gap structures, FeSe remains a fully gapped or nodeless superconductor with gap minima $\Delta_{min} \gtrsim 150\mu eV$. Indeed, evidence for a nodeless gap structure for FeSe has been detected by a wide variety of different techniques [64–68]. As a last remark, we note that since our samples are not detwinned and our field of view limited to ~ 200 x 200 nm^2 we cannot exclude that the existence of nodes in

the gap structure is affected by long-range effects of twin boundaries [63, 65].

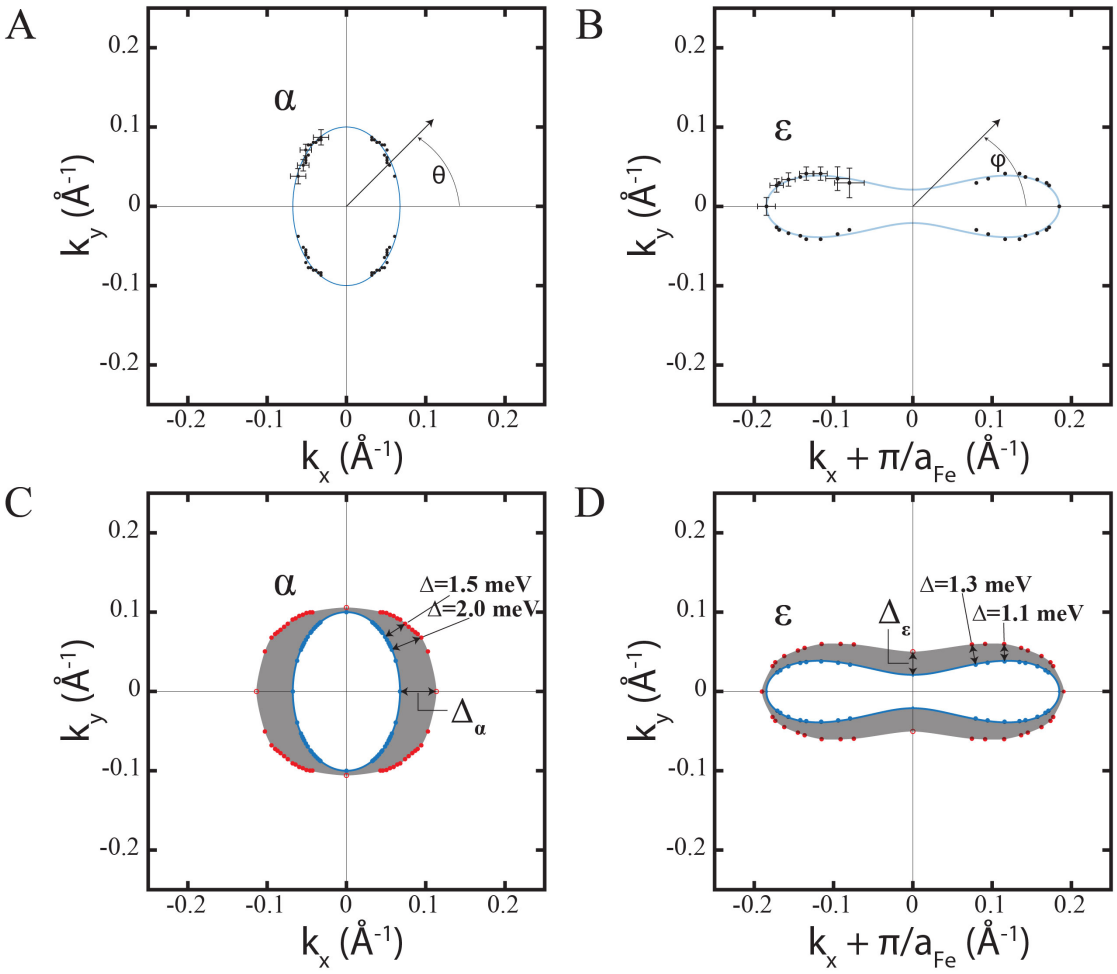

Figure 5.5: BQPI Determination of Fermi surfaces and energy gaps. A, Fermi surface of α-band measured using the BQPI triplet $\vec{q}_1^{\,\alpha}$, $\vec{q}_2^{\,\alpha}$, $\vec{q}_3^{\,\alpha}$. **B,** Fermi surface of ε-band measured using the BQPI triplet $\vec{q}_1^{\,\varepsilon}$, $\vec{q}_2^{\,\varepsilon}$, $\vec{q}_3^{\,\varepsilon}$. **C,** Energy-gap magnitude for the α-band measured using the energy dependence of the BQPI triplet $\vec{q}_1^{\,\alpha}$, $\vec{q}_2^{\,\alpha}$, $\vec{q}_3^{\,\alpha}$ plus the values of maximum and minimum energy gap from dI/dV(E) in Fig. 5.4E. **D,** Energy-gap magnitude for the ε-band measured using the energy dependence of the BQPI triplet $\vec{q}_1^{\,\varepsilon}$, $\vec{q}_2^{\,\varepsilon}$, $\vec{q}_3^{\,\varepsilon}$ plus the values of maximum and minimum energy gap from dI/dV(E) in Fig. 5.4E.

5.3 Comparison of SI-STM results to other experiments

Figure 5.6 shows directly the agreement of our model band structure to the position of the Fermi surface that we measure using BQPI (red dots). The black line is the calculated tight-binding model Fermi surface at $k_z = 0$ from our band-structure, and agrees well with the measured positions within the experimental error bars. At the same time, the dispersion of our band-structure along k_z is significant and agrees well with the findings from a recent ARPES investigation [56]. In Fig. 5.6, we also reproduce the spectral function measured by ARPES [55] at $k_z = \pi$, and it compares very well to the model Fermi surface at $k_z = \pi$ (blue line). The superposition of copies of the basic Fermi surface spectral-function features but rotated by $\pi/2$, is due to the existence of both orthorhombic domains in the ARPES study; obviously our band structure model does not reproduce these effects as discussed in detail in chapter 3.

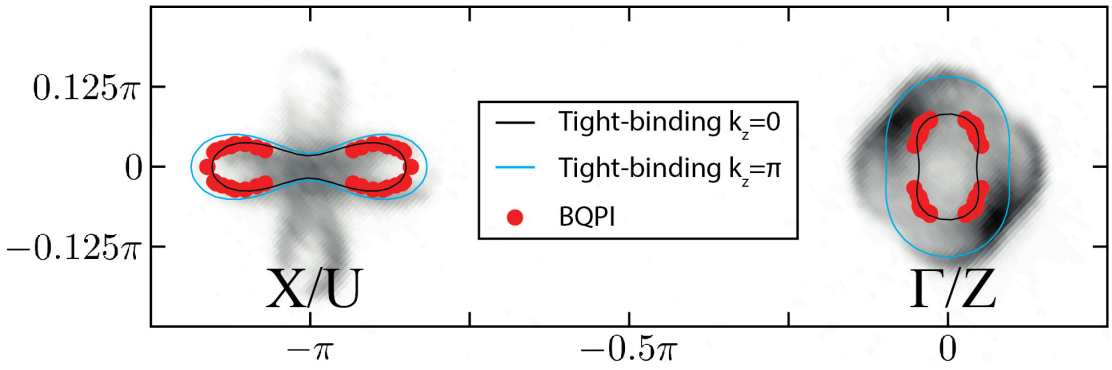

Figure 5.6: Overlay of BQPI results and ARPES spectral function. Comparison between the Fermi surface of our model at $k_z = 0$ (black lines) and $k_z = \pi$ (blue lines) and experimentally deduced points of the Fermi surface from BQPI (red dots) and a map of the spectral function at $\omega = 0$ and $k_z = \pi$ as measured by ARPES (gray map) [55]. The features in the ARPES spectral function that generate an apparent C_4-symmetry about both the Γ-point and about the X-point, are due to summation over the two types of orthorhombic domains that are orthogonal to each other, and are irrelevant for band structure parameterization.

Note that the same experimental work also revealed the Fermi surface at $k_z = 0$

which gives very similar spectral positions as the ones obtained from BQPI. Therefore, we concentrate on the use of the model system for $k_z = 0$ whenever carrying out simulations for comparison with the data as for example the JDOS simulations at the beginning of this chapter.

For the calculation of the extremal Fermi surface areas we use the 10-band analog of our band structure [27] that additionally introduces small hybridizations on the electron pockets yielding an orbit of the inner electron pocket and the outer electron pocket. The extremal areas obtained within this method would give rise to quantum oscillation frequencies of: 66T (inner electron pocket), 199 T (hole pocket at $k_z = 0$), 579T (outer electron pocket), and 651 T (hole pocket at $k_z = \pi$); results were rounded to last digit. The measured extremal frequencies for magnetic field angle $\theta = 0$ are reported as values in the range of 60 T - 114 T, 200 T - 207 T, 530 T - 580 T, and 660 T - 680 T, see table I in Ref. [56], and references therein. Thus, there is good comprehensive agreement within the experimental uncertainties between the band structure described by our model of the electronic structure and the quantum oscillation data.

Concerning the superconducting gap structure we determined using BQPI imaging. A recent specific heat experiment finds excellent agreement using our reported gap structure [43]. This is important as specific heat probes the bulk properties while STM and ARPES are surface sensitive probes, and the less two-dimensional nature of the iron-based superconductors compared to the cuprates necessitates more detailed comparisons of bulk and surface sensitive probes.

CHAPTER 6

DETERMINING THE RELATIVE SIGN OF THE SUPERCONDUCTING GAPS IN FeSe

The relative sign of $\Delta_\alpha(\vec{k})$ and $\Delta_\varepsilon(\vec{k})$ then remains to be determined. This is critical because one of the key characteristics of iron-based superconductors is whether the energy gaps on different bands have opposite signs, see introduction and Refs. [16, 17], for example. For FeSe this situation should be designated +− because the more conventional designation s_{+-} [16, 17] is rendered inappropriate by orthorhombic crystal/band-structure symmetry. One inventive technique for measuring +− pairing symmetry is to detect the enhancement in amplitude of $g(\vec{q}, E)$ at specific BQPI wavevectors when a magnetic field is applied; this was proposed to occur because field-induced magnetism results in amplified scattering interference between regions of $\vec{k}$-space with same-sign energy gaps [118]. Although never used for FeSe studies, in Fe(Se,Te) this approach has yielded field-induced reduction for wavevectors linking the electron and hole pockets, indicative of +− pairing symmetry [97]. Yet, there are reservations about this interpretation [98–100] because: (i) a subset of wavevectors where the Fe(Se,Te) field-induced alternations are reported occur at Bragg points of the reciprocal lattice and, (ii) a microscopic explanation for the field-induced reductions is absent.

Instead we implement the phase-sensitive BQPI scattering technique [100] in FeSe which relies on the coherence factor for scattering between superconducting gaps as introduced in chapter 2. This is to our knowledge the very first time this technique has been applied to any superconducting material.

6.1 Sign-changing or sign-preserving superconductivity?

For FeSe, the relevant interband scattering wavevector $\vec{p}_1$ is shown in Figs. 6.1A-C both for the ++ and +− scenario. Given our quantitative knowledge of the Fermi surface and energy gaps of FeSe (Fig. 5.5), $\rho_-(\vec{q}, E)$ can numerically be predicted specifically for this material.

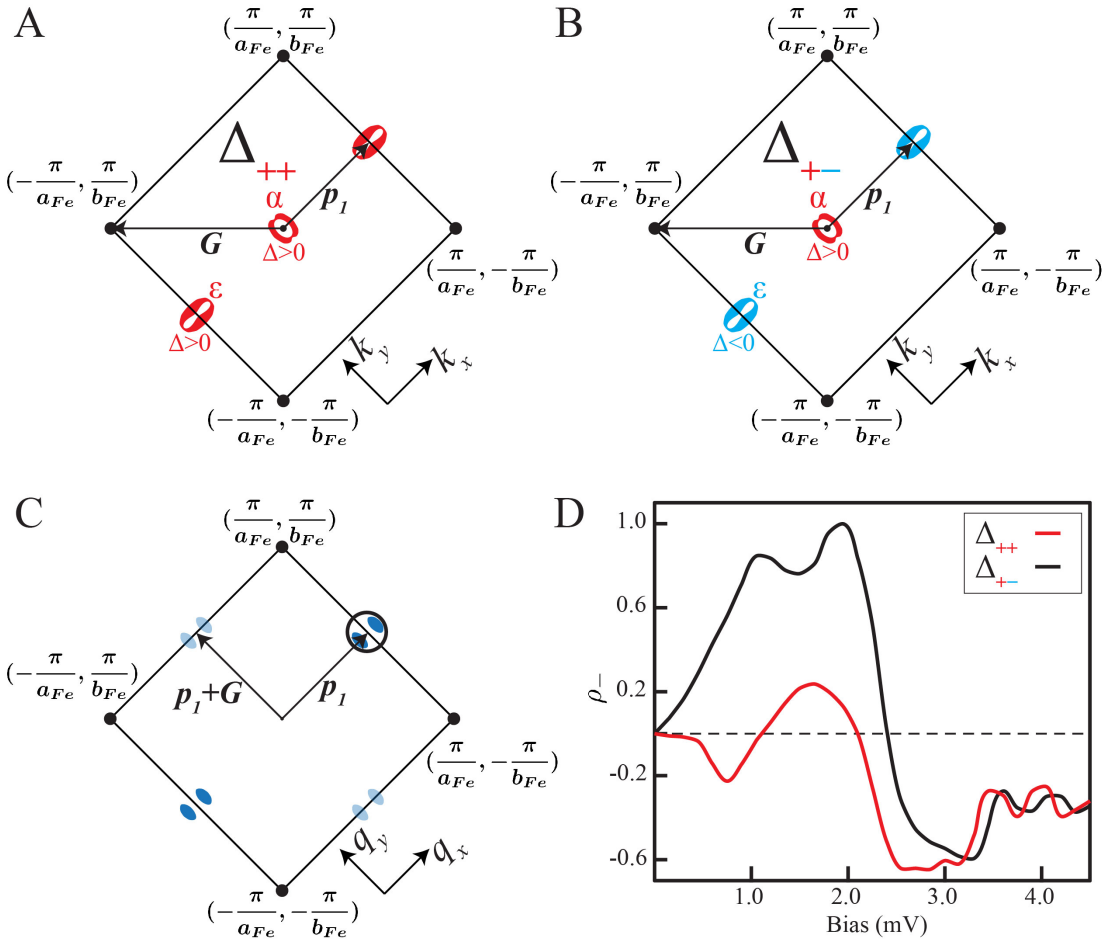

Figure 6.1: Interband scattering in FeSe. **A,** Schematic visualization of FeSe interband scattering wavevector $\vec{p}_1$ between α- and ε-bands in $\vec{k}$-space for sign-preserving order parameter. **B,** Schematic visualization of FeSe interband scattering wavevector $\vec{p}_1$ between α- and ε-bands in $\vec{k}$-space for sign-changing order parameter. **C,** FeSe $\vec{q}$-space of scattering wavevectors. **D,** Predicted $\rho_-(E)$ for ± pairing symmetry using the band/gap structure of FeSe, shown as solid black curve. Predicted $\rho_-(E)$ for no gap sign change in FeSe shown as solid red curve.

Following Ref. [100], we perform a calculation of the BQPI response within the T-matrix approach. For this purpose, the Nambu Hamiltonian $H = \begin{pmatrix} H_N & \Delta \\ \Delta^T & -H_N^T \end{pmatrix}$ as a matrix in orbital space is set up where the Hamiltonian is given in chapter 3. The superconducting gap is taken from a self-consistent calculation, [119,120] using the same band structure and pairing model as outlined in chapters 3 and 7.

Next, a weak (attractive) nonmagnetic impurity is modeled as a potential scatterer on a single Fe position, motivated by the Fe centered defects seen in the present STM experiment and also by other groups [63, 88]. These defects are also observed in the monolayer FeSe [121]. Setting $H_{imp} = V_0\delta_{ab}$ as a constant on-site scatterer at position $\mathbf{r}^*$ in orbital space, we use the additional impurity term in the Hamiltonian $H_{imp} = V_0 \sum_a c^\dagger_{a,\mathbf{r}^*} c_{a,\mathbf{r}^*}$ which describes the scattering from an impurity centered at a Fe lattice position in the approximation of a short-range potential.

Then we solve the T-matrix using the local Greens function $G_0(\omega) = \sum_{\mathbf{k}} G^0_{\mathbf{k}}$ where $G^0_{\mathbf{k}} = (\omega + i0^+ - H_{\mathbf{k}})^{-1}$. Noting that the impurity potential is constant in momentum space, we obtain the Greens function in the presence of scatterer as $G_{\mathbf{k},\mathbf{k}'}(\omega) = G^0_{\mathbf{k}-\mathbf{k}'}(\omega) + G^0_{\mathbf{k}}(\omega)T(\omega)G^0_{\mathbf{k}'}(\omega)$. The T-matrix is obtained from the equation $T(\omega) = [1 - V_{imp}G_0(\omega)]^{-1}V_{imp}$ such that the change in the local density of states is given by $\delta N(\mathbf{q},\omega) = \frac{1}{\pi} Tr\{Im \sum_{\mathbf{k}} G^0_{\mathbf{k}}(\omega)T(\omega)G^0_{\mathbf{k}+\mathbf{q}}(\omega)\}$.

Theoretically, the quasiparticle scattering between states with sign-changing order parameter yields a characteristic resonant energy dependence in $\rho_-(\omega)$, the anti-symmetrized QPI response, integrated over a finite momentum space corresponding to relevant inter-band scattering processes as discussed in Ref. [100]. To pick out only the inter-band scattering contributions in FeSe which are sign-changing in the Δ_{+-} scenario, we integrate over an area in momentum space

centered at $(\pi, 0)$ to obtain $\rho(\omega) = \sum_{\mathbf{q}}' \delta N(\mathbf{q}, \omega)$ and construct $\rho_-(\omega) = \rho(\omega) - \rho(-\omega)$. These calculations are done for two different gap structures that yield the same density of states because they differ only by a relative sign between the order parameters on the electron band and the hole band (Figs. 6.1A, B).

The results for the calculations are presented in Fig. 6.1D. The quantity $\rho_-(\omega)$ crosses zero at an energy within the superconducting gap for the sign-preserving order parameter Δ_{++} (solid red curve in panel D). For the sign-changing order parameter Δ_{+-}, there is however no zero crossing in $\rho_-(\omega)$ up to roughly the maximum superconducting gap (solid black curve in panel D).

6.2 Point defects in FeSe

Before we demonstrate how the experimental equivalent of Fig. 6.1D is created, we discuss the prominent type of defect found in FeSe [63, 88, 121]. Initially, it was thought that the defect is either created through substitution of an Fe-atom by a Se-atom or that it is a vacancy in the Fe-lattice [88]. A recent, detailed analysis of the same type of defect in the monolayer FeSe shows that the vacancy produces the best agreement between measured and simulated LDOS [121]. Due to its apparent shape in STM measurements it is called a dumbbell defect [88, 89, 121].

Below we show spectroscopic measurements for the dumbbell defect by Kasahara et al. [62] and us (Fig. 6.2). The key feature is a very strong resonance at $\sim$ 10 mV which is observed in both experiments. A broader peak around $\sim$ -20 mV exists simultaneously, as indicated by the slow rise in the spectra between -20 and -15 mV. Finally, we remark that differences in the visual appearance of the dumbbell defect between different topographic measurements are merely

due to the different bias voltages used to form topographic images (compare for example positive bias used in Fig. 6.2 to negative bias used in Fig. 2.4).

Fig. S6 in Kasahara et al., PNAS Vol. 111, No. 46, 16309-16313, November 18, 2014

Spectra taken at 0.4 K, Setup for topography V_s=+95 mV, I_s=100 pA

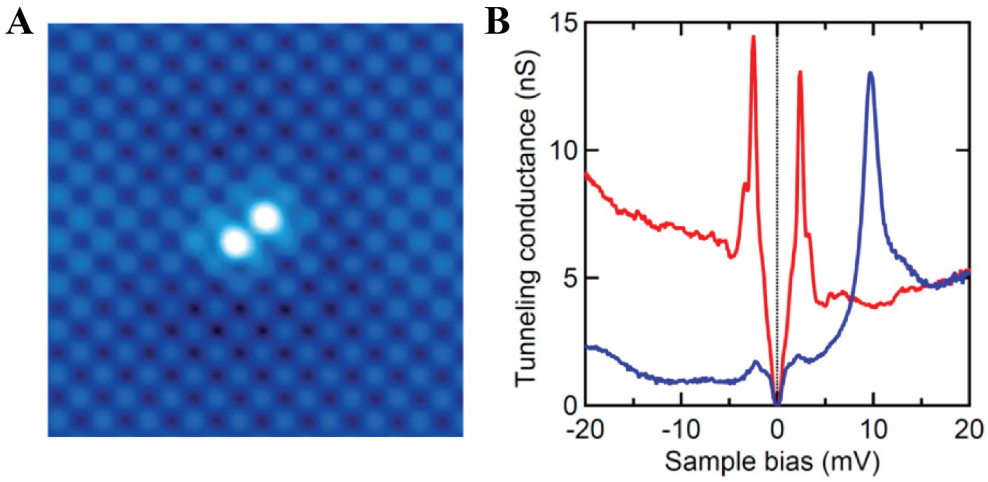

Our measurement:

Spectra taken at 4.2 K, Setup for topography V_s=+50 mV, I_s=10 pA

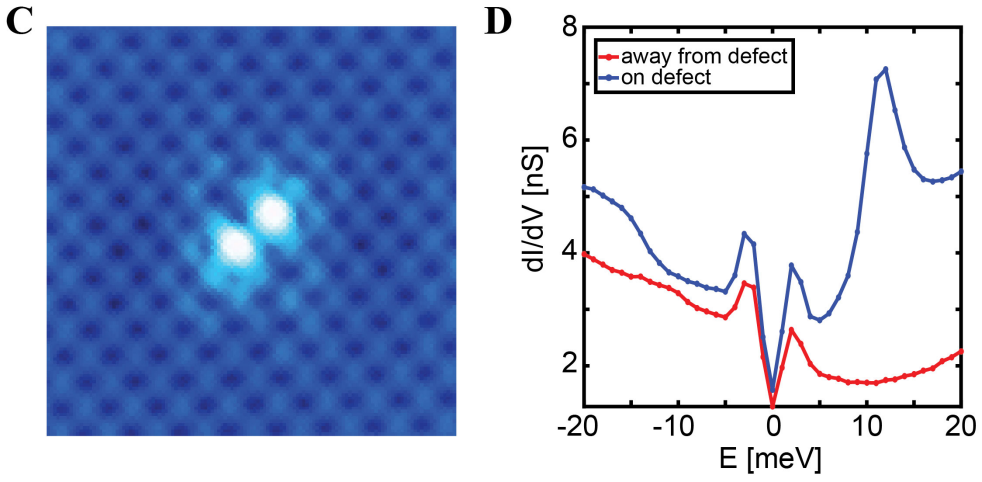

Figure 6.2: Dumbbell impurity in FeSe. **A,C,** Comparison of topographic images of the impurity in Kasahara et al. and in our studies. **B,D,** show the comparison of dI/dV spectra at the center and away from this impurity site. Different junction conditions (normalizations) were used for the curves in the two panels, but their overall characteristics, comparing off-impurity (red) curve shapes and on-impurity (blue) curve shapes to each other, are alike.
A, B were reproduced from reference [62].

Spectroscopic measurements of the dumbbell defect that focus on the superconducting energy gap find in-gap states at the position of the defect. We analyze the single defect by taking dI/dV line-cuts through it along the Fe-lattice x- and y-direction. Figure 6.3 presents dI/dV line-cuts through the single defect. The differential conductance inside the superconducting gap exhibits an increase at the defect location. The effect is small, but clearly visible.

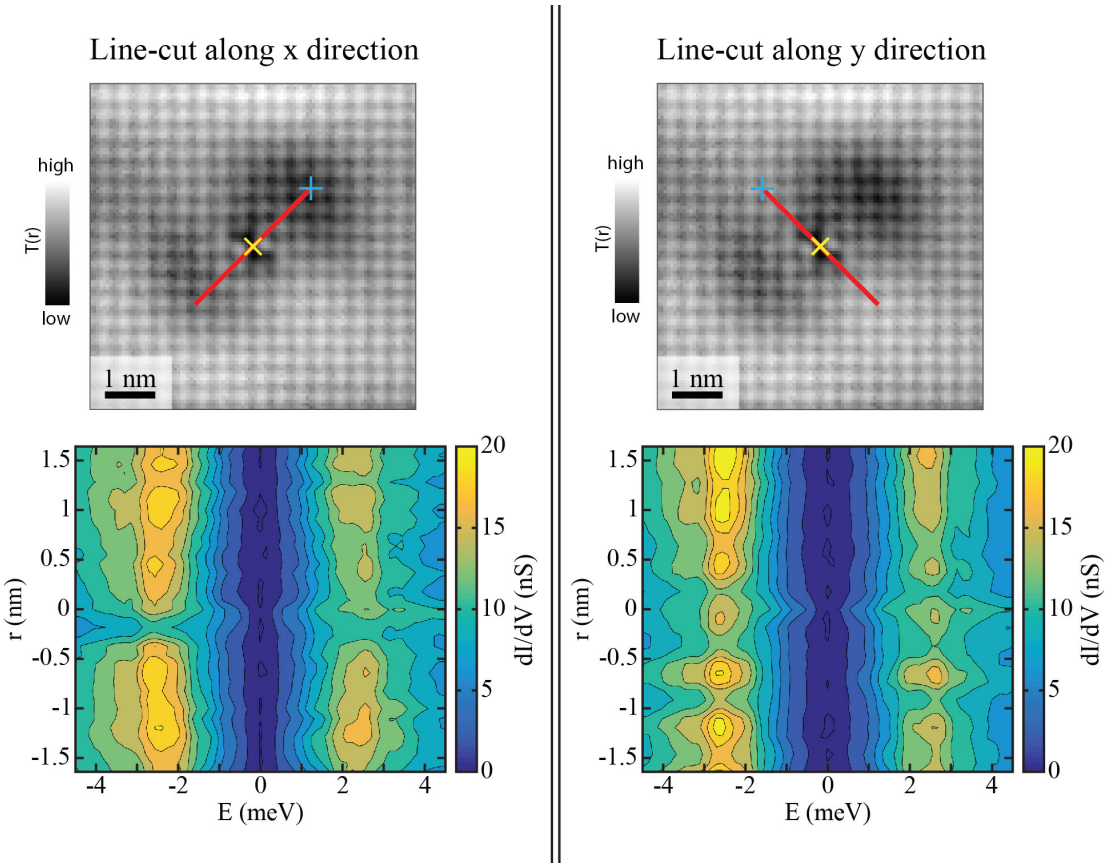

Figure 6.3: In-gap states induced by impurity. dI/dV line-cuts through the single impurity site along the x- and y-direction where x is parallel to a_{Fe} and y is parallel to b_{Fe}. While small, an increase of the dI/dV is clearly visible inside the superconducting gap at the location of the impurity (corresponding to 0 nm in the dI/dV panels) that is indicative of a weak in-gap impurity state.

Lastly, we compare the dumbbell defect to what based on its appearance in topography is either a vacancy in the Se-lattice or a substitution of a Se-atom by an impurity atom, see Fig. 6.4. The most notable difference between a defect in

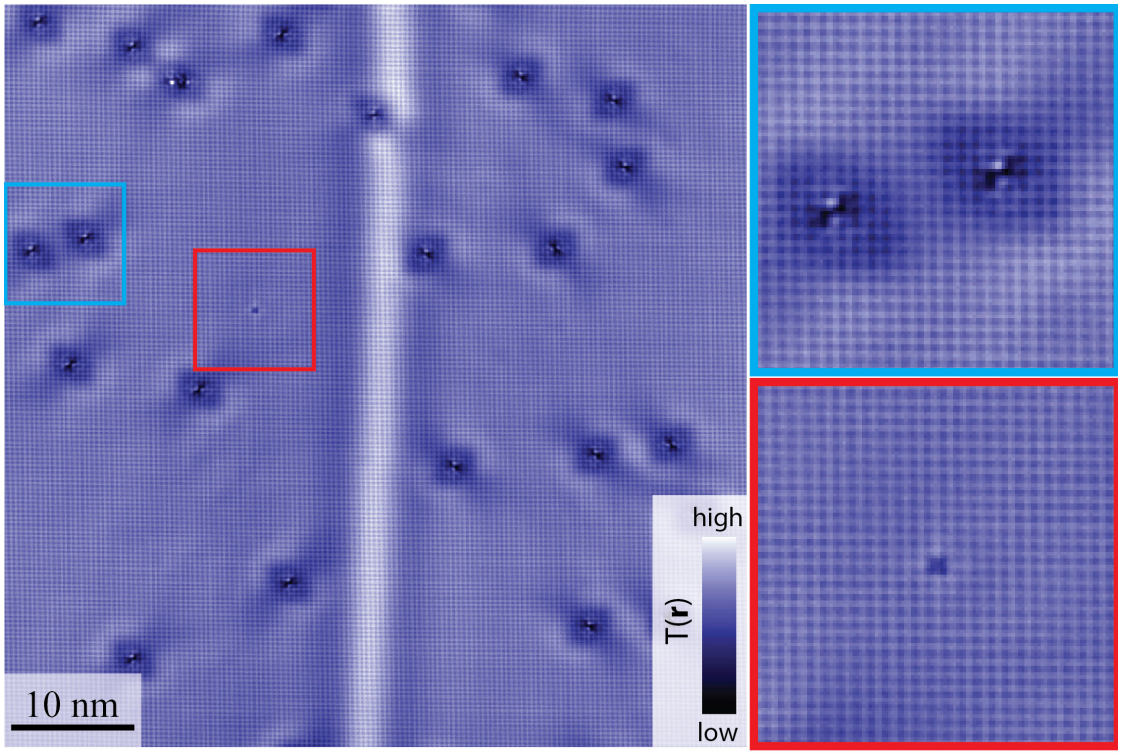

Figure 6.4: Dumbbell defect compared to Se-lattice defect. Constant current topography showing several dumbbell defects in two orthorhombic domains, and a Se-lattice defect. While the Friedel oscillations are very strong around the dumbbell defects there is virtually no response around the Se-lattice defect.

the Fe-lattice and a defect in the Se-lattice is the extreme disparity in terms of the observed Friedel oscillations or their lack thereof in the case of the Se-lattice defect (magnified regions in Fig. 6.4). As we require BQPI scattering for phase sensitive measurements of the gap sign [100], we focus on the dumbbell defects in the following.

6.3 Phase resolved FT-STM of single defects in FeSe

Experimentally, the challenge is then to achieve phase-resolved imaging of BQPI surrounding a single impurity atom in FeSe. We extract $\rho_{-}(\omega)$ from the experi-

ment by taking advantage of the fact that the differential tunneling conductance $g(\vec{r},\omega)$ is proportional to the local density of states of the sample $\rho(\vec{r},\omega)$. Next we construct in Fourier space the real part of the anti-symmetrized differential tunneling conductance $\rho_{-}(\vec{q},\omega) = Re\{g(\vec{q},+\omega)\} - Re\{g(\vec{q},-\omega)\}$ and integrate in a circular region around $(\pi,0)$-scattering which connects the electron and hole pocket at X and Γ, respectively: $\rho_{-}(\omega) = \sum_{(q_x-p_{1,x})^2+(q_y-p_{1,y})^2\leq\delta q^2} \rho_{-}(\vec{q},\omega)$. Here $\vec{p_1} = (p_{1,x}, p_{1,y})$ corresponds to the position of $(\pi/a_{Fe},0)$-scattering in $\vec{q}$-space, and the radius used for integration δq is chosen so that we capture only intensity related to scattering between the electron and hole pocket at X and Γ. δq is thus determined by the size of the two pockets.

However, before one computes $\rho_{-}(\omega)$, any shift of the scatterer away from the origin of the Fourier transform (FT) needs to be corrected as exactly as possible. The correction is necessary as any shift of the scatterer, i.e. the impurity, in real space away from the origin of the FT creates an additional phase term in $\vec{q}$-space according to the shift theorem of FTs: $FT\{f(\vec{r}-\vec{r_0})\} = e^{-i\vec{q}\vec{r_0}} FT\{f(\vec{r})\}$. Fortunately, the shift theorem allows one to correct the data. The experimental challenge lies therefore in determining the spatial position of the scatterer with high precision.

As mentioned above, the dominant type of defect in FeSe is centered on an Fe-atom. We know the relative position of Se- and Fe-atoms from the crystal structure. FeSe cleaves between two layers of selenium so that it is a reasonable assumption that STM images the Se-atoms. Before we determine the spatial shift of the impurity we correct the data for distortions due to non-orthogonality in the x/y axes of the piezoelectric scanner tube using the Lawler-Fujita algorithm [94]. After that we shift the data to the pixel corresponding to the origin of the FT.

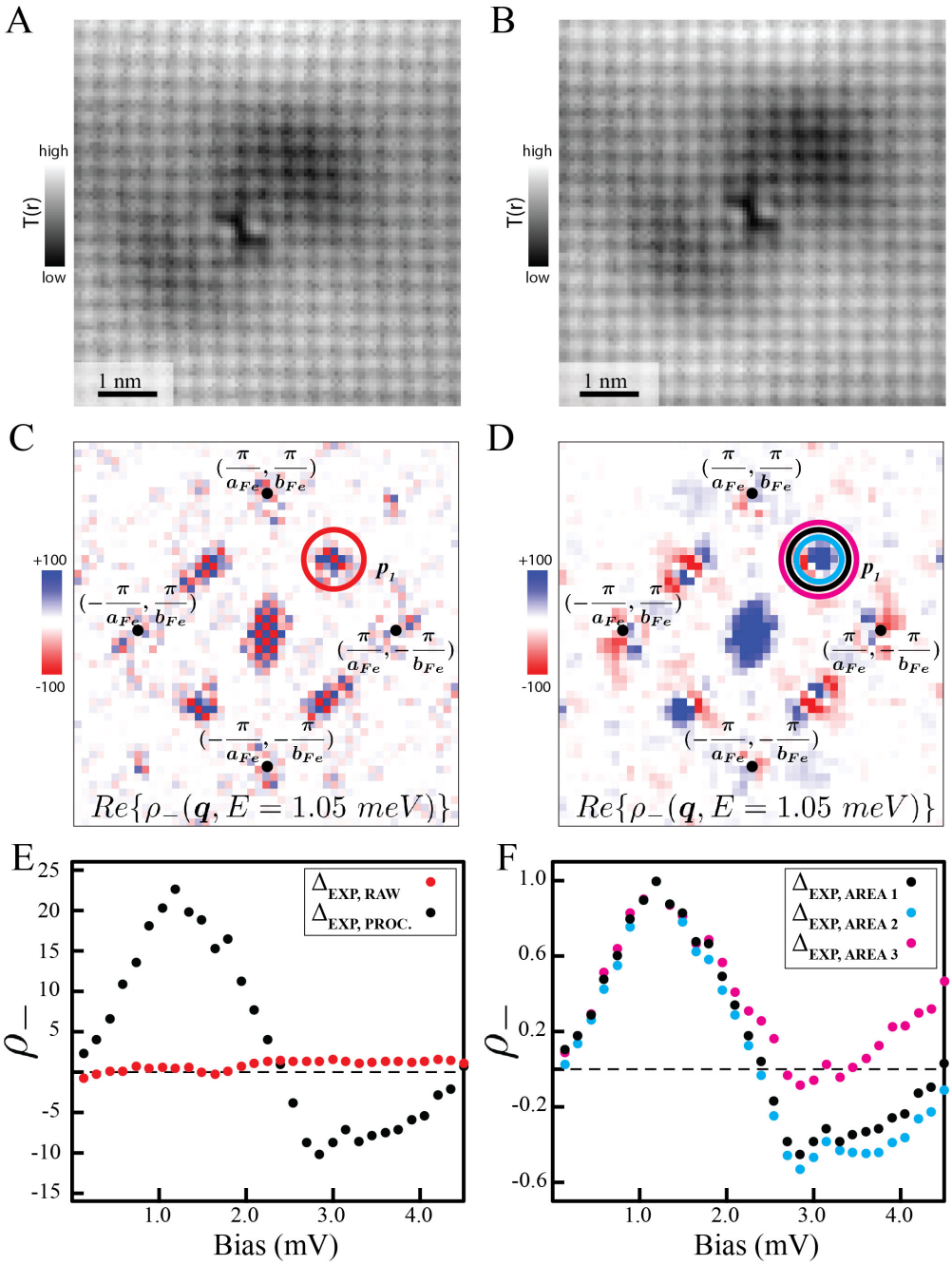

Figure 6.5: Experimentally extracted $\rho_-(\omega)$. A, Constant current topography of a single defect in FeSe. **B,** Constant current topography of the same defect as in A, but the data has both been LF-corrected and shifted so that the center of the defect is at the origin of the FT. **C,** $Re\{\rho_-(\vec{q}, \omega = 1.05meV)\}$ of the raw data. **D,** $Re\{\rho_-(\vec{q}, \omega = 1.05meV)\}$ of the LF- and shift-corrected data. **E** Comparison of $\rho_-(\omega)$ for both the raw and LF- and shift-corrected data. **F,** Comparison of $\rho_-(\omega)$ for three differently sized integration areas in $\vec{q}$-space.

The measured $\rho_-(\omega)$ is shown in Fig. 6.5. To increase the signal-to-noise ratio we average over adjacent energy values of $\rho_-(\omega)$. Note that the small Fermi surface pockets clearly separate scattering between states from and to different pockets, e.g. there are no intraband scattering events at the relative energy scale that are picked up by the integral. Resolving the structure of the tiny Fermi surface pockets is an experimental challenge because large FOV are required in STM, but at the same time it allows one to clearly separate intraband contributions.

In order to test how robust the result is under change of the integration area, we used three circular areas as depicted in Fig. 6.5D. The radius for the smallest, blue circle was three quarter the size of the medium black circle, and the radius of the biggest, magenta circle was five quarters the size of the medium black circle. As can be seen in panel F, the results are very consistent, and the biggest change occurs for energies outside the superconducting gap. For clarity and easier comparability $\rho_-(\omega)$ has been normalized to its maximum value for all three cases.

In order to confirm that the $\rho_-(\vec{q},\omega)$-signal originates from scattering inside the superconducting state, and is not for example due to effects of the band structure or the defect itself we analyze a defect at $T = 4.2K < T_C$ and $T = 10.0K > T_C$. Setup voltage ($V_s = -50mV$), tunneling current ($I = 500pA$), and modulation voltage for the lock-in measurement ($V_M = 1mV$) were identical in both measurements. As shown in Figs. 6.6A-D the signal related to scattering between the α- and ε-pocket vanishes above T_C. At the same time no sign of the superconducting gap remains visible in spectroscopy above T_C, see Fig. 6.6E. From that we conclude that the majority of the $\rho_-(\vec{q},\omega)$-signal stems from the properties of the superconducting ordered state in FeSe.

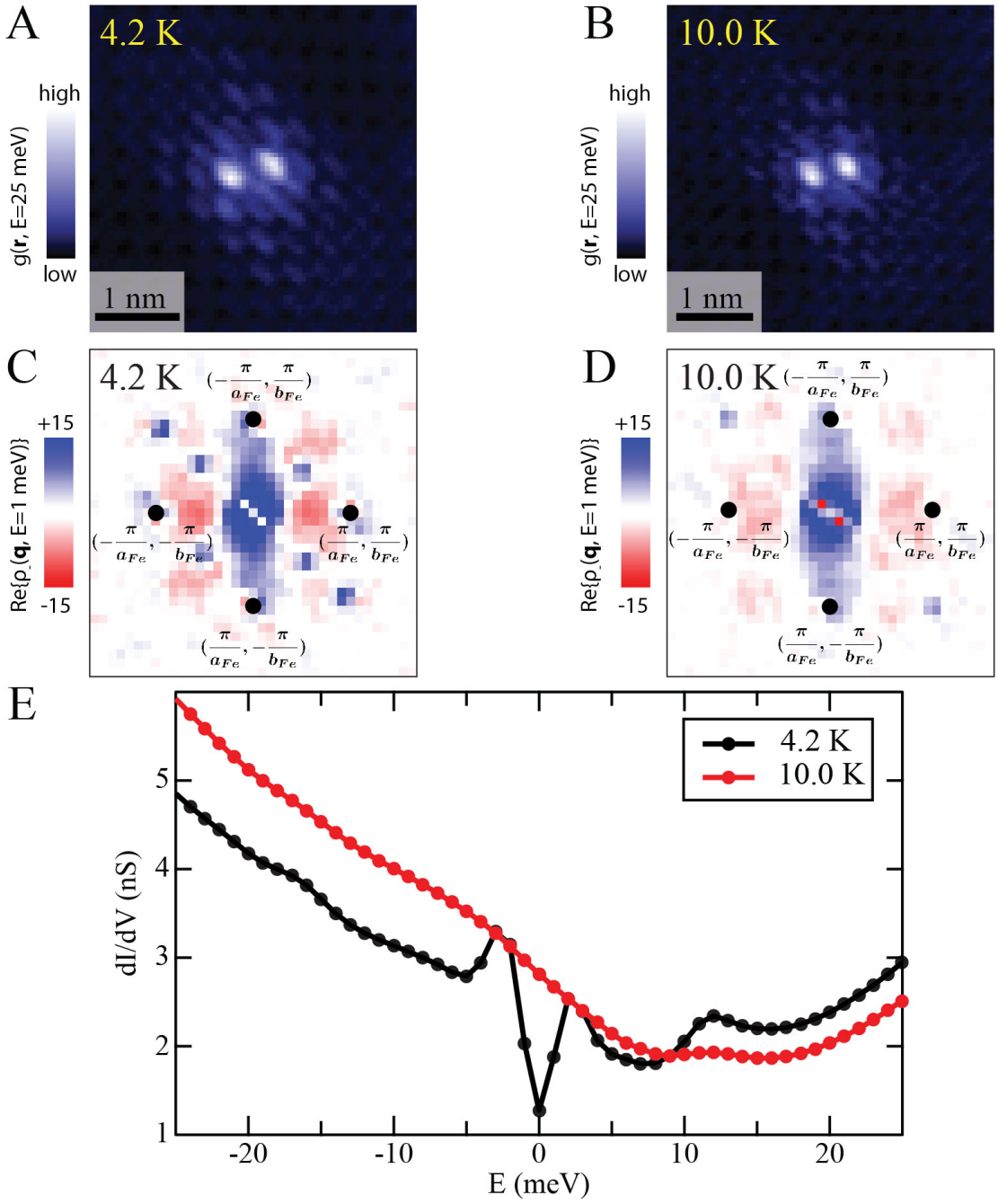

Figure 6.6: Disappearance of $\rho_-(\vec{q},\omega)$-signal above T_C. **A,B,** Differential conductance image at 25 meV of the same impurity at 4.2 K and 10.0 K. **C,D,** $Re\{\rho_-(\vec{q},\omega = 1meV)\}$ for the defect shown in A and B. The signal corresponding to scattering between the α- and ε-pocket vanishes above T_C. **E,** Average spectrum for the field of view shown in A, B recorded for the same setup voltage and current. Above T_C no sign of the superconducting gap remains.

6.4 Sign-changing superconductivity in FeSe

We present a comparison of this measured $\rho_-(E)$ to its predicted form for the FeSe gaps $\Delta_\alpha(\vec{k})$, $\Delta_\varepsilon(\vec{k})$ with Δ_{+-} and Δ_{++} symmetry in Fig. 6.7. Panel A depicts the LF- and shift corrected constant current topograph, and panel B contains the differential tunneling conductance at 1.05 meV in the same field of view. The conductance has been LF- and shift corrected using identical parameters as for the topograph. Distinguishing the high frequency oscillations corresponding to interband scattering in real space is complicated due to the coexisting atomic contrast. Fourier transform vastly simplifies the situation in this scenario. In both A and B red x-markers for Se and yellow +-markers for the Fe have been added in the lower right corner.

In Fig. 6.7C we repeat the expected Δ_{+-} pairing scenario for FeSe, and panel D shows the experimentally extracted and theoretically predicted $\rho_-(E)$-curves. Agreement is far better for the Δ_{+-} case. We reemphasize that the relevant difference between Δ_{+-} and Δ_{++} is the existence of a zero crossing for the latter. Thus, within the framework of Ref. [100], these data provide strong, clear confirmation that the sign of $\Delta_\alpha(\vec{k})$ is opposite to that of $\Delta_\varepsilon(\vec{k})$.

6.4.1 Robustness of result

In addition to tests of the temperature dependence (Fig. 6.6) and robustness against changes in the integration area (Fig. 6.5) another important test is repetition of the experiment for different impurities. In order to test the generality of the result for $\rho_-(\omega)$, we repeat the analysis for two more impurities. The second impurity was in the same sample studied with the same tip, and its relative po-

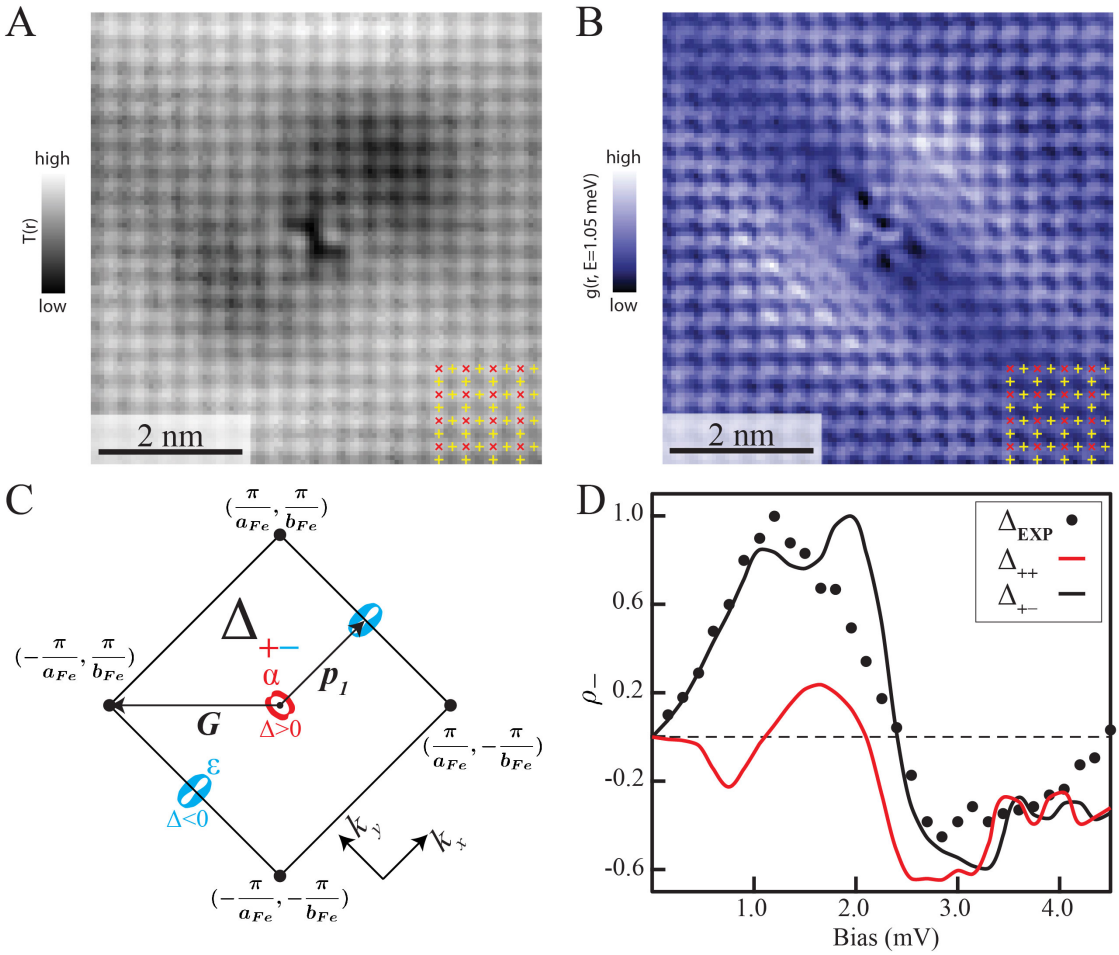

Figure 6.7: Measurement of relative sign of energy gaps in FeSe. A, Measured topograph $T(\vec{r})$ centered on a typical individual impurity site; ~ 6.5x6.5 nm^2 field of view. The surface (upper) Se sites are shown using red x symbol, and the Fe sites using yellow +. **B,** Measured BQPI $g(\vec{r}, E)$ in same field of view as A. **C,** Schematic visualization of FeSe interband scattering wavevector $\vec{p_1}$ between α- and ε-bands in $\vec{k}$-space for sign-changing order parameter. **D,** Predicted $\rho_-(E)$ for ± pairing symmetry using the band/gap structure of FeSe, shown as solid black curve. The measured $\rho_-(E)$ for FeSe is calculated by integrating around interpocket scattering vector $\vec{p_1}$, and is shown here as black dots. Predicted $\rho_-(E)$ for no gap sign change in FeSe shown as solid red curve.

sition to the first impurity can be seen in Figs. 6.8A-C. The third impurity was in a second sample, and was examined with a physically different tip. Its position is marked in the topograph in Fig. 6.8D.

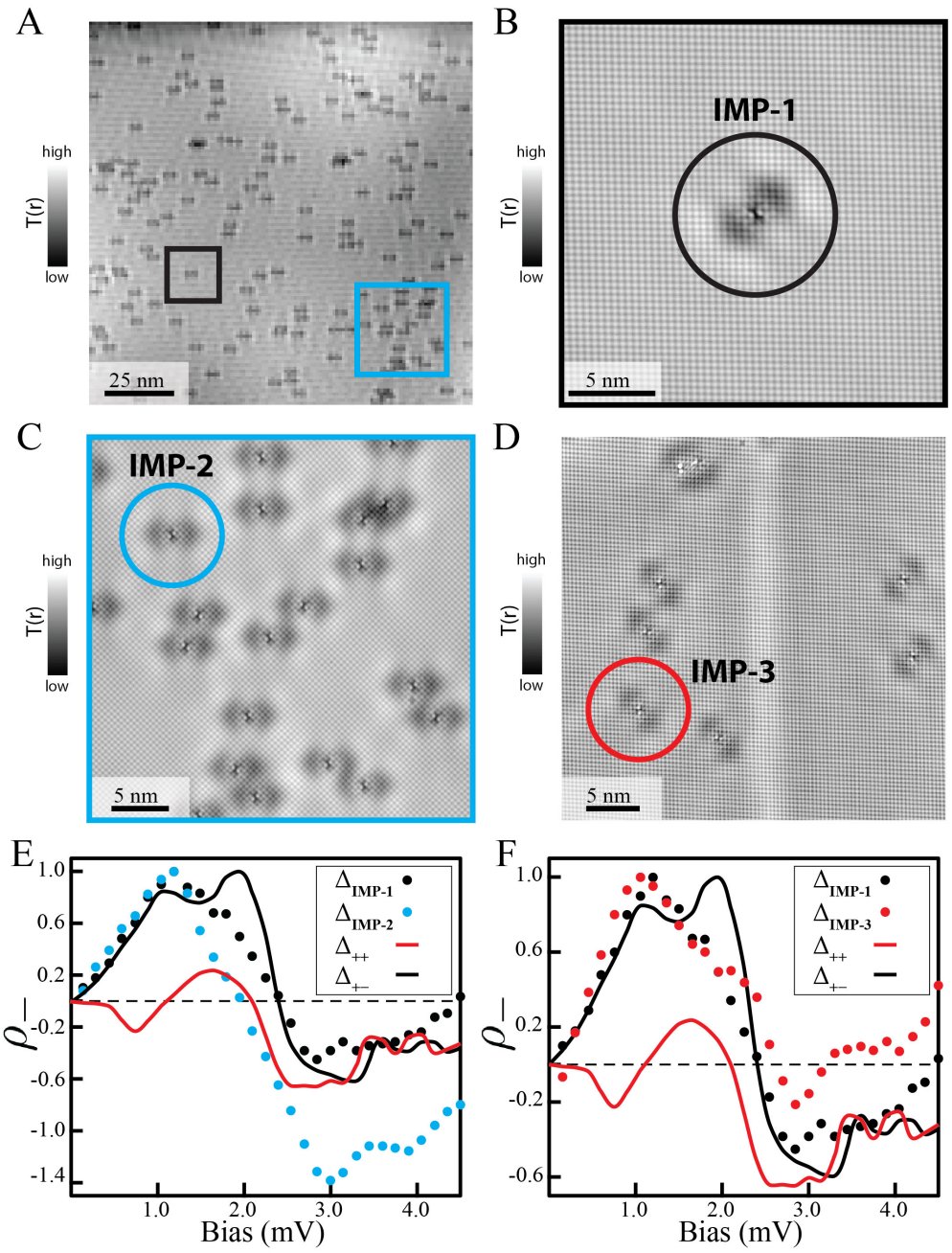

Figure 6.8: $\rho_-(\omega)$ **for three different impurities. A,** Constant current topography of a single domain in FeSe. The black and blue square mark the position of the topograph presented in B and C, respectively. **B,** Constant current topography of a single defect, referred to as impurity 1 in E and F. **C,** Constant current topography of several defects. The blue circle marks impurity 2. **D,** Constant current topography of several defects near a twin boundary in a second sample of FeSe studied by SI-STM. The red circle marks impurity 3. **E,** Comparison of $\rho_-(\omega)$ for impurities 1 and 2 of the same sample with theoretically predicted $\rho_-(\omega)$. **F,** Comparison of $\rho_-(\omega)$ for impurities 1 and 3 of two different FeSe samples with theoretically predicted $\rho_-(\omega)$.

For both additional impurities the results agree best with a sign-changing superconducting order parameter, see Figs. 6.8E, F. In order to make the visual comparison of experiment and theory easier, $\rho_-(\omega)$ has been normalized to its maximum value for all three impurities and the theoretically predicted case of Δ_{+-}. Theoretically predicted $\rho_-(\omega)$ for the case of Δ_{++} has been normalized so that the relative magnitude to the theoretically predicted case of Δ_{+-} is conserved. There is no signature of a sign change in $\rho_-(\omega)$ within $\omega \leq \Delta$ which is a clear indication for the Δ_{+-} scenario and rules out the sign-preserving order parameter within our modeling.

Importantly, the $g(\vec{r}, \omega)$ and $\rho_-(\omega)$ at the impurity studied in a second sample with a physically different tip, agrees remarkably well with the first, isolated impurity. From that we conclude that the result supporting sign-changing superconducting order is both very robust and intrinsic to the material studied.

We conclude this section with a look at the average tunneling spectrum in a $\sim$ 6.5x6.5 nm^2 field of view around the three impurities shown in Fig. 6.9. The two major differences are that the maximum gap coherence peak shifts slightly between the three impurities, and that the impurity close to the twin boundary (IMP-3) exhibits a prominent peak around $\sim \pm 1.5$ meV compared to the other two. The latter observation could be related to the proximity to the twin boundary [63].

Comparing the shift of the maximum gap coherence peak and $\rho_-(\omega)$ for the three impurities it seems to be true that a shift to a bigger (smaller) gap shifts the entry point from normal state scattering to superconducting state scattering to bigger (smaller) energies which intuitively seems reasonable. On the theoretical side the general robustness of the phase sensitive BQPI scattering scheme was recently investigated for more realistic models, and found to be generally

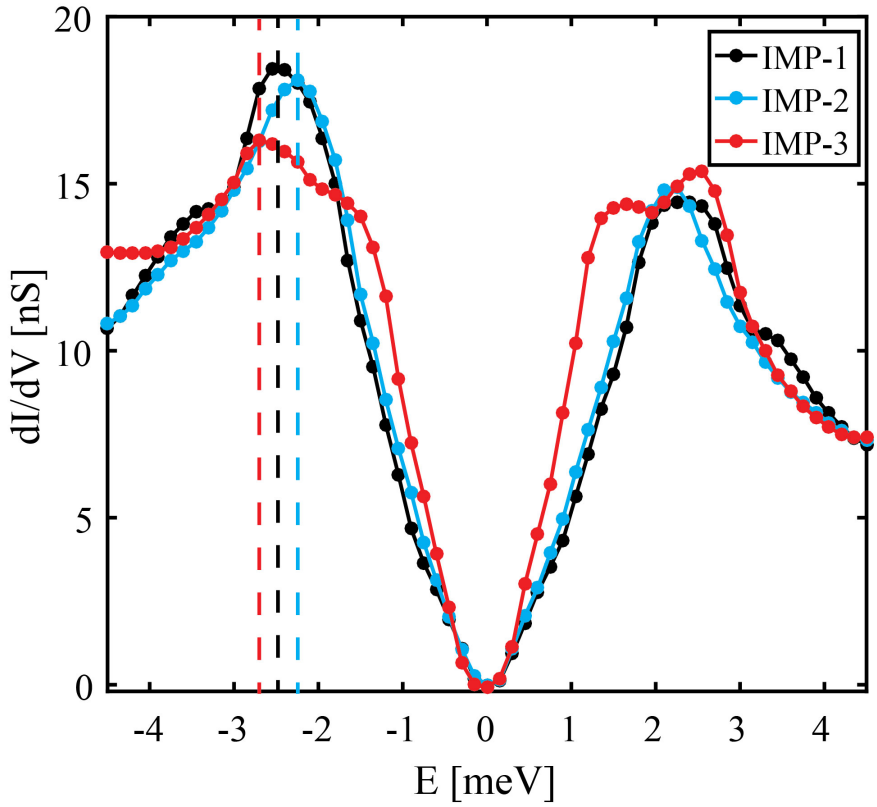

Figure 6.9: Tunneling conductance in vicinity of three different impurities. Average conductance in a ~ 6.5x6.5 nm^2 field of view around the three impurities shown in Fig. 6.8. The dashed lines serve as a guide to the eye, and identify the position of the maximum gap coherence peak.

robust [122].

CHAPTER 7

ORBITAL SELECTIVE COOPER PAIRING IN FESE

The authors of Ref. [69] concluded that the highly anisotropic, C_2-symmetric gap detected for the α-pocket in Fe(Se, S) cannot be explained within the framework of standard spin-fluctuation pairing models. We find an even more complicated situation in our BQPI studies of FeSe with a second highly anisotropic, C_2-symmetric gap on the ε-pocket. Calculations that use standard spin-fluctuation pairing model approaches indeed fail to reproduce such an exotic gap structure [27, 102]. This prompts the question if there is a missing ingredient, and we argue in the following that the answer is yes, and that the ingredient is orbital selectivity.

7.1 Gap magnitude and orbital content of the Fermi surface

First we remind the reader that orbital selective superconductivity predicts anisotropic gaps with gaps being large for parts of the Fermi surface where a specific orbital content dominates [60, 61]. Therefore, we compare in Fig. 7.1 the experimentally determined Fermi surface and gap structure magnitude and the $k_z = 0$ Fermi surface of our band structure and the contributions of the d_{xz}, d_{yz}, and d_{xy} orbitals on the Fermi surface. Greater line thickness corresponds to larger orbital contribution throughout. The correspondence between gap anisotropy and d_{yz}-orbital content is evident, and thus we postulate that Cooper pairing in FeSe is orbital selective with predominant pairing due to the electrons of the d_{yz}-orbitals.

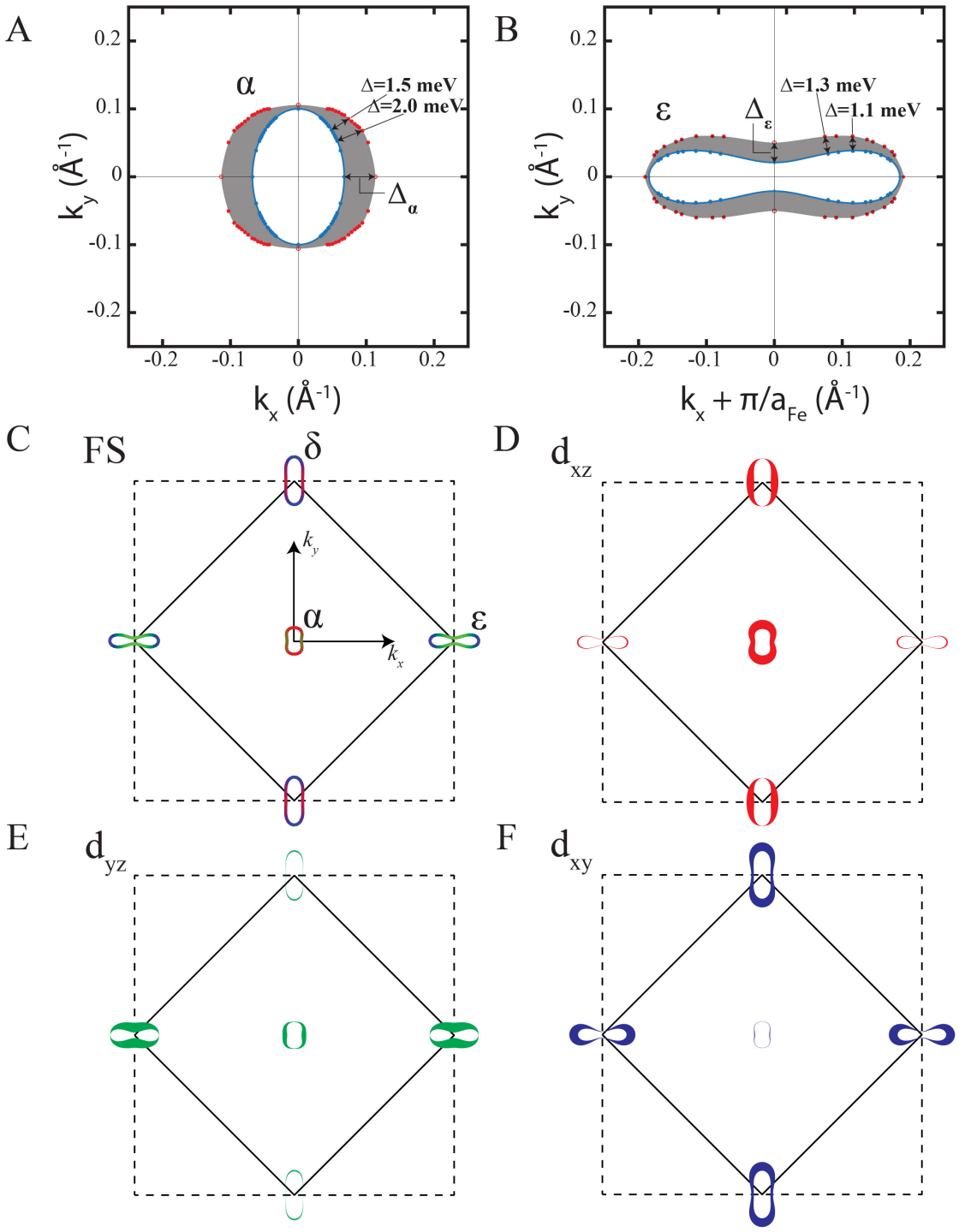

Figure 7.1: Comparison of gap anisotropy and orbital content of the individual Fermi surface pockets. A, Energy-gap magnitude for the α-band measured using BQPI. **B,** Energy-gap magnitude for the ε-band measured using BQPI. **C-F,** Upper left panel shows the Fermi surface at $k_z = 0$ for our band structure model (color code for orbital content as before). In the remaining three panels, the individual contributions of the main 3d-orbitals are shown explicitly on the Fermi surface (greater line thickness corresponding to bigger contribution).

7.2 Calculating the gap-symmetry function with and without orbital selectivity

Within a theoretical model for quasiparticles in a correlated material, one can parameterize the full Greens function using a quasiparticle weight $Z_{\mathbf{k}}$ and a modified dispersion $\tilde{E}_{\mathbf{k}}$ as $G(\mathbf{k},\omega) = Z_{\mathbf{k}}/(\omega + i0^{+} - \tilde{E}_{\mathbf{k}})$. Considering our approach to determine the quasiparticle energies by a fit to experimental results from ARPES, QO and SI-STM data for the present material, the corrections to $\tilde{E}_{\mathbf{k}}$ are already taken into account by the shifts and additional terms as outlined in chapter 3.

A calculation of the gap structure within a model that only takes into account the modified quasiparticle energies fails: From standard spin-fluctuation theory one obtains a rather small gap on the α-pocket (even slightly smaller than in earlier 3D calculations [102]) with limited anisotropy and a large gap on the ε-pocket, but with opposite anisotropy as shown in Fig. 7.2A. Furthermore, the spin-fluctuation spectrum is dominated by (π,π) fluctuations rather than $(\pi,0)$ fluctuations as observed in INS experiments [33, 123]. Neither imposing strong $(\pi,0)$ fluctuations 'by hand', nor using the slightly modified band structure of Ref. [102], which actually accounts well for the measured neutron measurements, resolves the discrepancy. We therefore turn to our postulate that the missing ingredient is strong orbital selectivity in the quasiparticle weights.

From many-body methods [108, 125] and recent experiments [40], it is known that the d_{xy} orbital is strongly renormalized, i.e. the quasiparticle weight $Z_{\mathbf{k}}$ is suppressed. In the nematic state one additionally expects that the quasiparticle weight of the d_{xz} orbital is different from that of the d_{yz} orbital. Using this information, one can dress the Greens function as derived from our tight-

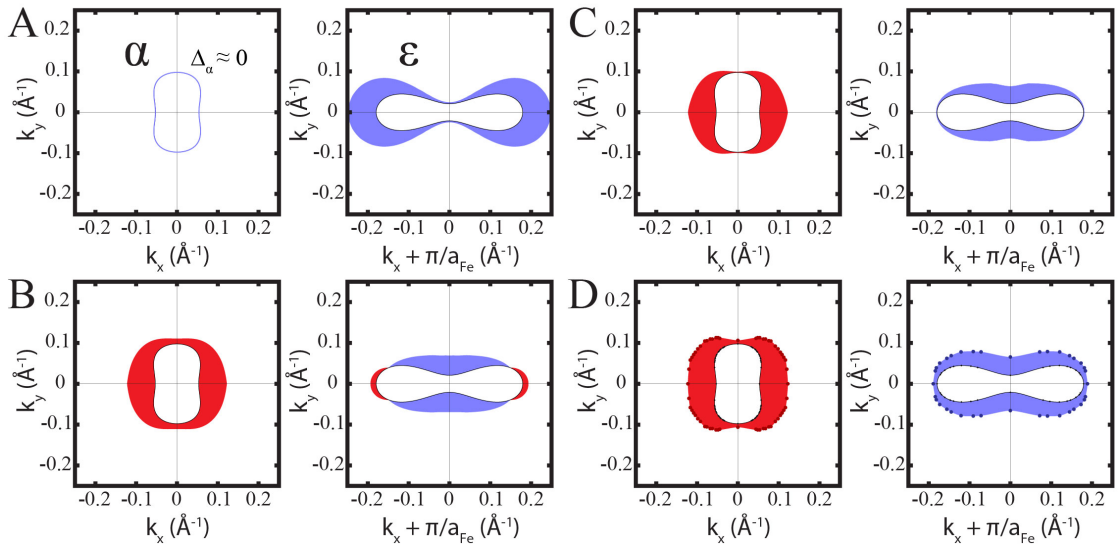

Figure 7.2: Results from calculations of the gap-symmetry function [104, 124]. **A,** Traditional spin-fluctuation theory of the present model, yielding a very small gap on the α-pocket and a large anisotropic gap on the ε-band (and δ-pocket not shown). Comparison to the experimental result in panel D shows a strong qualitative and quantitative discrepancy. **B,** Spin-fluctuation pairing using a susceptbility calculated with modified quasiparticle weights Z_α, eq. 7.1, yields a gap function that has some similarities to the measured order parameter from BQPI, whereas a nodal feature on the ε-band together with the sign change disagrees with experimental findings. **C,** Additionally imposing orbital selectivity in the pairing itself, e.g. suppressing pairing in the d_{xy} channel and in the d_{xz} channel according to their respective decoherence as described by the Z-factors when projecting the pairing interaction to momentum space, yields almost perfect agreement due to the dominant d_{yz} pairing. **D,** Superconducting gap deduced experimentally from BQPI. The gap symmetry functions in all models (A-C) were scaled to have the same maximum gap value that would agree with the main coherence peak observed in dI/dV spectra.

binding model with a simple multiplication of an orbital-dependent quasiparticle weight:

$$G_{ab}(\mathbf{k}, \omega) = Z_{ab} G^0_{ab}(\mathbf{k}, \omega) \tag{7.1}$$

where $Z_{ab} = \sqrt{Z_a}\sqrt{Z_b}$ is given by the geometric mean of the quasiparticle weights of the connected orbitals in the spirit of renormalizing the electron operators $c_a \rightarrow \sqrt{Z_a} c_a$.

This approach modifies the pairing interaction in orbital space and thus also in-

fluences the superconducting gap found when solving the linearized gap equation [104,124] or the Bogoliubov de Gennes equation self-consistently [119,120]. In a simple picture, it suppresses pair scattering from and to d_{xy} orbitals and d_{xz} orbitals, as they are less coherent. Within this approach, the resulting gap gets much more anisotropic because the only left over orbital channel (with significant orbital contribution close to the Fermi level) is d_{yz}.

To illustrate the drastic changes upon orbital selectivity, we strongly suppress the weight of the d_{xy} orbital and moderately suppress the d_{xz} orbital to calculate the spin susceptibility using eq. 7.1 instead of the bare Green function $G^0_{ab}(\mathbf{k},\omega)$. Calculating the pairing interaction and solving the linearized gap equation [104, 124] we obtain a gap function as shown in Fig. 7.2B. Obviously, the trends in the anisotropy and the relative magnitudes of the gaps are drastically changed. At the same time, the susceptibility becomes more $(\pi, 0)$ dominated, consistent with Refs. [33, 123]. Finally, we note that the electronic states themselves may show properties of decoherence according to the quasiparticle weights in band space.

To demonstrate the implementation of this effect, we perform a pairing calculation where additionally pairing in the d_{xy} (d_{xz}) states is relatively suppressed according to the decoherence of these states described by the Z-factors. In this calculation, the decoherence enters via the susceptibility and as additional prefactors through the matrix elements when projecting the pairing interaction from orbital to band space, such that an almost perfect agreement between theoretical result and experiment is obtained, see Figs. 7.2C, D.

7.3 Summary of results

In summary: by introducing Bogoliubov quasiparticle interference (BQPI) imaging to FeSe studies, we measure the coherent Fermi surface geometries and superconducting energy gaps $\Delta_\alpha(\vec{k})$ and $\Delta_\varepsilon(\vec{k})$ for its α-band and ε-band (chapter 5). We show directly that both gaps are exceptionally anisotropic yet nodeless [64–68], are aligned along orthogonal axes, and are of opposite sign (chapter 6). This complex configuration of energy gaps, which was unforeseen by theoretical studies of FeSe, reveals a unique new form of superconductivity based on orbital selective Cooper pairing of electrons predominantly from the d_{yz} orbitals of Fe atoms.

Figures 7.3A, B visualize the key results of our study: the measured values of $\Delta_\alpha(\vec{k})$, $\Delta_\varepsilon(\vec{k})$ are both extremely anisotropic but nodeless, each having C_2- symmetry with deep minima that are aligned along orthogonal crystal axes. Recalling that our x-axis is defined to always be the orthorhombic a_{Fe}-axis, these results are found equally true in both nematic domains. Not only is such a gap structure unanticipated, it is actually highly divergent from standard spin-fluctuation pairing theory [27] which yield a weak almost isotropic gap on the α-band and a strong gap on the ε-band but with the opposite anisotropy.

Remarkably, however, orbital selective pairing concentrated in the d_{yz} channel can provide an explanation for the observed $\Delta_\alpha(\vec{k})$ and $\Delta_\varepsilon(\vec{k})$. Figure 7.3B shows our measured angular dependence of $\Delta_\alpha(\vec{k})$ about $\Gamma = (0,0)$ and the equivalent for $\Delta_\varepsilon(\vec{k})$ about $X = (\pi/a_{Fe}, 0)$. For a d_{yz} orbital selective pairing interaction peaked at wavevector $\vec{q} = (\pi/a_{Fe}, 0)$, the predicted angular dependence of $\Delta_\alpha(\vec{k})$ and $\Delta_\varepsilon(\vec{k})$ is shown in Fig. 7.3C. The detailed quantitative agreement between the structure of measured $\Delta_\alpha(\vec{k})$, $\Delta_\varepsilon(\vec{k})$ in panel B and the predictions for $\Delta_\alpha(\vec{k})$,

$\Delta_\varepsilon(\vec{k})$ in panel C, denotes the existence of orbital selective Cooper pairing in FeSe.

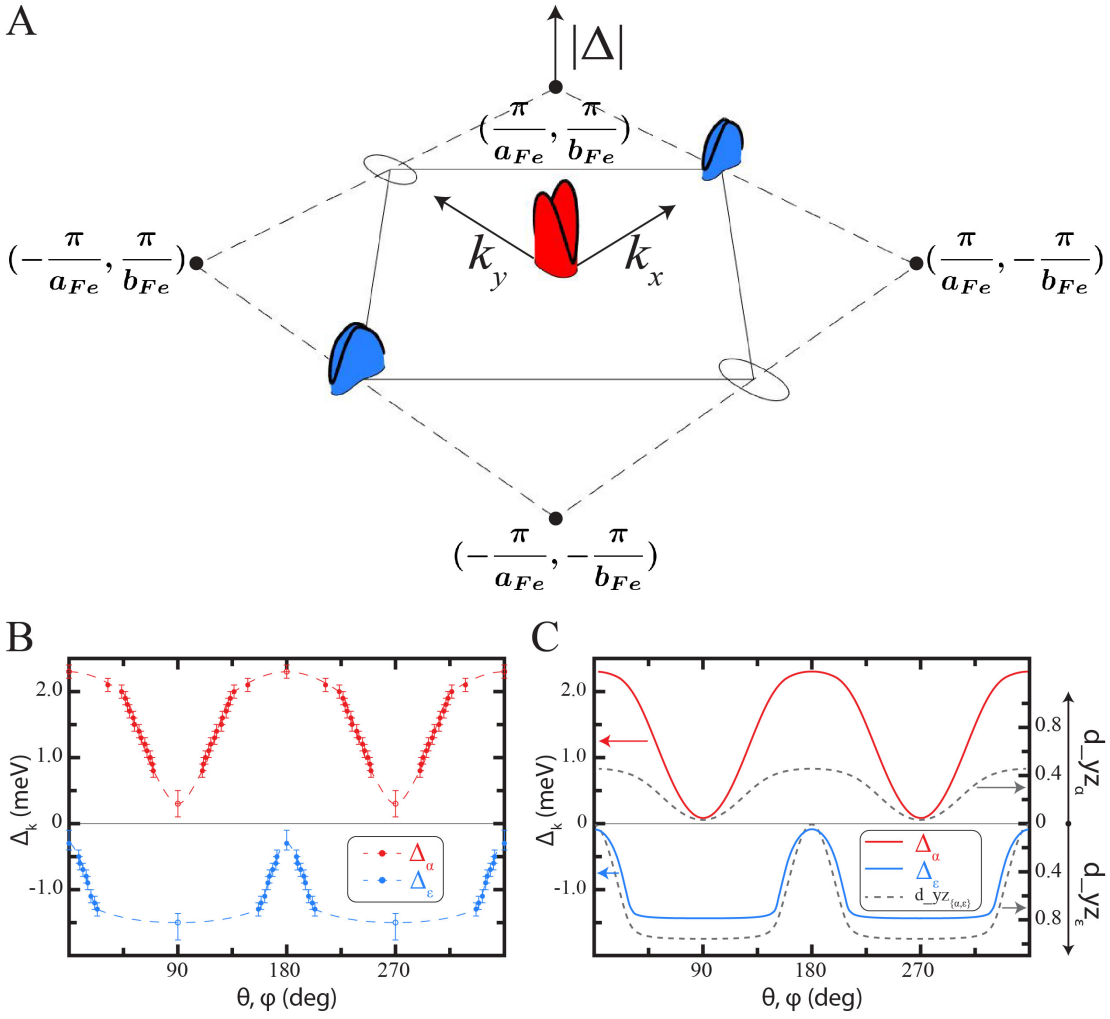

Figure 7.3: Orbital selective Cooper pairing in FeSe. **A,** Measured $\vec{k}$-space structure of anisotropic energy gaps of FeSe. The red and blue colors indicate the different signs of the two gap functions. Neither band nor gap were detected for the δ-pocket by SI-STM. **B,** Measured angular dependence of FeSe superconducting energy-gaps $\Delta_\alpha(\vec{k})$ about $\Gamma = (0,0)$ and the equivalent for $\Delta_\varepsilon(\vec{k})$ about $X = (\pi/a_{Fe}, 0)$. **C,** Predicted angular dependence of $\Delta_\alpha(\vec{k})$ and $\Delta_\varepsilon(\vec{k})$ for an interband pairing interaction that is peaked at $\vec{q} = (\pi/a_{Fe}, 0)$ and for which pairing occurs predominantly for electrons with d_{yz} orbital character. The correspondence with B is persuasive. The dashed grey curves show the d_{yz} orbital character of states at the α-band and ε-band Fermi surfaces.

Such orbital selective Cooper pairing may arise from differences in correlation-strength for electrons with different orbital character. For example, correlations sufficient to generate incoherence for states with predominantly d_{xy} orbital character [40, 41] would suppress their pairing completely within an itinerant picture. Moreover, superconducting FeSe must exhibit distinct quasiparticle weights at the Fermi surface for states with d_{xz} and d_{yz} orbital character, due to the nematic state [11, 12].

Obviously such a model could provide a rationale for why the δ-band, predominantly associated with the d_{xy} orbital, has weak visibility by ARPES [40, 41] and BQPI, and could also account similarly for a low energy spin-susceptibility that is dominant at $\vec{q} = (\pi/a_{Fe}, 0)$ consistent with INS data [123]. By projecting this form of orbital selective pairing interaction onto the Fermi surfaces of FeSe, the gap functions can be predicted by solving the linearized gap equation (Ref. [27]). The resulting predicted $\Delta_\alpha(\vec{k})$ and $\Delta_\varepsilon(\vec{k})$ (solid curves Fig. 7.3C) are quantitatively consistent with the extremely anisotropic structure and sign reversal of the measured gap functions (Figs. 7.3A, B). Moreover, as the magnitudes of $\Delta_\alpha(\vec{k})$ and $\Delta_\varepsilon(\vec{k})$ (solid curves Figs. 7.3B, C) track the strength of d_{yz} orbital character on both bands (dashed curves Fig. 7.3C; Refs. [27, 54, 102]), the effects of orbital selectivity on the pairing are directly discernible.

CHAPTER 8

OUTLOOK

Discovery of orbital selective superconductivity in the multi-orbital, chalcogenide superconductor FeSe both opens the way for general studies of orbital selective interactions and ordering, and also emphasizes the role of strong correlations in iron-based high temperature superconductivity. This is an intriguing result, since it potentially paves the way to unify the copper- and iron-based superconductors [37].

L. de' Medici and coworkers argue that selective Mott physics is the key to understanding iron-based superconductors, and that the electronic states derived from the individual 3d orbitals can be viewed as separate doped Mott insulator states. They speculate that a phase diagram based on the average 3d orbital doping could bring together copper- and iron-based superconductivity under a unified framework [37].

If the scenario above was true the main question for future experiments in pnictides and chalcogenides would then be if additional cases of orbital selective Mottness and orbital selective superconductivity can be found. In the following, I will focus on possible STM experiments, and refer the interested reader to the literature for other experimental techniques [37, 39–41].

For the decision which materials should be primarily targeted, calculations by Z. P. Yin et al. [23] could provide guidance which materials should be prioritized in the search for orbital selective physics. FeTe is predicted to be the most strongly correlated chalcogenide [23], and thus seems to be a logical choice. However, the existence of the bi-collinear AFM order at low temperatures, see for example [49], could complicate its study, and as it is not superconducting, studies would need to concentrate on the normal state properties.

On the pnictide side, strong correlations are predicted to occur both in LiFeAs and NaFeAs [23]. Since in LiFeAs neither a nematic nor a magnetically ordered phase coexist with the superconductivity, LiFeAs could provide the possibility to study orbital selective correlations in a metal without the complications of coexisting ordered electronic phases. NaFeAs on the other hand is both nematic and antiferromagnetically ordered. Finally, the 122 family of iron-based superconductors has the advantage that it is both readily hole and electron doped as discussed by de' Medici et al. [37].

In order to identify further orbital selective superconductors one needs to search for anisotropic gap structures, and obtain orbitally resolved band structures for the model calculations. As it turns out two possible candidates for orbital selective superconductivity besides bulk FeSe might already exist based on available data: The above mentioned LiFeAs and monolayer FeSe. In spirit of the theory presented in chapter 7, orbital selective pairing was applied to the FeSe monolayer and LiFeAs system, and successfully reduces discrepancies between experimentally observed anisotropic gap structures and standard spin-fluctuation pairing models [126].

Beyond FeSe and LiFeAs, BQPI imaging experiments have the potential to play an important role in the search and exploration of new materials with anisotropic gap structures due to their unrivaled precision [80–82]. In this context it is also of interest to apply the introduced phase sensitive BQPI scattering technique to other iron-based superconductors, as the (non-)existence of sign changes in the gap structure is important to distinguish possible pairing scenarios [13]. Chalcogenide superconductors where the Fermi surface misses the hole pockets are prime candidates, and the scientific question would be if there is a sign change between the electron pockets at the X- and Y-point [122].

In the normal state electronic structure, quasiparticle interference imaging could be used to detect orbital selective Mottness. The large modification of quasiparticle weights Z implies that quasiparticle scattering in the normal state should be strongly affected: QPI should be strongest for the parts of the band structure comprised of coherent electrons which in the specific case of FeSe would be predominantly the d_{yz}-electrons. In this context, it is an important open question if the effects of orbital selective Mottness on QPI can be distinguished or separated from the effects of antiferromagnetic order in materials as for example NaFeAs [127].

On the theory side, the weakness of the current orbital selective pairing calculation lies in its phenomenological nature which is based on fitting the quasiparticle weights, instead of calculating them from microscopic models. Normal state QPI experiments are therefore an important independent test of the proposed quasiparticle weights Z from orbital selective pairing calculations. The ideal case would be if the quasiparticle weights Z could be directly determined from QPI [128] or ARPES [129] experiments.

Therefore, it is important to explore if the quasiparticle weights Z deduced from fits to experiments can be calculated from microscopic models. This should be accompanied by efforts to explain the orbital selective nature of pairing within microscopic models. In this light, the recent proposal for the mechanism of nematic superconductivity in FeSe by She et al. holds great promise [57].

Finally, it should be explored if orbital selective physics is important in strongly correlated materials beyond the iron-based superconductors. Materials that contain transition metals with not completely filled electronic configurations for d orbitals are of primary interest, and so far the ruthenates are proving to be very promising candidates based on existing studies [58, 130].

In conclusion, the interplay and interaction of multiple orbitals has the potential to produce extremely rich physics in strongly correlated materials [58] which in turn creates opportunities to discover novel and diverse phenomena in the future: A future that ultimately could hold the key to the mystery of unconventional copper- and iron-based superconductivity [37].

BIBLIOGRAPHY

[1] R. de Bruyn Ouboter. Heike Kamerlingh Onnes's discovery of superconductivity. *Scientific American*, March, 98–103, 1997.

[2] D. van Delft and P. Kes. The discovery of superconductivity. *Physics Today*, September, 38–43, 2010.

[3] J. G. Bednorz and K. A. Müller. Possible high T_C superconductivity in the Ba-La-Cu-O system. *Zeitschrift fúr Physik B*, 64, 189–193, 1986.

[4] L. Taillefer. Scattering and pairing in cuprate superconductors. *Annual Review Condensed Matter Physics*, 1, 51–70, 2010.

[5] Y. Kamihara, T. Watanabe, T. Hirano, and H. Hosono. Iron-based layered superconductor $La[O_{1-x}F_x]FeAs(x = 0.05 - 0.12)$ with $T_C = 26K$. *Journal of the American Chemical Society*, 130, 3296–3297, 2008.

[6] A. A. Kordyuk. Iron-based superconductors : Magnetism , superconductivity , and electronic structure (Review Article). *Fiz. Nizk.Temp.*, 38, 888–899, 2012.

[7] A. P. Drozdov, M. I. Eremets, and I. A. Troyan. Conventional superconductivity at 190 K at high pressures. *Arxiv Preprint*, 1412.0460, 1986.

[8] A. P. Drozdov, M. I. Eremets, V. Troyan, I. A. Ksenofontov, and S. I. Shylin. Conventional superconductivity at 203 kelvin at high pressures in the sulfur hydride system. *Nature*, 525, 73–76, 2015.

[9] Q.-Y. Wang, Z. Li, W.-H. Zhang, Z.-C. Zhang, J.-S. Zhang, W. Li, H. Ding, Y.-B. Ou, P. Deng, K. Chang, J. Wen, C.-L. Song, K. He, J.-F. Jia, S.-H. Ji, Y.-Y. Wang, L.-L. Wang, X. Chen, X.-C. Ma, and Q.-K. Xue. Interface-induced high-temperature superconductivity in single unit-cell FeSe films on $SrTiO_3$. *Chinese Physics Letters*, 29, 037402, 2012.

[10] Z. Zhang, Y.-H. Wang, Q. Song, C. Liu, R. Peng, K. A. Moler, D. Feng, and Y. Wang. Onset of the Meissner effect at 65 K in FeSe thin film grown on Nb-doped $SrTiO_3$ substrate. *Science Bulletin*, 60, 1301–1304, 2015.

[11] D.-H. Lee. What makes the T_C of $FeSe/SrTiO_3$ so high? *Chinese Physics B*, 24, 117405, 2015.

[12] P. J. Hirschfeld. Using gap symmetry and structure to reveal the pairing mechanism in Fe-based superconductors. *Comptes Rendus Physique*, 17, 197–231, 2016.

[13] I. I. Mazin and J. Schmalian. Pairing symmetry and pairing state in ferropnictides: Theoretical overview. *Physica C*, 469, 614–627, 2009.

[14] V. Cvetkovic and Z. Tesanovic. Multiband magnetism and superconductivity in Fe-based compounds. *Europhysics Letters*, 85, 37002, 2009.

[15] J. Paglione and R. L. Greene. High-temperature superconductivity in iron-based materials. *Nature Physics*, 6, 645–658, 2010.

[16] F. Wang and D.-H. Lee. The electron-pairing mechanism of iron-based superconductors. *Science*, 332, 200–204, 2011.

[17] P. J. Hirschfeld, M. M. Korshunov, and I. I. Mazin. Gap symmetry and structure of Fe-based superconductors. *Reports on Progress in Physics*, 74, 124508, 2011.

[18] A. Chubukov. Pairing mechanism in Fe-based superconductors. *Annual Review of Condensed Matter Physics*, 3, 57–92, 2012.

[19] F. Yang, F. Wang, and D.-H. Lee. Fermiology, orbital order, orbital fluctuations, and Cooper pairing in iron-based superconductors. *Physical Review B*, 88, 100504(R), 2013.

[20] Q. Si, R. Yu, and E. Abrahams. High-temperature superconductivity in iron pnictides and chalcogenides. *Nature Reviews Materials*, 16017, 1–15, 2016.

[21] A. V. Chubukov, M. Khodas, and R. M. Fernandes. Magnetism, superconductivity, and spontaneous orbital order in iron-based superconductors: which comes first and why? *Physical Review X*, 6, 041045, 2016.

[22] R. M. Fernandes and A. V. Chubukov. Low-energy microscopic models for iron-based superconductors: a review. *Reports on Progress in Physics*, 80, 014503, 2017.

[23] Z. P. Yin, K. Haule, and G. Kotliar. Kinetic frustration and the nature of the magnetic and paramagnetic states in iron pnictides and iron chalcogenides. *Nature Materials*, 10, 932–935, 2011.

[24] J. Hu, L. Congcong, and X. Wu. Predicting unconventional high-temperature superconductors in trigonal bipyramidal coordinations. *Physical Review X*, 5, 041012, 2015.

[25] B. A. Averill and P. Eldredge. *Principles of General Chemistry*, volume 1.0, pp. 2813–2836. Published under Creative Commons by-nc-sa 3.0, 2012.

[26] H. Eschrig and K. Koepernik. Tight-binding models for the iron-based superconductors. *Physical Review B*, 80, 104503, 2009.

[27] S. Mukherjee, A. Kreisel, P. J. Hirschfeld, and B. M. Andersen. Model of electronic structure and superconductivity in orbitally ordered FeSe. *Physical Review Letters*, 115, 026402, 2015.

[28] S. Kasahara, H. J. Shi, K. Hashimoto, S. Tonegawa, Y. Mizukami, T. Shibauchi, K. Sugimoto, T. Fukuda, T. Terashima, A. H. Nevidomskyy, and Y. Matsuda. Electronic nematicity above the structural and superconducting transition in $BaFe_2(As_{1-x}P_x)_2$. *Nature*, 486, 382–385, 2012.

[29] I. R. Fisher, L. Degiorgi, and Z. X. Shen. In-plane electronic anisotropy of underdoped '122' Fe-arsenide superconductors revealed by measurements of detwinned single crystals. *Reports on Progress in Physics*, 74, 124506, 2011.

[30] R. M. Fernandes, A. V. Chubukov, and J. Schmalian. What drives nematic order in iron-based superconductors? *Nature Physics*, 10, 97–104, 2014.

[31] W. Lv, J. Wu, and P. Phillips. Orbital ordering induces structural phase transition and the resistivity anomaly in iron pnictides. *Physical Review B*, 80, 224506, 2009.

[32] P. Dai, J. Hu, and E. Dagotto. Magnetism and its microscopic origin in iron-based high-temperature superconductors. *Nature Physics*, 8, 709–718, 2012.

[33] Q. Wang, Y. Shen, B. Pan, X. Zhang, K. Ikeuchi, K. Iida, A. D. Christianson, H. C. Walker, D. T. Adroja, M. Abdel-Hafiez, X. Chen, D. A. Chareev, A. N. Vasiliev, and J. Zhao. Magnetic ground state of FeSe. *Nature Communications*, 7, 12182, 2016.

[34] S. Blundell. *Magnetism in Condensed Matter*. Oxford Master Series In Condensed Matter Physics. Oxford University Press, 2001.

[35] F. Wang, S. A. Kivelson, and D.-H. Lee. Nematicity and quantum paramagnetism in FeSe. *Nature Physics*, 11, 959–963, 2015.

[36] J. K. Glasbrenner, I. I. Mazin, H. O. Jeschke, P. J. Hirschfeld, R. M. Fernandes, and R. Valentí. Effect of magnetic frustration on nematicity and superconductivity in Fe chalcogenides. *Nature Physics*, 11, 953–958, 2015.

[37] L. de' Medici, G. Giovannetti, and M. Capone. Selective Mott physics as a key to iron superconductors. *Physical Review Letters*, 112, 177001, 2014.

[38] M. Aichhorn, S. Biermann, T. Miyake, A. Georges, and M. Imada. Theoretical evidence for strong correlations and incoherent metallic state in FeSe. *Physical Review B*, 82, 064504, 2010.

[39] Z. K. Liu, M. Yi, Y. Zhang, J. Hu, R. Yu, J. X. Zhu, R. H. He, Y. L. Chen, M. Hashimoto, R. G. Moore, S. K. Mo, Z. Hussain, Q. Si, Z. Q. Mao, D. H. Lu, and Z. X. Shen. Experimental observation of incoherent-coherent crossover and orbital-dependent band renormalization in iron chalcogenide superconductors. *Physical Review B*, 92, 235138, 2015.

[40] M. Yi, Z.-K. Liu, Y. Zhang, R. Yu, J.-X. Zhu, J. J. Lee, R. G. Moore, F. T. Schmitt, W. Li, S. C. Riggs, J.-H. Chu, B. Lv, J. Hu, M. Hashimoto, S.-K. Mo, Z. Hussain, Z.-Q. Mao, C. W. Chu, I. R. Fisher, Q. Si, Z.-X. Shen, and D. H. Lu. Observation of universal strong orbital-dependent correlation effects in iron chalcogenides. *Nature Communications*, 6, 7777, 2015.

[41] Z. Wang, V. Tsurkan, M. Schmidt, A. Loidl, and J. Deisenhofer. Tuning orbital-selective correlations in superconducting $Rb_{0.75}Fe_{1.6}Se_{2-z}S_z$. *Physical Review B*, 93, 104522, 2016.

[42] K. Kothapalli, A. E. Böhmer, W. T. Jayasekara, B. G. Ueland, P. Das, A. Sapkota, V. Taufour, Y. Xiao, E. Alp, S. L. Bud'ko, P. C. Canfield, A. I. Kreyssig, and A. Goldman. Strong cooperative coupling of pressure-induced magnetic order and nematicity in FeSe. *Nature Communications*, 7, 12728, 2016.

[43] G.-Y. Chen, X. Zhu, H. Yang, and H.-H. Wen. Highly anisotropic superconducting gaps and possible evidence of antiferromagnetic order in FeSe single crystals. *Arxiv Preprint*, 1703.08680v1F, 2017.

[44] M. A. Tanatar, A. E. Böhmer, E. I. Timmons, M. Schütt, G. Drachuck, V. Taufour, K. Kothapalli, A. Kreyssig, S. L. Bud'ko, P. C. Canfield, R. M. Fernandes, and R. Prozorov. Origin of the resistivity anisotropy in the nematic phase of FeSe. *Physical Review Letters*, 117, 127001, 2016.

[45] X. Liu, L. Zhao, S. He, J. He, D. Liu, D. Mou, B. Shen, Y. Hu, J. Huang, and X. J. Zhou. Electronic structure and superconductivity of FeSe-related superconductors. *Journal of Physics: Condensed Matter*, 27, 183201, 2015.

[46] S. Shamoto, K. Matsuoka, R. Kajimoto, M. Ishikado, T. Watashige, S. Kasahara, M. Nakamura, H. Kontani, T. Shibauchi, and Y. Matsuda. Spin nematic susceptibility studied by inelastic neutron scattering in FeSe. *Arxiv Preprint*, 1511.04267, 2015.

[47] R. Yu and Q. Si. Antiferroquadrupolar and Ising-Nematic orders of a frustrated ilinear-Biquadratic Heisenberg model and implications for the magnetism of FeSe. *Physical Review Letters*, 115, 116401, 2015.

[48] H.-H. Lai, S.-S. Gong, W.-J. Hu, and Q. Si. Frustrated magnetism and bicollinear antiferromagnetic order in FeTe. *Arxiv Preprint*, 1608.08206, 2016.

[49] M. Enayat, Z. Sun, U. R. Singh, R. Aluru, S. Schmaus, A. Yaresko, Y. Liu, V. Tsurkan, A. Loidl, J. Deisenhofer, and P. Wahl. Real-space imaging of the atomic-scale magnetic structure of $Fe_{1+y}Te$. *Science*, 345, 653–656, 2014.

[50] S. Margadonna, Y. Takabayashi, M. T. McDonald, K. Kasperkiewicz, Y. Mizuguchi, Y. Takano, A. N. Fitch, E. Suard, and K. Prassides. Crystal structure of the new $FeSe_{1-x}$ superconductor. *Chemical Communications*, 5607–5609, 2008.

[51] C. Koz, M. Schmidt, H. Borrmann, U. Burkhardt, S. Rößler, W. Carrillo-Cabrera, W. Schnelle, U. Schwarz, and Y. Grin. Synthesis and crystal growth of tetragonal $\beta - Fe_{1.00}Se$. *Zeitschrift für Anorganische und Allgemeine Chemie*, 640, 1600–1606, 2014.

[52] E. Pomjakushina, K. Conder, V. Pomjakushin, M. Bendele, and R. Khasanov. Synthesis, crystal structure, and chemical stability of the superconductor $FeSe_{1-x}$. *Physical Review B*, 80, 024517, 2009.

[53] C.-L. Song, Y.-L. Wang, P. Cheng, Y.-P. Jiang, W. Li, T. Zhang, Z. Li, K. He, L. Wang, J.-F. Jia, H.-H. Hung, C. Wu, X. Ma, X. Chen, and Q.-K. Xue. Direct observation of nodes and twofold symmetry in FeSe superconductor. *Science*, 332, 1410–1413, 2011.

[54] Y. Suzuki, T. Shimojima, T. Sonobe, A. Nakamura, M. Sakano, H. Tsuji, J. Omachi, K. Yoshioka, M. Kuwata-Gonokami, T. Watashige,

R. Kobayashi, S. Kasahara, T. Shibauchi, Y. Matsuda, Y. Yamakawa, H. Kontani, and K. Ishizaka. Momentum-dependent sign inversion of orbital order in superconducting FeSe. *Physical Review B*, 92, 205117, 2015.

[55] M. D. Watson, T. K. Kim, L. C. Rhodes, M. Eschrig, M. Hoesch, A. A. Haghighirad, and A. I. Coldea. Evidence for unidirectional nematic bond ordering in FeSe. *Physical Review B*, 94, 201107(R), 2016.

[56] M. D. Watson, T. K. Kim, A. A. Haghighirad, N. R. Davies, A. McCollam, A. Narayanan, S. F. Blake, Y. L. Chen, S. Ghannadzadeh, A. J. Schofield, M. Hoesch, C. Meingast, T. Wolf, and A. I. Coldea. Emergence of the nematic electronic state in FeSe. *Physical Review B*, 91, 155106, 2015.

[57] J.-H. She, M. J. Lawler, and E.-A. Kim. Mechanism for nematic superconductivity in FeSe. *Arxiv Preprint*, 1701.07813, 2017.

[58] A. Georges, L. de' Medici, and J. Mravlje. Strong correlations from Hund's coupling. *Annual Review of Condensed Matter Physics*, 4, 137–178, 2013.

[59] R. Yu, J.-X. Zhu, and Q. Si. Orbital-dependent effects of electron correlations in microscopic models for iron-based superconductors. *Current Opinion in Solid State and Materials Science*, 17, 65–71, 2013.

[60] N. Arakawa and M. Ogata. Orbital-selective superconductivity and the effect of lattice distortion in iron-based superconductors. *Journal of the Physical Society of Japan*, 80, 074704, 2011.

[61] R. Yu, J.X. Zhu, and Q. Si. Orbital-selective superconductivity, gap anisotropy, and spin resonance excitations in a multiorbital $t - J_1 - J_2$-model for iron pnictides. *Physical Review B*, 89, 024509, 2014.

[62] S. Kasahara, T. Watashige, T. Hanaguri, Y. Kohsaka, T. Yamashita, Y. Shimoyama, Y. Mizukami, R. Endo, H. Ikeda, K. Aoyama, T. Terashima, S. Uji, T. Wolf, H. v. Löhneysen, T. Shibauchi, and Y. Matsuda. Field-induced superconducting phase of FeSe in the BCS-BEC cross-over. *Proceedings of the National Academy of Sciences*, 111, 16309–16313, 2014.

[63] T. Watashige, Y. Tsutsumi, T. Hanaguri, Y. Kohsaka, S. Kasahara, A. Furusaki, M. Sigrist, C. Meingast, T. Wolf, H. v. Löhneysen, T. Shibauchi, and Y. Matsuda. Evidence for time-reversal symmetry breaking of the superconducting state near twin-boundary interfaces in FeSe revealed by scanning tunneling spectroscopy. *Physical Review X*, 5, 031022, 2015.

[64] R. Khasanov, K. Conder, E. Pomjakushina, A. Amato, C. Baines, Z. Bukowski, J. Karpinski, S. Katrych, H.-H. Klauss, H. Luetkens, A. Shengelaya, and N. D. Zhigadlo. Evidence of nodeless superconductivity in $FeSe_{0.85}$ from muon-spin-rotation study of the in-plane magnetic penetration depth. *Physical Review B*, 78, 220510(R), 2008.

[65] M. Li, N. R. Lee-Hone, S. Chi, R. Liang, W. N. Hardy, D. A. Bonn, E. Girt, and D. M. Broun. Superfluid density and microwave conductivity of FeSe superconductor: ultra-long-lived quasiparticles and extended s-wave energy gap. *New Journal of Physics*, 18, 082001, 2016.

[66] P. Bourgeois-Hope, S. Chi, D. A. Bonn, R. Liang, W. N. Hardy, T. Wolf, C. Meingast, N. Doiron-Leyraud, and L. Taillefer. Thermal conductivity of the iron-based superconductor FeSe: nodeless gap with a strong two-band character. *Physical Review Letters*, 117, 097003, 2016.

[67] S. Teknowijoyo, K. Cho, M. A. Tanatar, J. Gonzales, A. E. Böhmer, O. Cavani, V. Mishra, P. J. Hirschfeld, S. L. Bud'ko, P. C. Canfield, and R. Prozorov. Enhancement of superconducting transition temperature by point-like disorder and anisotropic energy gap in FeSe single crystals. *Physical Review B*, 94, 064521, 2016.

[68] L. Jiao, C.-L. Huang, S. Rößler, C. Koz, U. K. Rößler, U. Schwarz, and S. Wirth. Direct evidence for multi-gap nodeless superconductivity in FeSe. *Arxiv Preprint*, 1605.01908, 2016.

[69] H. C. Xu, X. H. Niu, D. F. Xu, J. Jiang, Q. Yao, Q. Y. Chen, Q. Song, M. Abdel-Hafiez, D. A. Chareev, A. N. Vasiliev, Q. S. Wang, H. L. Wo, J. Zhao, R. Peng, and D. L. Feng. Highly anisotropic and twofold symmetric superconducting gap in nematically ordered $FeSe_{0.93}S_{0.07}$. *Physical Review Letters*, 117, 157003, 2016.

[70] G. Binnig, H. Rohrer, Ch. Gerber, and E. Weibel. Surface studies by Scanning Tunneling Microscopy. *Physical review Letters*, 49, 57–61, 1982.

[71] G. Binnig, H. Rohrer, Ch. Gerber, and E. Weibel. Tunneling through a controllable vacuum gap. *Applied Physics Letters*, 40, 178–180, 1982.

[72] G. Binnig, H. Rohrer, Ch. Gerber, and E. Weibel. 7x7 reconstruction on Si(111) resolved in real space. *Physical Review Letters*, 50, 120-123, 1983.

[73] Ø. Fischer, M. Kugler, I. Maggio-Aprile, C. Berthod, and C. Renner. Scan-

ning tunneling spectroscopy of high-temperature superconductors. *Reviews of Modern Physics*, 79, 353–419, 2007.

[74] J. E. Hoffman. Spectroscopic scanning tunneling microscopy insights into Fe-based superconductors. *Reports on Progress in Physics*, 74, 124513, 2011.

[75] R. Wiesendanger. Spin mapping at the nanoscale and atomic scale. *Reviews of Modern Physics*, 81, 1495–1550, 2009.

[76] I. Zeljkovic, Y. Okada, M. Serbyn, R. Sankar, D. Walkup, W. Zhou, J. Liu, G. Chang, Y. J. Wang, M. Z. Hasan, F. Chou, H. Lin, A. Bansil, L. Fu, and V. Madhavan. Dirac mass generation from crystal symmetry breaking on the surfaces of topological crystalline insulators. *Nature Materials*, 14, 318–24, 2015.

[77] I. Giaever. Energy gap in superconductors measured by electron tunneling. *Physical Review Letters*, 5, 147–148, 1960.

[78] I. Giaever, H. R. Hart, and K. Megerle. Tunneling into superconductors at temperatures below 1 K. *Physical Review*, 126, 941–948, 1962.

[79] W. L. McMillan and J. M. Rowell. Lead phonon spectrum calculated from superconducting density of states. *Physical Review Letters*, 14, 108–112, 1965.

[80] J. E. Hoffman, K. McElroy, D.-H. Lee, K. M. Lang, H. Eisaki, S. Uchida, and J. C. Davis. Imaging quasiparticle interference in $Bi_2Sr_2CaCu_2O_{8+delta}$. *Science*, 297, 1148–51, 2002.

[81] M. P. Allan, A. W. Rost, A. P. Mackenzie, Y. Xie, J. C. Davis, K. Kihou, C. H. Lee, A. Iyo, H. Eisaki, and T.-M. Chuang. Anisotropic energy gaps of iron-based superconductivity from intraband quasiparticle interference in LiFeAs. *Science*, 336, 563–567, 2012.

[82] M. P. Allan, F. Massee, D. K. Morr, J. van Dyke, A. W. Rost, A. P. Mackenzie, C. Petrovic, and J. C. Davis. Imaging Cooper pairing of heavy fermions in $CeCoIn_5$. *Nature Physics*, 9, 468–473, 2013.

[83] L. Petersen, Ph. Hofmann, E.W. Plummer, and F. Besenbacher. Fourier TransformSTM: determining the surface Fermi contour. *Journal of Electron Spectroscopy and Related Phenomena*, 109, 97–115, 2000.

[84] S. H. Pan, E. W. Hudson, and J. C. Davis. ^3He refrigerator based very low temperature scanning tunneling microscope. *Review Of Scientific Instruments*, 70, 1459–1463, 1999.

[85] J. Tersoff and D. R. Hamann. Theory of the scanning tunneling microscope. *Physical Review B*, 31, 805–813, 1985.

[86] M. F. Crommie, C. P. Lutz, and D. M. Eigler. Confinement of electrons to quantum corrals on a metal surface. *Science*, 262, 218–220, 1993.

[87] M. F. Crommie, C. P. Lutz, and D. M. Eigler. Imaging standing waves in a two-dimensional electron gas. *Nature*, 363, 524–527, 1993.

[88] C.-L. Song, Y.-L. Wang, Y.-P. Jiang, L. Wang, K. He, X. Chen, J. E. Hoffman, X.-C. Ma, and Q.-K. Xue. Suppression of superconductivity by twin boundaries in FeSe. *Physical Review Letters*, 109, 137004, 2012.

[89] P. Choubey, T. Berlijn, A. Kreisel, C. Cao, and P. J. Hirschfeld. Visualization of atomic-scale phenomena in superconductors: Application to FeSe. *Physical Review B*, 90, 134520, 2014.

[90] Q.-H. Wang and D.-H. Lee. Quasiparticle scattering interference in high-temperature superconductors. *Physical Review B*, 67, 020511(R), 2003.

[91] Y.-Y. Zhang, C. Fang, X. Zhou, K. Seo, W.-F. Tsai, B. A. Bernevig, and J. Hu. Quasiparticle scattering interference in superconducting iron pnictides. *Physical Review B*, 80, 094528, 2009.

[92] A. Akbari, J. Knolle, I. Eremin, and R. Moessner. Quasiparticle interference in iron-based superconductors. *Physical Review B*, 82, 224506, 2010.

[93] J. A. Slezak, J. Lee, M. Wang, K. McElroy, K. Fujita, B. M. Andersen, P. J. Hirschfeld, H. Eisaki, S. Uchida, and J. C. Davis. Imaging the impact on cuprate superconductivity of varying the interatomic distances within individual crystal unit cells. *Proceedings of the National Academy of Sciences*, 105, 3203–3208, 2008.

[94] M. J. Lawler, K. Fujita, J. Lee, A. R. Schmidt, Y. Kohsaka, C. K. Kim, H. Eisaki, S. Uchida, J. C. Davis, J. P. Sethna, and E.-A. Kim. Intra-unit-cell electronic nematicity of the high-T_c copper-oxide pseudogap states. *Nature*, 466, 347–51, 2010.

[95] A. Mesaros, K. Fukita, H. Eisaki, S. Uchida, J. C. Davis, S. Sachdev, J. Zaanen, M. J. Lawler, and E.-A. Kim. Topological defects coupling smectic modulations to intra-unit cell nematicity in cuprates. *Science*, 333, 426–430, 2011.

[96] D. Huang, C.-L. Song, T. A. Webb, S. Fang, C.-Z. Chang, J. S. Moodera, E. Kaxiras, and J. E. Hoffman. Revealing the empty-state electronic structure of single-unit-cell $FeSe/SrTiO_3$. *Physical Review Letters*, 115, 017002, 2015.

[97] T. Hanaguri, S. Niitaka, K. Kuroki, and H. Takagi. Unconventional s -Wave Superconductivity in Fe(Se,Te). *Science*, 328, 474–477, 2010.

[98] I. I. Mazin and D. J. Singh. Comment on "Unconventional s-wave superconductivity in Fe(Se, Te)", 2010.

[99] T Hanaguri, S. Niitaka, K. Kuroki, and H. Takagi. Reply to comment on "Unconventional s-wave superconductivity in Fe(Se, Te)", 2010.

[100] P. J. Hirschfeld, D. Altenfeld, I. Eremin, and I. I. Mazin. Robust determination of the superconducting gap sign structure via quasiparticle interference. *Physical Review B*, 92, 184513, 2015.

[101] T. Terashima, N. Kikugawa, A. Kiswandhi, E.-S. Choi, J. S. Brooks, S. Kasahara, T. Watashige, H. Ikeda, T. Shibauchi, Y. Matsuda, T. Wolf, A. E. Böhmer, F. Hardy, C. Meingast, H. v. Löhneysen, M.-T. Suzuki, R. Arita, and S. Uji. Anomalous Fermi surface in FeSe seen by Shubnikov-de Haas oscillation measurements. *Physical Review B*, 90, 144517, 2014.

[102] A. Kreisel, S. Mukherjee, P. J. Hirschfeld, and B. M. Andersen. Spin excitations in a model of FeSe with orbital ordering. *Physical Review B*, 92, 224515, 2015.

[103] T. Shimojima, Y. Suzuki, T. Sonobe, A. Nakamura, M. Sakano, J. Omachi, K. Yoshioka, M. Kuwata-Gonokami, K. Ono, H. Kumigashira, A. E. Böhmer, F. Hardy, T. Wolf, C. Meingast, H. v. Löhneysen, H. Ikeda, and K. Ishizaka. Lifting of xz / yz orbital degeneracy at the structural transition in detwinned FeSe. *Physical Review B*, 90, 121111(R), 2014.

[104] A. Kreisel, Y. Wang, T. A. Maier, P. J. Hirschfeld, and D. J. Scalapino. Spin fluctuations and superconductivity in $K_xFe_{2-y}Se_2$. *Physical Review B*, 88, 094505, 2013.

[105] R. M. Fernandes and O. Vafek. Distinguishing spin-orbit coupling and nematic order in the electronic spectrum of iron-based superconductors. *Physical Review B*, 90, 214514, 2014.

[106] A. Fedorov, A. Yaresko, T. K. Kim, E. Kushnirenko, E. Haubold, T. Wolf, M. Hoesch, A. Grueneis, B. Buechner, and S. V. Borisenko. Effect of nematic ordering on electronic structure of FeSe. *Scientific Reports*, 6, 36834, 2016.

[107] A. Kostin, Sprau. P. O., A. Kreisel, Y. X. Chong, A. E. Böhmer, P. C. Canfield, P. J. Hirschfeld, B. M. Andersen, and J. C. Davis. Visualization of an orbital selective Mott phase in FeSe, in preparation 2017.

[108] E. Bascones, B. Valenzuela, and M. J. Calderón. Magnetic interactions in iron superconductors: A review. *Comptes Rendus Physique*, 17, 36–59, 2016.

[109] A. E. Böhmer, T. Arai, F. Hardy, T. Hattori, T. Iye, T. Wolf, H. v. Löhneysen, K. Ishida, and C. Meingast. Origin of the tetragonal-to-orthorhombic phase transition in FeSe: A combined thermodynamic and NMR study of nematicity. *Physical Review Letters*, 114, 027001, 2015.

[110] A. E. Böhmer and C. Meingast. Electronic nematic susceptibility of iron-based superconductors. *Comptes Rendus Physique*, 17, 90–112, 2016.

[111] S-H. Baek, D. V. Efremov, J. M. Ok, J. S. Kim, J. van den Brink, and B. Büchner. Orbital-driven nematicity in FeSe. *Nature Materials*, 14, 210–214, 2014.

[112] P. Zhang, T. Qian, P. Richard, X. P. Wang, H. Miao, B. Q. Lv, B. B. Fu, T. Wolf, C. Meingast, X. X. Wu, Z. Q. Wang, J. P. Hu, and H. Ding. Observation of two distinct d_{xz} / d_{yz} band splittings in FeSe. *Physical Review B*, 91, 214503, 2015.

[113] A. E. Böhmer, V. Taufour, W. E. Straszheim, T. Wolf, and P. C. Canfield. Variation of transition temperatures and residual resistivity ratio in vapor-grown FeSe. *Physical Review B*, 94, 024526, 2016.

[114] U. S. Kaluarachchi, V. Taufour, A. E. Böhmer, M. A. Tanatar, S. L. Bud'ko, V. G. Kogan, R. Prozorov, and P. C. Canfield. Nonmonotonic pressure evolution of the upper critical field in superconducting FeSe. *Physical Review B*, 93, 064503, 2016.

[115] K. McElroy, R. W. Simmonds, J. E. Hoffman, D.-H. Lee, J. Orenstein, H. Eisaki, S. Uchida, and J. C. Davis. Relating atomic-scale electronic phenomena to wave-like quasiparticle states in superconducting $Bo_2Sr_2CaCu_2O_{8+\delta}$. *Science*, 422, 592–596, 2003.

[116] Z. Wang, H. Yang, D. Fang, B. Shen, Q.-H. Wang, L. Shan, C. Zhang, P. Dai, and H.-H. Wen. Close relationship between superconductivity and the bosonic mode in $Ba_{0.6}K_{0.4}Fe_2As_2$ and $Na(Fe_{0.975}Co_{0.025})As$. *Nature Physics*, 9, 42–48, 2012.

[117] C.-L. Song, Y.-L. Wang, Y.-P. Jiang, Z. Li, L. Wang, K. He, X. Chen, J. E. Hoffman, X.-C. Ma, and Q.-K. Xue. Imaging the electron-boson coupling in superconducting FeSe films using a Scanning Tunneling Microscope. *Physical Review Letters*, 112, 057002, 2014.

[118] T. Hanaguri, Y. Kohsaka, M. Ono, M. Maltseva, P. Coleman, I. Yamada, M. Azuma, M. Takano, K. Ohishi, and H. Takagi. Coherence factors in a high- Tc cuprate probed by quasi-particle scattering off vortices. *Science*, 323, 923–927, 2009.

[119] A. T. Rømer, A. Kreisel, I. Eremin, M. A. Malakhov, T. A. Maier, P. J. Hirschfeld, and B. M. Andersen. Pairing symmetry of the one-band Hubbard model in the paramagnetic weak-coupling limit: A numerical RPA study. *Physical Review B*, 92, 104505, 2015.

[120] S. Chi, R. Aluru, U. R. Singh, R. Liang, W. N. Hardy, D. A. Bonn, A. Kreisel, B. M. Andersen, R. Nelson, T. Berlijn, W. Ku, P. J. Hirschfeld, and P. Wahl. Impact of iron-site defects on superconductivity in LiFeAs. *Physical Review B*, 94, 134515, 2016.

[121] D. Huang, T. A. Webb, C.-L. Song, C.-Z. Chang, J. S. Moodera, E. Kaxiras, and J. E. Hoffman. Dumbbell defects in FeSe films: A Scanning Tunneling Microscopy and first-principles investigation. *Nano Letters*, 16, 4224–4229, 2016.

[122] J. H. J. Martiny, A. Kreisel, P. J. Hirschfeld, and B. M. Andersen. Robustness of quasiparticle interference test for sign-changing gaps in multiband superconductors. *Arxiv Preprint*, 1703.04891v1, 2017.

[123] Q. Wang, Y. Shen, B. Pan, Y. Hao, M. Ma, F. Zhou, P. Steffens, K. Schmalzl, T. R. Forrest, M. Abdel-Hafiez, X. Chen, D. A. Chareev, A. N. Vasiliev, P. Bourges, Y. Sidis, H. Cao, and J. Zhao. Strong interplay between stripe

spin fluctuations, nematicity and superconductivity in FeSe. *Nature Materials*, 15, 159–164, 2016.

[124] S. Graser, T. A. Maier, P. J. Hirschfeld, and D. J. Scalapino. Near-degeneracy of several pairing channels in multiorbital models for the Fe pnictides. *New Journal of Physics*, 11, 025016, 2009.

[125] R. Yu and Q. Si. U(1) slave-spin theory and its application to Mott transition in a multiorbital model for iron pnictides. *Physical Review B*, 86, 085104, 2012.

[126] A. Kreisel, B. M. Andersen, P. O. Sprau, A. Kostin, J. C. Davis, and P. J. Hirschfeld. Orbital selective pairing and gap structures of iron-based superconductors. *Physical Review B*, 00, accepted for publication, 2017.

[127] E. P. Rosenthal, E. F. Andrade, C. J. Arguello, R. M. Fernandes, L. Y. Xing, X. C. Wang, C. Q. Jin, A. J. Millis, and A. N. Pasupathy. Visualization of electron nematicity and unidirectional antiferroic fluctuations at high temperatures in NaFeAs. *Nature Physics*, 10, 225–232, 2014.

[128] T. Dahm and D. J. Scalapino. Quasi-particle interference probe of the self-energy. *New Journal of Physics*, 16, 023003, 2014.

[129] R. Comin and A. Damascelli. *Strongly Correlated Systems*, volume 180, 31–71 of *Springer Series in Solid-State Sciences*. Springer, 2014.

[130] M. Neupane, P. Richard, Z.-H. Pan, Y.-M. Xu, R. Jin, D. Mandrus, X. Dai, Z. Fang, Z. Wang, and H. Ding. Observation of a novel orbital selective Mott transition in $Ca_{1.8}Sr_{0.2}RuO_4$. *Physical Review Letters*, 103, 097001, 2009.